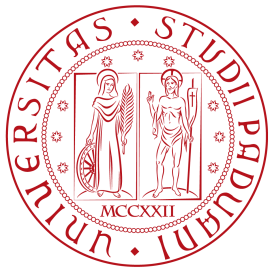

UNIVERSITÀ DEGLI STUDI DI PADOVA

Dipartimento di Fisica e Astronomia "Galileo Galilei"

Master Degree in Astrophysics and Cosmology

Final Dissertation

Characterization of sodium targets for the study of ^{23}Na$(p,\alpha)^{20}$Ne reaction at LUNA

Thesis supervisor

Prof. Antonio Caciolli

Thesis co-supervisor

Dr.ssa Denise Piatti

Candidate

Riccardo Biasissi

Academic Year 2023/2024

Abstract

Stars produce most of elements in the universe out of primordial nuclei, H and He. Nuclear fusion reactions taking place deep inside stellar cores both provide the energy to keep stars in hydrostatic equilibrium and are responsible for the stellar nucleosynthesis. When the protostar temperature is high enough to start H ignition, it enters the Zero Age Main Sequence and accretes a He core via either predominantly the p – p chain ($M_i \lesssim 1.2\,M_\odot$) or the CNO cycle ($M_i \gtrsim 1.2\,M_\odot$). When star runs out of H, the leftover moves to outer layers while the core shrinks. The H continues burning progressively on a thin shell around the He core while the core contracts. When the temperature rises enough to burn He via the 3α process, the star will develop a C/O core.

When the He-burning phase ends, stars with initial mass between 0.6 and $8\,M_\odot$ will enter the Asymptotic Giant Branch (AGB) phase. AGB-stars with a progenitor of at least $4\,M_\odot$ are sustained by an alternating He and H shell burning. In particular, the He shell burning proceeds via thermal pulses which drive deep convective phenomena in the (convective) envelope of the star. These mixing events bring on the surface products typical of CNO, NeNa and MgAl cycles, like O and Na. As they reach the star surface, they are effectively dispersed in the interstellar medium via the strong stellar winds typical of AGB-stars.

Globular clusters (GC) are objects formed by hundreds of thousands of stars bound by gravity. Several observations of GC, some of which dates back to the seventies, revealed a number of anomalies in the observed chemical abundances, i.e. the Na-O anti-correlation. The activation in AGB stars of the NeNa cycle together with mixing events and mass loss makes them the best candidate to pollute the surrounding interstellar medium from which second generation of stars are formed within the globular cluster. The $^{23}\mathrm{Na}(p,\alpha)^{20}\mathrm{Ne}$ reaction is placed at the branching point between the NeNa and MgAl cycles and it is responsible for the conversion of ^{23}Na into ^{20}Ne. Since this reaction directly affect the ^{23}Na abundance that will be eventually brought to the surface during the mixing processes and subsequently dispersed in the interstellar medium, it is crucial to precisely determine its reaction rate to constrain the role of AGB in the Na-O anti-correlation.

Variations of the cross-section of the $^{23}\mathrm{Na}(p,\alpha)^{20}\mathrm{Ne}$ reaction can dramatically influence the predicted Na abundance. Resonances play a fundamental role by enhancing the cross-section around the resonance energy E_r. The last uncertainties that affect the $^{23}\mathrm{Na}(p,\alpha)^{20}\mathrm{Ne}$ reaction rate are related to low-energy resonances below 170 keV. In particular, the resonance at $E_\mathrm{r}^\mathrm{cm} = 138$ keV has not been observed directly and is still affected by large uncertainties. An upcoming experiment at LUNA 400kV accelerator aims for the first time at directly measuring its strength. A high intensity proton beam will be delivered from LUNA 400kV to a solid target, while the generated α particles will be detected at backward angles by a dedicated array of Si detectors. Backscattered protons will be filtered out by thin foils of aluminised Mylar.

The present work focuses on the characterization of the solid targets which will be used in the aforementioned measurement. Two types of targets have been investigated: the evaporated Na_2WO_4 targets produced initially by the Laboratori Nazionali di Legnaro LNL (Italy) and later by the Institute for Nuclear Research (MTA Atomki) in Debrecen (Hungary), and the sputtered $NaNbO_3$ targets produced at LNL. The relevance of this analysis lies in the fact that targets represent one of the main source of systematic uncertainty. In order to characterize targets, the well known Nuclear Resonant Reaction Analysis technique, consisting of scanning a narrow resonance has been used.

Contents

1 Astrophysical introduction

The primordial abundances of hydrogen and helium that were produced during the Big Bang nucleosynthesis, have been subsequently processed in stars to form most of the nuclei we observe nowadays. Stars are expected to form in cold (10 – 100 K) and relatively dense (10 – 300 molecules/cm^3) molecular clouds [1, 2, 3]. An external event, such as a shock wave, may triggers the cloud collapse which will lead to the formation of many protostars. If the core of such object reaches temperatures of at least 8 MK there is the onset of hydrogen burning processes and the freshly formed star enters the Zero Age Main Sequence (ZAMS). During this phase the hydrogen will burn either via p – p chain or CNO cycle depending on the star mass. Stars with an initial mass $M_i \gtrsim 1.2 - 1.3\,M_\odot$ will rather burn hydrogen via the CNO cycle. The main consequence of this burning phase is the production of He which is the fuel of the next core-burning stage. As the He core is developed, the hydrogen burning continues in a thinner shell around the contracting core.

When the core temperature reaches $T \gtrsim 0.1$ GK, there is the onset of helium burning via the 3α process [4] which is responsible of the buildup of carbon. As its abundance increases in the core, the $^{12}C(\alpha,\gamma)^{16}O$ reaction gradually starts depleting carbon. The complex interplay between 3α and $^{12}C(\alpha,\gamma)^{16}O$ reactions leads ultimately to the formation of a C/O core with two shells of H and He enveloping it.

When the He-burning phase ends, stars with a progenitor of mass between 0.6 and 8 $M_\odot$ will enter the Asymptotic Giant Branch (AGB) phase. For the scopes of the present study I will focus on this particular phase of stellar evolution.

1.1 The Asymptotic Giant Branch phase

The AGB phase, shown with a red shaded area in the HR diagram in Fig. 1.1 strongly depends on the initial mass. We recover the low-mass AGB ($M_i \lesssim 4\,M_\odot$), the massive AGB ($4\,M_\odot \lesssim M_i \lesssim 8\,M_\odot$) and the super AGB ($M_i \gtrsim 8\,M_\odot$) stars, which is the only class achieving (unstable) carbon burning in their core developing an ONeMg nucleus. Schematically, these three classes follow an initial stage of Early AGB (E-AGB) and later develop into a Thermally Pulsing AGB (TP-AGB). During the E-AGB phase, the stellar core contracts while the He-burning shell expands, extinguishing the H-shell. Throughout the E-AGB phase, the star is sustained by the He-shell burning. As the helium abundance in this shell lowers it eventually extinguishes too.

After the He-shell extinguishes at the end of the E-AGB phase, the H-shell contracts in response and eventually re-ignites. The TP-AGB phase consists of several cyclic events during which the hydrogen and helium shells burnings alternate. The ignited H-shell accretes with helium the top layer of the underlying shell and once the bottom of the He-shell achieves temperatures up to 0.3 GK, He starts igniting explosively giving place to the He-shell flash. This large energy flux induces the generation of a pulse-driven convective inter-shell that will extend between the bottom of He-shell and the H-shell. The convective

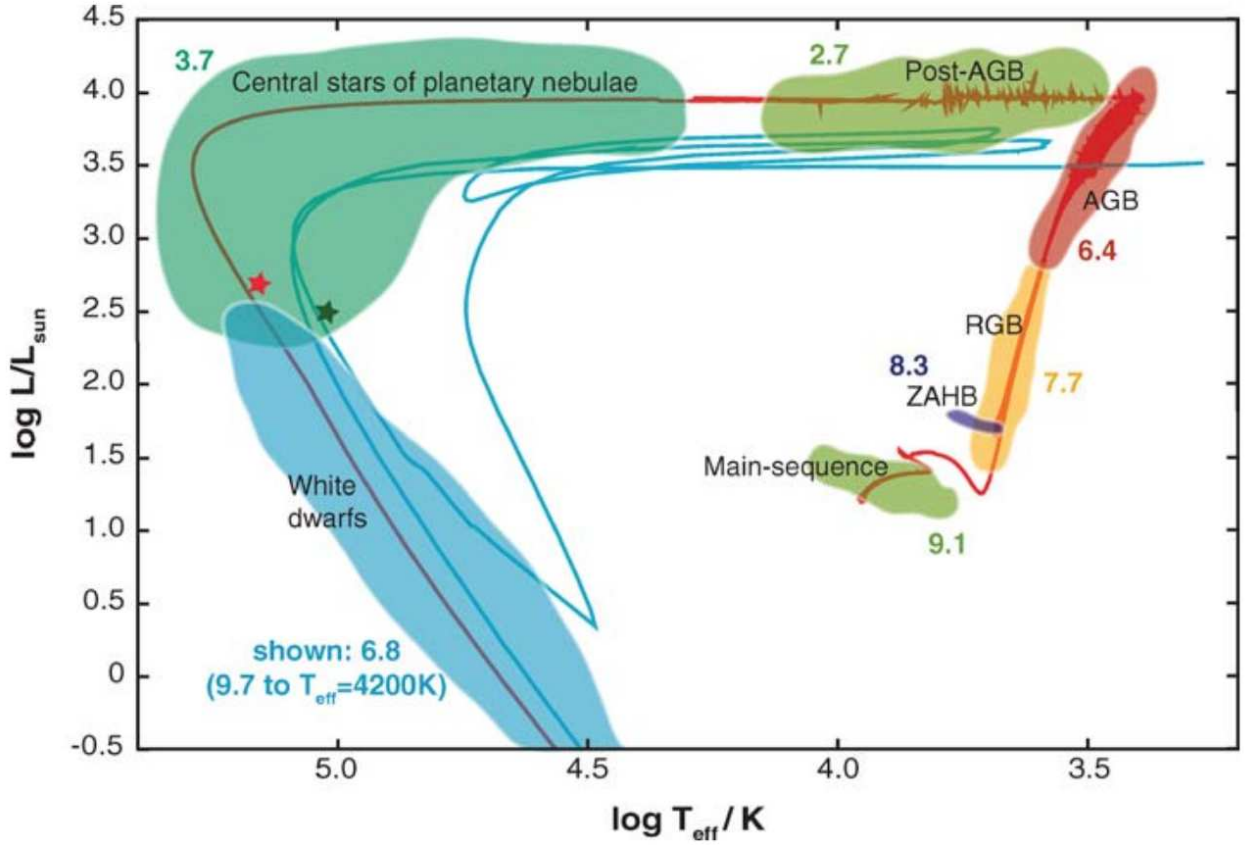

Figure 1.1: Complete HR diagram of a $2\,M_\odot$ star of solar metallicity, the reported numbers next to each phase represents the logarithm of their duration. The AGB phase stands in the top-right corner (red region) [5].

processes in the inter-shell allows to inject fresh He produced by the above H-shell and remove the products of 3α reactions during the He-shell flash.

However, most of the energy released by the He-shell flash causes an expansion of the inter-shell which extinguishes the H-shell, follows a short but stable He-burning phase. This expansion allows a deeper penetration of the convective envelope that reaches the inter-shell region and bring to the star surface elements typical of the 3α process like ^{12}C, this phenomenon is called third dredge-up. Following the third dredge-up, the H-shell reignites and stably burn hydrogen for a period from less than 1 Myr to 1 Gyr (interpulse) depending on the star mass while the He-shell becomes inactive again.

In massive and super AGB stars the shell H-burning takes place at temperatures between 40-100 MK. At such high temperature the H burning proceeds via CNO cycle and NeNa and MgAl cycles are also activated, this is the so called Hot Bottom Burning (HBB). The products of these cycles during successive mixing processes are brought to the stellar surface and ejected in the ISM. The combination between mixing processes and mass loss make AGB stars the best candidates of the pollution model to explain Globular Cluster Na-O anti-correlation. In Fig. 1.2 is reported the evolution of a $15\,M_\odot$ star between two consecutive thermal pulses. Among the reactions of the NeNa cycle the most uncertain is the $^{23}Na(p,\alpha)^{20}Ne$, which is the focus of Section 3. Before examining the case of

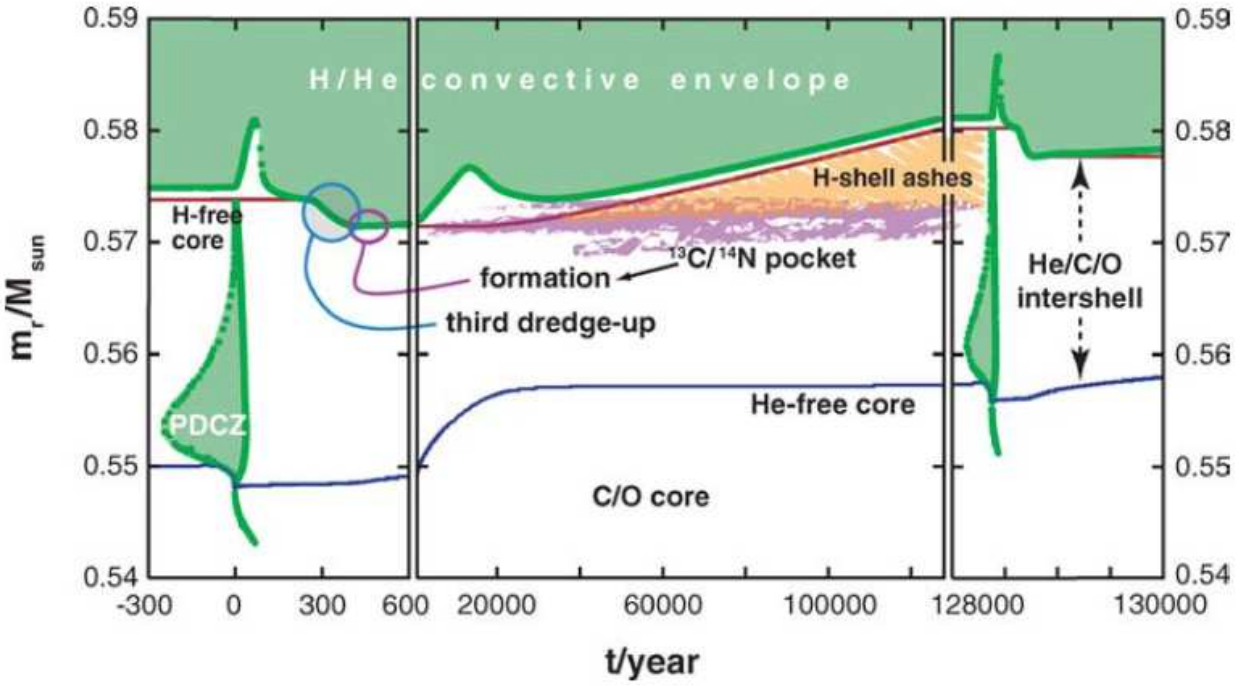

Figure 1.2: Thermal pulses and interpulse between them for a $15\,M_\odot$ star of $Z = 0.01$. In green are indicate the convection zones (PDCZ is the Pulse-Driven Convection Zone induced by 3α process). Courtesy of [5].

^{23}Na$(p,\alpha)^{20}$Ne, in Section 2 useful formalism for the nuclear reaction is described.

2 Theoretical framework

Nuclear reactions are of fundamental importance in describing and predicting the stellar evolution and nucleosynthesis. Since the present work aims at characterizing the targets that will be used in the measurement of a cross-section, this section reports some basics of nuclear astrophysics. These tests, as I will explain in Section 4, involved the Nuclear Resonance Reaction Analysis (NRRA) technique which is based on the concept of nuclear resonance. The topic of resonant processes here presented aims to show the relations between quantities like reaction rate, cross-section and resonance strength.

2.1 Q-value, cross-section and reaction rate

For a reaction involving two bodies like T(P, D)R the interacting nuclei, T and P, constitute the entrance channel while the produced nuclei, D and R, are instead the exit channel. Each particle involved will be characterized by an energy which will be the sum of two contributes. A first term is given by the kinetic energy, K_i, while the second is represented by the rest energy, $m_i c^2$. Applying the energy conservation:

$$0 = (m_T + m_P - m_D - m_R)c^2 + K_T + K_P - K_D - K_R \tag{2.1}$$

separating the kinetic and rest energy terms it is possible to introduce a quantity called Q-value:

$$Q = (m_T + m_P - m_D - m_R)c^2 = -K_T - K_P + K_D + K_R \tag{2.2}$$

it represents the energy released ($Q > 0$, exothermic) or consumed ($Q < 0$, endothermic) by the reaction. The cross-section σ, namely the probability for a reaction to take place, is defined as:

$$\sigma = \frac{N_R \cdot A}{N_P \cdot N_T} \tag{2.3}$$

where N_R is the number of reactions, N_P is the number of beam particles, N_T is the number of target nuclei and A is the surface area impinged by the beam. Along with the cross-section, in nuclear astrophysics another important quantity is the reaction rate. It is defined as the number of reactions per unit of time and volume:

$$r = \frac{N_R}{V \cdot t} = \sigma \frac{N_T}{V} \frac{N_P}{A \cdot t} = \sigma \frac{N_T}{V} \frac{N_P}{V} v = \sigma v \; n_T n_P \tag{2.4}$$

where we used Eq. (2.3) and expressed the volume as $V = A \cdot L = A\ (v \cdot t)$, with v the particles relative velocity, therefore $A = V/(v \cdot t)$. Moreover n_T and n_P are the number density of target and beam particles.

In stellar environment the relative velocity v is not constant, but rather follows a dis-

tribution $\phi(v)$. For this reason, more realistically, the reaction rate r is expressed as:

$$r = \frac{n_T n_P}{1+\delta_{TP}} \int_0^\infty dv\ v\ \phi(v)\ \sigma(v) = \frac{n_T n_P}{1+\delta_{TP}} \langle \sigma v \rangle \tag{2.5}$$

where the coefficient $1 + \delta_{TP}$ corrects the result for possible reaction between identical particles. In the right-hand-side term of Eq. (2.5), the quantity $\langle \sigma v \rangle$ represents the cross-section for pair particles and it is defined as below:

$$\langle \sigma v \rangle = \int_0^\infty dv\ v\ \phi(v)\ \sigma(v) \tag{2.6}$$

Since nuclei in stellar plasma are characterized by non-relativistic and non-degenerate conditions [6], it is correct to assume they follow a Maxwell-Boltzmann distribution:

$$\phi(E)\ dE = \frac{2}{\sqrt{\pi}} \frac{1}{(k_B T)^{3/2}} \sqrt{E} \cdot \exp\left(-\frac{E}{k_B T}\right) dE \tag{2.7}$$

where T is the local plasma temperature and k_B is the Boltzmann constant. It describes, for a given temperature T, the probability that the relative particles velocity has a value between v and $v + dv$. By substituting the Maxwell-Boltzmann distribution of Eq. (2.7) in the expression for $\langle \sigma v \rangle$ of Eq. (2.6) and by using the relation $E = \mu v^2/2$ between energy E and the velocity v (μ is the reduced mass equal to $m_T m_P/(m_T + m_P)$), we immediately obtain:

$$\langle \sigma v \rangle = \left(\frac{8}{\pi\mu}\right)^{1/2} \frac{1}{(k_B T)^{3/2}} \int_0^\infty dE\ E\ \sigma(E)\ \exp\left(-\frac{E}{k_B T}\right) \tag{2.8}$$

It is clear that the term $\langle \sigma v \rangle$ will give distinct results for different gas temperatures T, for this reason some reactions will be more efficient than others as the star evolves. The cross-section that enters in Eq. (2.8) is required to calculate the reaction rate r, from which then the produced energy and the impact of the reaction on nucleosynthesis can be calculated. In the later, the cross-section description for the cases of direct capture and the narrow resonances is reported.

2.2 Direct and resonant processes

In nuclear astrophysics direct and resonant processes are distinguished. A direct process is characterized by a transition that ends on a bound state. Consider, for example, the radiative capture of A with the particle x to form B. The cross-section is proportional to a single matrix element:

$$\sigma \propto |\langle B|H|A + x\rangle|^2 \tag{2.9}$$

where H is the electromagnetic operator that describes the transition. This kind of process can occur at any projectile energies, therefore the cross-section has a smooth energy dependence. In resonant processes instead a compound nucleus, that subsequently decays,

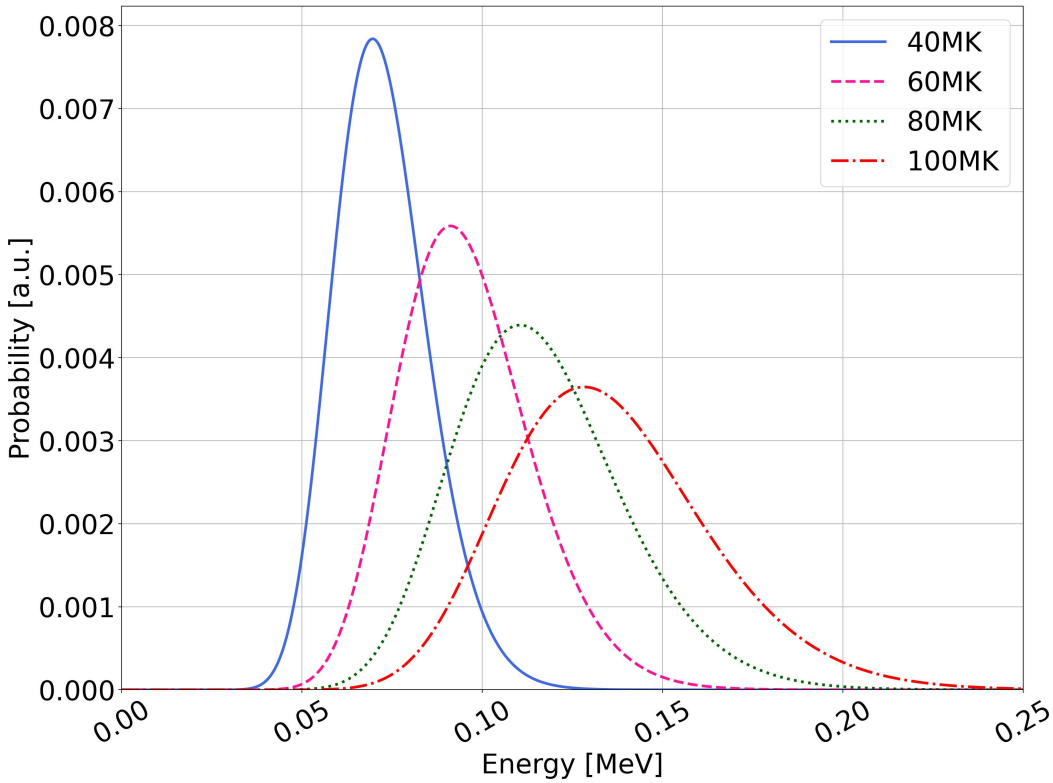

Figure 2.1: Representation of the Gamow peak for the $^{23}\mathrm{Na}(p,\alpha)^{20}\mathrm{Ne}$ reaction at four different temperatures relevant in the HBB events of AGB stars (40, 60, 80 and 100 MK). The curves are normalized by their area.

is formed. In this case the initial particle energy must fall close to the resonance E_r. Using the previous example:

$$\sigma \propto |\langle E_\mathrm{r}|H_B|A+x\rangle|^2 \cdot |\langle B|H|E_\mathrm{r}\rangle|^2 \tag{2.10}$$

where the first matrix element represents the compound formation while the second the decay process, H and H_B are the usual electromagnetic operators associated to each step of the resonant process.

2.2.1 Direct processes

Whenever a nuclear reaction takes place, the involved nuclei must overcome the strong electrostatic repulsion between them. This threshold is called Coulomb barrier. However, particles with energies below this limit have a non-zero probability to pass through due to tunnel effect and thus give place to a reaction. The probability of a nucleus to overcome the Coulomb barrier is approximated by the penetrability term $P(E)$, defined as follows:

$$P(E) \propto \exp(-2\pi\eta) \tag{2.11}$$

where $\eta = b/\sqrt{E}$ is the Sommerfeld parameter with b a terms that accounts for the charges and masses involved in the reaction. For non-resonant processes, the cross-section is

defined as:

$$\sigma(E) = \frac{1}{E} \exp(-2\pi\eta)\, S(E) \tag{2.12}$$

where $S(E)$ is the astrophysical S-factor which has generally a weak energy dependence and accounts for all nuclear effects. By substituting Eq. (2.12) in the definition of $\langle \sigma v \rangle$ of Eq. (2.8) one obtain:

$$\langle \sigma v \rangle = \left(\frac{8}{\pi\mu} \right)^{1/2} \frac{1}{(\mathrm{k_B} T)^{3/2}} \int_0^\infty dE\; S(E) \cdot \exp\left(-\frac{b}{\sqrt{E}} - \frac{E}{\mathrm{k_B} T} \right) \tag{2.13}$$

In the assumption of constant S-factor, the integrand in Eq. (2.13) is the Gamow peak with maximum located at E_0 and width ΔE:

$$E_0 = \left(\frac{b\, \mathrm{k_B} T}{2} \right)^{2/3} \qquad \Delta E \propto \sqrt{E_0\, \mathrm{k_B} T} \tag{2.14}$$

note that these quantities will depend generally on the nuclei charges via the b term, so these values and the Gamow profile in general depends on the entrance channel particles and strongly varies with the temperature. Since the Gamow peak is generally centered at energies ranging from few eV to some MeV where the penetrability term is small, the resulting cross-section is still tiny (of the order 10^{-15}b). An exemplification relevant to this work is shown in Fig. 2.1.

2.2.2 Resonant processes

As stated before, in case of resonant processes, there is the initial formation of a compound that will decay subsequently. The reaction takes place following a chain like $\mathrm{P} + \mathrm{T} \rightarrow \mathrm{C} \rightarrow \mathrm{D} + \mathrm{R}$ where C is the compound that subsequently decays. When dealing with a resonance well separated from the others, it is possible to study its effect on the reaction rate without the interferences from others. In this simplified but often valid case, the cross-section σ is described by the Breit-Wigner formula:

$$\sigma(E) = \frac{\lambda^2}{4\pi} \cdot \frac{2J_\mathrm{C} + 1}{(2J_\mathrm{P} + 1)(2J_\mathrm{T} + 1)} \cdot (1 + \delta_\mathrm{PT}) \cdot \frac{\Gamma_\mathrm{P}\Gamma_\mathrm{R}}{(E - E_\mathrm{r})^2 + (\Gamma/2)^2} \tag{2.15}$$

where $\lambda = 2\pi\hbar/\sqrt{2\mu E}$ is the de Broglie wavelength, J_i is the spin of i-th particle, Γ_i is the partial width for decay via emission of i-th particle, $\Gamma = \Gamma_\mathrm{P} + \Gamma_\mathrm{R}$ is the total width of the compound excited state and finally E_r is the resonance energy in the center of mass reference frame. Again, the factor $1 + \delta_\mathrm{PT}$ corrects the results for reaction involving identical particles since in this case the cross-section is enhanced by a factor of 2. For simplicity, the term involving spins and correction for equal particles of Eq. (2.15) is indicated as ω.

With the Eq. (2.15), the $\langle \sigma v \rangle$ term of Eq. (2.8) to compute the reaction rate is:

$$\langle \sigma v \rangle = \sqrt{2\pi} \frac{\hbar^2}{(\mu k_B T)^{3/2}} \omega \int_0^\infty dE \; \frac{\Gamma_P \Gamma_R}{(E - E_r)^2 + (\Gamma/2)^2} \exp\left(-\frac{E}{k_B T}\right) \tag{2.16}$$

but for a narrow resonance the exponential term of Maxwell-Boltzmann distribution and the partial widths can be assumed constants over the total width of the resonance. For this reason, these terms can be evaluated at the resonance energy E_r and be extracted from the integral which admits analytical solution if we multiply and divide the integrand with $\Gamma/2$:

$$\langle \sigma v \rangle = \sqrt{2\pi} \frac{\hbar^2}{(\mu k_B T)^{3/2}} \exp\left(-\frac{E_r}{k_B T}\right) \omega \frac{\Gamma_P \Gamma_R}{\Gamma} 2 \int_0^\infty dE \; \frac{\Gamma/2}{(E - E_r)^2 + (\Gamma/2)^2} \tag{2.17}$$

the integration results is formally $\pi/2 + \arctan(2 \cdot E_r/\Gamma)$. However, since we are in the limit of narrow resonance, $E_r/\Gamma \to \infty$ so the integration result is π. Moreover the term $\Gamma_P \Gamma_R/\Gamma$ is expressed as γ for simplicity, obtaining:

$$\langle \sigma v \rangle = \left(\frac{2\pi}{\mu k_B T}\right)^{3/2} \hbar^2 \exp\left(-\frac{E_r}{k_B T}\right) \omega\gamma \tag{2.18}$$

the term $\omega\gamma$ is called resonance strength since it is proportional to the area under the resonance cross-section. Moreover, by looking at the γ term, it is immediate to note that the reaction rate is determined always by the smaller width:

$$\begin{aligned} \Gamma_P \gg \Gamma_R \Rightarrow \Gamma \approx \Gamma_P \Rightarrow \gamma \approx \Gamma_R \\ \Gamma_R \gg \Gamma_P \Rightarrow \Gamma \approx \Gamma_R \Rightarrow \gamma \approx \Gamma_P \end{aligned} \tag{2.19}$$

To calculate the total reaction rate the contribution from all the resonances must be taken into account.

3 The ^{23}Na$(p,\alpha)^{20}$Ne reaction

In the following I focus on the relevance of the ^{23}Na$(p,\alpha)^{20}$Ne reaction in the context of the Globular Cluster (GC) Na-O anti-correlation puzzle. I will consider here, indeed, the scenario proposed in [7], which attribute the anomaly in the GC observed abundances to the ISM pollution by AGB stars. Finally I present the specific case of the $E_r^{cm} = 138\,\text{keV}$ resonance in the ^{23}Na$(p,\alpha)^{20}$Ne reaction.

3.1 Astrophysical motivation

A yet unresolved astrophysical problem, is the oxygen-sodium anti-correlation observed in globular clusters (GC) [7, 8]. GC are objects that contain millions of low-metal and very old stars gravitationally bound together. Their origins generally dates back to the very first stages of the universe, therefore understanding the origin of their observed abundances can improve our knowledge in the chemical evolution of galaxies and universe. The results of spectroscopic analysis based on 17 GCs are reported in Fig. 3.1 [7] and shows nicely the strong anti-correlation between the observed abundances of sodium and oxygen. Other examples are NGC2808 [9], NGC5904 [10], NGC6388 [11] and NGC 6441 [12]. Various models have been proposed but in the recent years it is believed that the observed anti-correlation is the fingerprint of nucleosynthesis taking place in AGB stars. As explained in Section 1, in between the thermal pulses, massive and super AGB stars experience the HBB. In this phase, the bottom of the convective envelope reaches temperatures up to 100 MK and the H-burning takes place via CNO, NeNa and MgAl cycles. A representation of the NeNa as well as the two adjacent cycles is reported in 3.2 [13]. The initial abundance of ^{20}Ne required in the NeNa cycles is either given by the ^{19}F$(p,\gamma)^{20}$Ne reaction of elements that are involved in the CNO cycle or comes from previous generation stars. In the NeNa cycle, the ^{23}Na represents a branching point since it can proceed either via ^{23}Na$(p,\alpha)^{20}$Ne or ^{23}Na$(p,\gamma)^{24}$Mg reactions. Clearly their relevance lies in the fact that the first closes the NeNa cycle, while the latter produces the starting nucleus of the MgAl cycle. The nucleosynthesis taking place in the H-shell affects the surface abundances and ultimately the chemical composition of the material ejected in the ISM, via the mixing processes in the convective envelope.

3.2 State of the art

The ^{23}Na$(p,\alpha)^{20}$Ne reaction rate (Q-value equal to $(2376.1338 \pm 0.0015)\,\text{keV}$ [14]) at the temperature of interest for the HBB in AGB stars is mainly determined by three resonances at $E_r^{cm} = 138\,\text{keV}$, 167 keV and 170 keV. Some basic properties of these resonances are reported in Tab. 3.1. The resonance sets at $E_r^{cm} = 167\,\text{keV}$ can be disregarded since it is characterized by a high angular momentum transfer ($J^\pi = 8^+$ from linear polarization measurements [15]) that strongly suppresses it due to the large centrifugal barrier. The

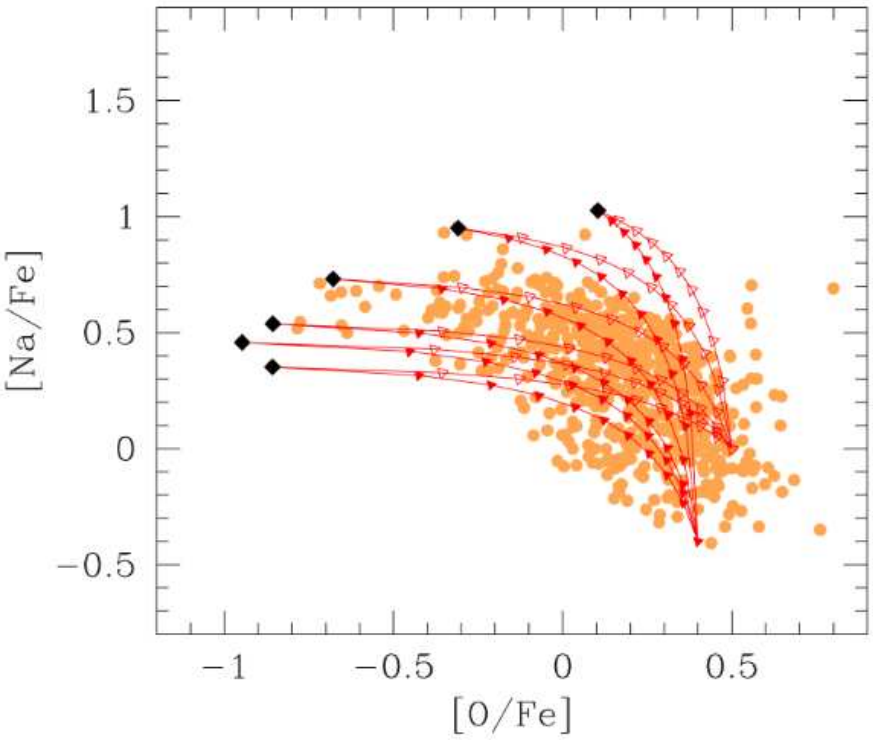

Figure 3.1: Oxygen and sodium abundances of 17 globular clusters, normalized with respect to iron. Orange dots represent spectroscopic data, while the red lines are evolutionary paths of TP-AGB models with initial mass comprised between $4-5\,M_{\odot}$ in steps of $0.2\,M_{\odot}$ [7].

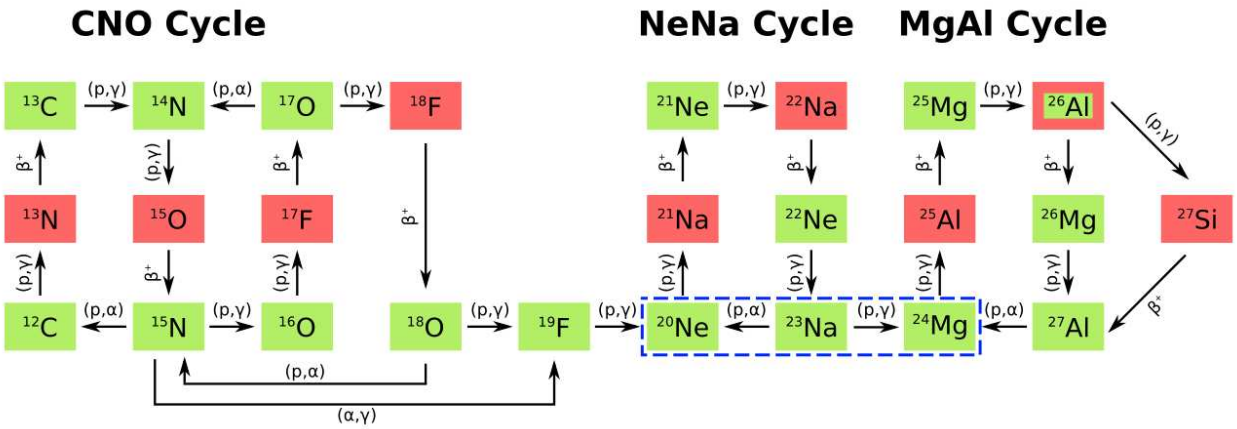

Figure 3.2: Reaction network of the CNO, NeNa and MgAl cycles, stable nuclides are reported in green [13]. I marked the reactions of interest in the this work with a blue dashed rectangle.

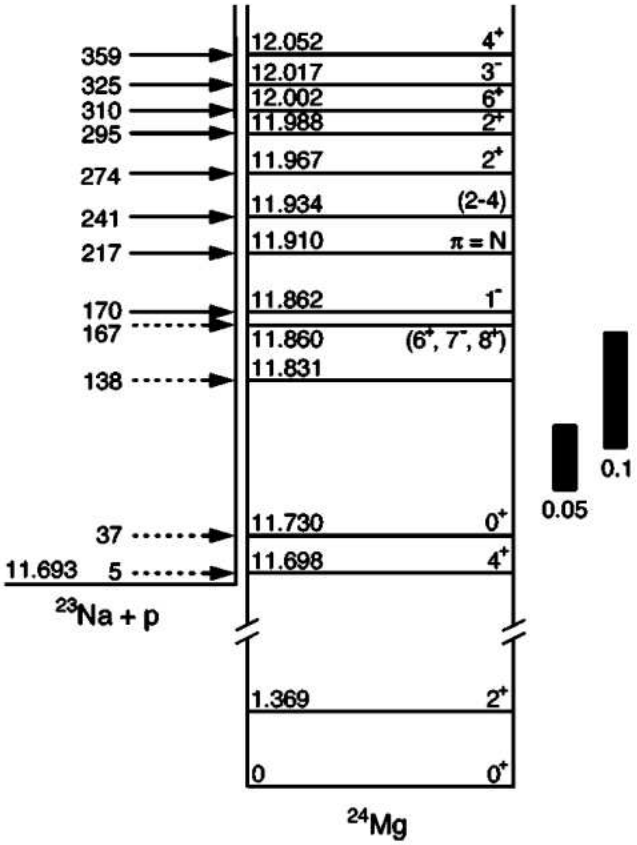

Figure 3.3: Level scheme of ^{24}Mg, on the right-hand-side it is represented the Gamow window for two temperatures of astrophysical relevance for AGB stars in GK. Dashed lines represents resonances that have not been observed directly. The reported resonance values are expressed in keV and referred to the center of mass, excited states are in MeV instead. Adapted from [16].

highest energy resonance from those considered here is at $E_r^{cm} = 170\,\text{keV}$ and it is the only one that has been studied directly. Its resonance strengths is known with an uncertainty of about 20% and its contribution to the final reaction rate is modest. Therefore, only the $E_r^{cm} = 138\,\text{keV}$ resonance is expected to dominate the final reaction rate at the considered temperatures. Since the ^{24}Mg is associated to an α-threshold of $Q_\alpha = -9316.56\,\text{keV}$, the $E_r^{cm} = 138\,\text{keV}$ resonance corresponds to the 11 830.69 keV state of ^{24}Mg. In Fig. 3.3 it is reported a scheme of the ^{24}Mg levels with two ranges of the Gamow window, defined in Section 2, relevant to the HBB. Since the $E_r^{cm} = 138\,\text{keV}$ resonance has never been studied directly, its state is not unequivocally identified. Selection rules allow to infer some hypothesis on this resonance J^π, but the resulting resonance strength $\omega\gamma$ varies of many orders of magnitudes.

Many experimental efforts have been dedicated to the measurement of the 138 keV resonance strength $\omega\gamma$. The first relevant study [17] dates back to 1989 and aimed at studying two resonances at $E_r^{cm} = 138\,\text{keV}$ and $E_r^{cm} = 217\,\text{keV}$. The 360 keV accelerator at the University of Munster was used to accelerate a proton beam in the energy range of $150 - 350\,\text{keV}$ on evaporated targets. Two types of detectors were used in coincid-

Table 3.1: Resonance strengths and J^π associated to the three resonances relevant in the ^{23}Na$(p,\alpha)^{20}$Ne reaction. The wide $\omega\gamma$ range reported for the $E_r^{cm} = 138\,\text{keV}$ depends on the choice of the angular momentum transfer ℓ, its J^π is unknown. For the $E_r^{cm} = 167\,\text{keV}$ the resonance strength is negligible due to the high J^π. Reported values are retrieved from [16, 15].

E_r^{cm} [keV]	J^π	$\omega\gamma$ [eV]
138	? ($\ell = 0$)	$\leq 1.6 \times 10^{-6}$
	? ($\ell = 1$)	$\leq 7.5 \times 10^{-8}$
	? ($\ell = 2$)	$\leq 2.8 \times 10^{-9}$
	? ($\ell = 3$)	$\leq 5.4 \times 10^{-11}$
167	8^+	negligible
170	1^-	2.3×10^{-5}

ence, a Ge(Li) detector at 0° to investigate the (p,γ) reaction and a Si surface barrier detector covered with Ni foil at 90° for the (p,α) channel. This analysis concluded that the $E_r^{cm} = 217\,\text{keV}$ resonance has a negligible contribution in the (p,α) reaction. For the other resonance instead only an upper limit was reported, $\omega\gamma_{p\alpha} \leq 5 \times 10^{-7}\,\text{eV}$. Moreover, it was proven that the ratio between the (p,α) and the (p,γ) reactions rate varies significantly below 100 MK due to the uncertainties on the $E_r^{cm} = 138\,\text{keV}$ resonance.

The (p,α) and (p,γ) reactions had to wait until the end of 2004 for further studies to be conducted [16, 18]. The work reported in [16] used an indirect method based on the ^{23}Na$(^3\text{He},d)^{24}$Mg reaction spectroscopy to populate relevant excited states of ^{24}Mg. In this experiment it was used the TUNL 10 MV Tandem accelerator combined with a position sensitive avalanche detector and evaporated NaBr targets to investigate the resonances at $E_r^{cm} = 5, 37, 138, 170\,\text{keV}$. The result relevant here is the $\omega\gamma_{p\alpha} \leq 1.6 \times 10^{-6}\,\text{eV}$. Moreover, the nucleosynthesis network calculations performed in [16] were able to reproduce the O-Na anti-correlation observed in [7]. However, this result is heavily affected by the uncertainties of the 138 keV resonance, suggesting the key to explain the GC observations. The study in [18] focused on the 138 keV resonance for the (p,γ) channel using the LENA 1 MV accelerator on evaporated Na_2WO_4 targets cooled with water. Protons were accelerated in the energy range of 130 – 450 keV and the photons were subsequently detected with a HPGe at 0° in coincidence with an annular NaI(Tl) detector. Together with the new $\omega\gamma_{p\gamma}$ and the branching ratio $(p,\alpha)/(p,\gamma)$ they retrieved a new upper limit for $\omega\gamma_{p\alpha} \leq 1.5 \times 10^{-8}\,\text{eV}$. An year later [19], a study with the same experimental setup reported the same results, except for a greater uncertainty on temperatures relevant for the HBB of AGB stars.

A more recent experiment [20] in 2013, again at LENA, focused on the $E_r^{cm} = 138\,\text{keV}$ resonance and used higher proton energies (up to 550 keV) and thicker targets (up to 50 keV). It obtained a new upper limits for the resonance strength $\omega\gamma_{p\alpha} \leq 8.8 \times 10^{-10}\,\text{eV}$. In Fig. 3.4 I report the ratio between (p,α) and (p,γ) rates in literature.

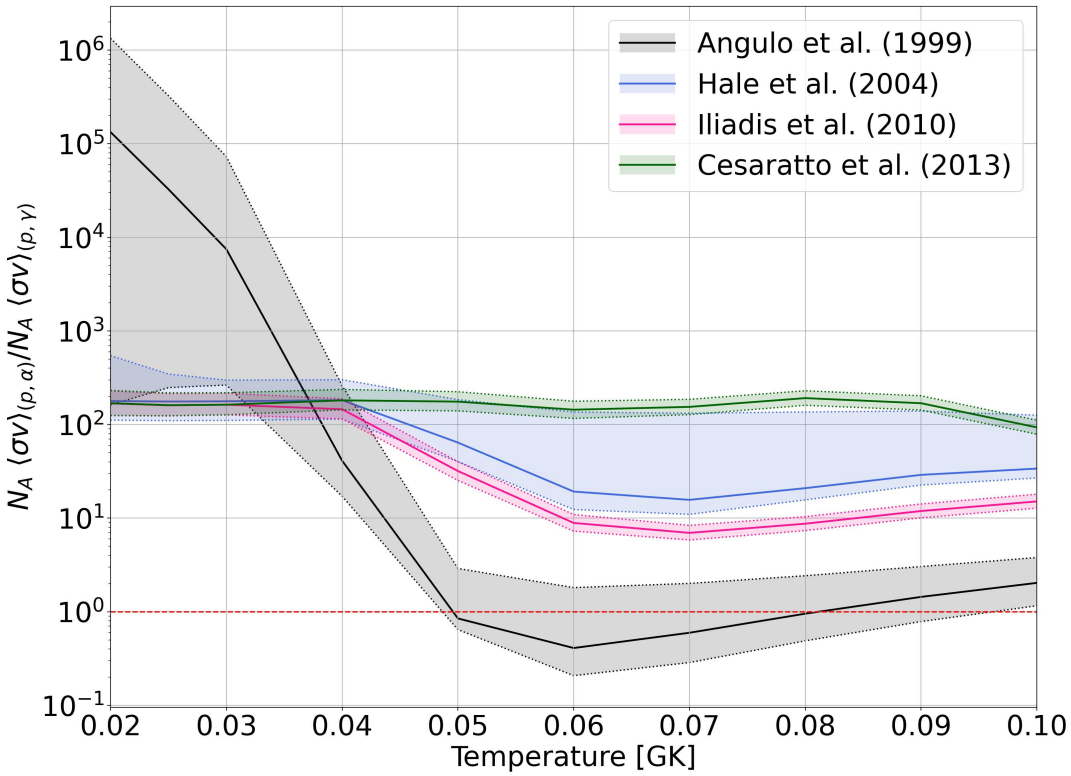

Figure 3.4: Representation of the branching ratio, $(p,\alpha)/(p,\gamma)$, in two nuclear compilations [22, 23] (1999 and 2010) and two measurement campaigns [16, 20] (2004 and 2013) from 1999 to 2013. Each solid line represents the adopted value while the associated shaded area is the uncertainty relative to that measure. With a red dashed line is highlighted the unitary value, points above it are associated to a closed NeNa cycle.

The most recent investigation I discuss was carried out in the 2021 [21]. Despite it focused only on the (p,γ) channel, it is relevant to report this study due to its strong implications on the NeNa cycle. They found a new energy for the $E_r^{cm} = 138\,\text{keV}$ resonance, setting it 5 keV lower than what previously obtained. This has dramatic consequences on the reaction rate, especially in the temperature range of $0.04 - 0.1\,\text{GK}$. The result was an enhancement of the final ^{24}Mg abundance of about 2.5, suggesting that at these temperatures the NeNa cycle is open.

4 Experimental setup

In the upcoming months, the LUNA experiment (Laboratory for Underground Nuclear Astrophysics), located in the Gran Sasso National Laboratories (LNGS) deep inside the Gran Sasso massif is going to measure the $E_r^{cm} = 138\,\text{keV}$ resonance of the $^{23}\text{Na}(p,\alpha)^{20}\text{Ne}$ reaction, exploiting the high current beam from LUNA 400kV accelerator [24, 25, 26] and the reduction of background guaranteed by the underground location [27, 28, 29, 30]. A comparison with the surface background is reported in Fig. 4.1. However, a critical aspect in any nuclear physics experiment is the target stability since it represents one of the main sources of systematic error. In the following I will report on a dedicated study to characterize and test different types of target to find the optimal one for the $^{23}\text{Na}(p,\alpha)^{20}\text{Ne}$ experiment. The experimental setup used for the target characterization is described in the next section.

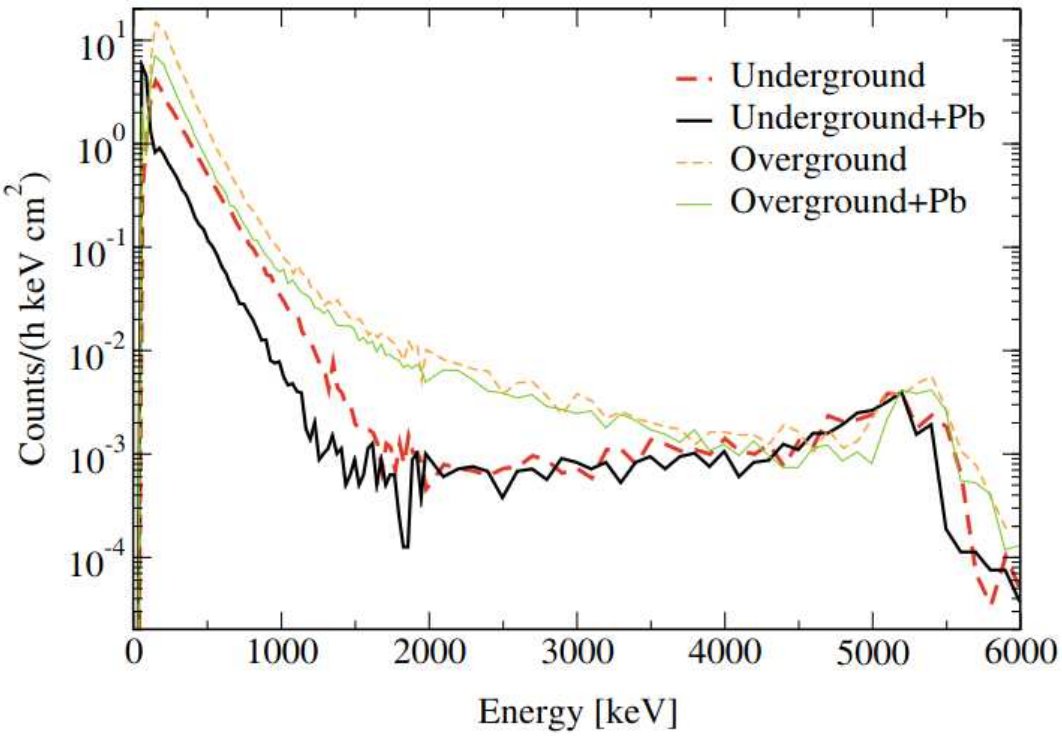

Figure 4.1: Comparison of background spectra taken with and without shielding underground at LUNA and overground at Edinburgh. In the region around 200 keV, the background suppression is up to a factor of 15. The peak around 5 MeV arises from intrinsic α activity in the silicon detectors [28].

4.1 LUNA 400kV accelerator and beamline

The LUNA 400kV setup was manufactured by High Voltage Engineering Europe (HVEE), Netherlands, and has been installed in 2001 to upgrade the former 50 kV accelerator. It consists of a single stage Cockcroft-Walton accelerator that can accelerate H^+ and He^+ particles up to 400 keV of energy. The main features of LUNA 400kV accelerator are the high current (up to 500 µA on target for the H^+ beam [25]), its low beam energy spread

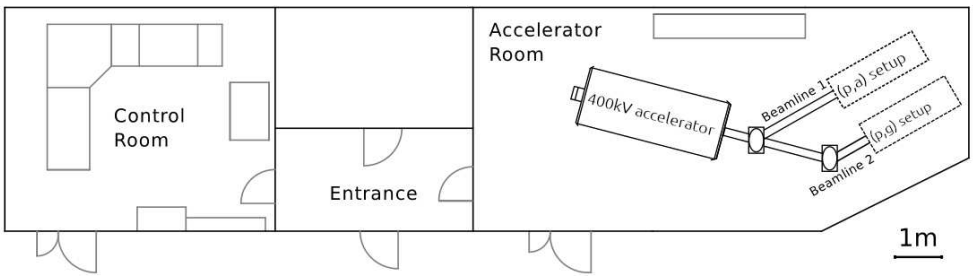

Figure 4.2: Sketch of the floor map of LUNA 400kV facility, currently only the (p, γ) setup is operative. Figure adapted from [31].

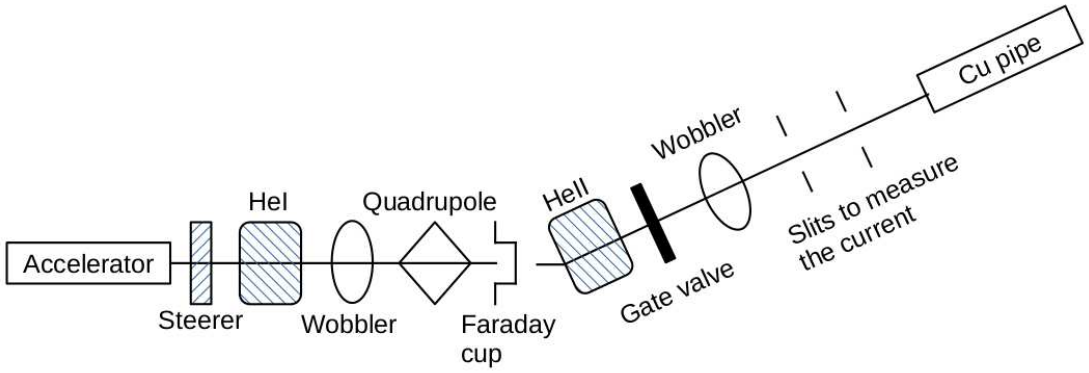

Figure 4.3: Representation of the BL2 from the accelerator to the target chamber, including the focusing and bending elements.

(just 100 eV) and the long-term energy stability over time (5 eV/h). The accelerator uses a radiofrequency (RF) ion source and it is able to provide an ion beam of H^+ at 1 mA or He^+ 500 µA. The beam is therefore accelerated via a voltage difference up to 400 kV and injected into the beamline. The accelerator is embedded in a tank filled with a gas mixture of N_2 and CO_2 at 20 bar to guarantee electric insulation [25].

Two beamlines (BL) are available and presently both operate with solid targets. The first (BL1) will be used to study the $^{23}Na(p, \alpha)^{20}Ne$ reaction while the second (BL2) was used in the target characterization instead. When under operation, the beamline is kept at vacuum with the help of a primary and a turbo pump to achieve a vacuum level of 10^{-7} bar. Many other elements are placed in between the accelerator and the target chamber to direct, focus and collimate the beam on target. An illustration of the LUNA 400kV facility and the BL2 scheme are reported in Fig. 4.2 and 4.3 respectively.

Once the beam exits the accelerator, it encounters a multitude of elements that serve different purposes. A steerer creates an offset along the beam axis and allows to focus it on the target. A couple of magnets (HeI, HeII) to divert the beam onto one of the beamlines (BL1 or BL2). A quadrupole is placed after HeI in order to refocus the beam. After these components, a gate valve is placed to operate on the beamline safely. Two wobblers are present, their function is to continuously move the beam along two directions to spread the beam spot on a larger area of the target surface. A Faraday cup (FC0) is placed after the quadrupole in order to measure the beam current along the beamline.

Before impinging on the target the beam pass through a Cu tube cooled with liquid

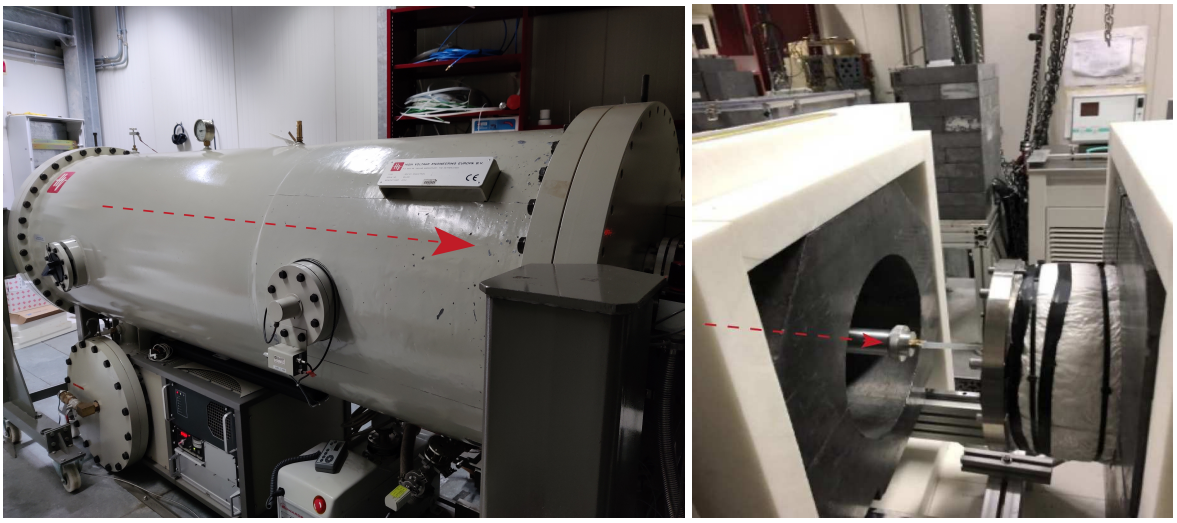

Figure 4.4: Pictures of the LUNA 400kV accelerator (left) and target chamber (right) taken during the second target campaign, at the end of 2023. In both pictures the beam direction is indicated with dashed red arrows.

nitrogen which acts as a cold trap, preventing unwanted ions (mainly carbon) to deposit on the target surface. These atoms may stack up on the target surface causing an energy loss on the beam particles before they reach the layer with the nuclei of relevance for the reaction. This build up of material may also induces reactions which are sources of beam induced-background (like $^{12}C(p,\gamma)^{13}N$). These issues have to be avoided as much as possible since they increase significantly the noise and thereby decrease the signal/noise ratio. Moreover the Cu tube was biased with a negative voltage to push back into the target secondary electrons that will affect the current lectures.

After passing through the Cu tube the beam impinges on the target, which is mounted on a dedicated target holder. Both the target chamber and the target holder are insulated from the beamline in order to directly read the beam current. The target holder allows to water cool the target to prevent target degradation. In Fig. 4.4 is shown the starting and final elements of the beamline, the accelerator and the target chamber.

4.2 Detection systems

During the target characterization campaigns, two kind of detectors have been used to measure the photons generated by the $^{23}Na(p,\gamma)^{24}Mg$ reaction. In the first campaign a HPGe detector was employed, while on the other two campaigns a BGO detector was used. A complete dissertation of the two is beyond the scope of this work, here I will describe briefly the basic physics behind them and focus on their differences.

HPGe HPGe stands for High Purity Germanium and it is often used as detector, this element has semi-conductive properties and when it is irradiated with a ionizing radiation releases charges which can be measured as an electronic signal simply by applying a voltage. It has two main disadvantages. First the germanium has to be cooled to liquid-

nitrogen temperatures in order to neglect the generation of charges by thermal effect (the band gap of Ge is relatively small so it is very likely the promotion of electrons from the valence to the conduction band). Secondly there are physical limit to their size which directly affect the efficiency. The main advantage of using a HPGe detector lies in its excellent resolution, generally much higher than a BGO detector. The one used at LUNA 400kV had a resolution of about 2.2 keV for photons of energy equal to 1.33 MeV (corresponding to a resolution better than 0.2%) [32] and was placed with an angle of 55° with respect to the beam.

BGO This scintillator detector is made of an inorganic crystal of bismuth germanium oxide ($Bi_4Ge_3O_{12}$). Unlike HPGe detector, it can be manufactured in large sizes and, due to its characteristics, it has typically very high efficiencies but worse resolutions, about 12% for photons of 1.274 MeV energy [33]. The LUNA BGO detector consists of 6 crystals arranged in a cylindrical geometry around a cylindric borehole with the target placed at the center. This configuration allows to cover almost the entire solid angle.

4.3 Target types

The aim of the present work is the characterization and test of different sodium targets. Before reporting the details of the type of targets investigated here I will describe the requirements for a solid target:

- Stability. The target material are supposed to be as much as possible chemically and physically stable under the experimental conditions;
- High purity. The target material should be as pure as possible, with minimal contamination from other elements. This minimizes beam induced background;
- Uniformity. The deposited material should be uniform in composition and thickness;
- Specific thickness. The choice of thinner or thicker targets directly affect the measurement;
- Mechanical and electrical properties. The target needs to be able to withstand the bombardment of particles and it must also ensure thermal and electrical conductivity during the experiment.

In the past a wide variety of solid compounds have been used to investigate reactions involving ^{23}Na, from implanted targets [34, 35, 36] to evaporated ones (NaOH [37], NaCl [38], NaBr [39], Na_2WO_4 [39, 40], Na_2SO_4 [41] and $Na_4P_2O_7$ [42]). In a recent study of $^{23}Na(p,\gamma)^{24}Mg$ cross-section, targets of NaCl, Na_2SiO_3 and Na_2WO_4 have been used [13]. Among these, despite some issues with beam induced background from ^{11}B and ^{7}Li, the Na_2WO_4, proved to be the best candidate.

The targets used in the present work were manufactured using two different techniques: evaporation and sputtering of ^{23}Na compounds on a backing material. The first method, used to produce Na_2WO_4 targets, was performed both at the National Laboratories of Legnaro (Italy) and the Institute for Nuclear Research (MTA Atomki, Hungary). The second technique was conducted only at LNL and was used to manufacture $NaNbO_3$ targets.

Both production processes belong to the vapor deposition (PVD) techniques. PVD are processes in which atoms or molecules of a material are vaporized from a solid (or liquid) source and transported in the form of a vapor onto a substrate, where they condense. The low-pressure environment grants to reduce contamination during the process. Typically the deposited layer thickness ranges from few Å to hundreds of nm. An advantage of PDV techniques resides in their versatility since almost any inorganic and most organic compounds can be deposited. In the following I describe the features specifically for the evaporation technique and the sputter deposition [43].

Vacuum evaporation According to this technique, the material from a thermally vaporized source reaches the substrate in a high vacuum environment (10^{-9} mbar). In this configuration, it is possible to approximate the trajectories of evaporated particles to line-of-sight lines from the source surface to the substrate placed above the source. This technique is characterized by higher deposition rate compared to other production techniques ($\approx 10^{-3}$ g/cm^2·s). However, there are also some downsides: only few variables are controlled by the operator and the deposited layer might be non-homogeneous. Particularly relevant to this method, are the substrate adhesive properties since they help improving the uniformity of the deposited layer.

The first three targets produced with this technique were manufactured at LNL and where used during the HPGe phase, while the later four where produced by Atomki and they were characterized in the course of the BGO phase. They consist of Na_2WO_4 molecules evaporated on a Ta disk, moreover those produced on LNL accounted also of a Cr coating or a wafer structure (Cr-Na compound-Cr-Ta backing). This additional surrounding layer was deposited because Na_2WO_4 compound is hygroscopic which leads to the deposition on target surface of moisture from the air and ultimately may alter the target properties and affect the measurements. For the same reason, all evaporate targets where delivered in a jar kept under vacuum.

Sputter deposition This technique consists in the deposition of vaporized atoms from a target surface onto a substrate via physical sputtering process. During the physical sputtering, superficial particles of the target are physically ejected due to momentum transfer with energetic ions (sputtering gas, commonly an inert element like argon). The impinging ion is usually produced by a plasma source and is subsequently guided on the target surface with some magnets. When a target particle is struck by the ion with enough energy,

Table 4.1: List of the analyzed targets, grouped for the detector used to characterize them. In the table the production method is reported.

Detector	Target	Type	Detector	Target	Type
HPGe	LNL1	Evaporated	BGO	ATOMKI2	Evaporated
HPGe	LNL2	Evaporated	BGO	ATOMKI3	Evaporated
HPGe	LNL4	Evaporated	BGO	ATOMKI4	Evaporated
HPGe	LNL6	Sputtered	BGO	LNL101	Sputtered
HPGe	LNL9	Sputtered	BGO	LNL103	Sputtered
BGO	ATOMKI1	Evaporated	BGO	LNL105	Sputtered

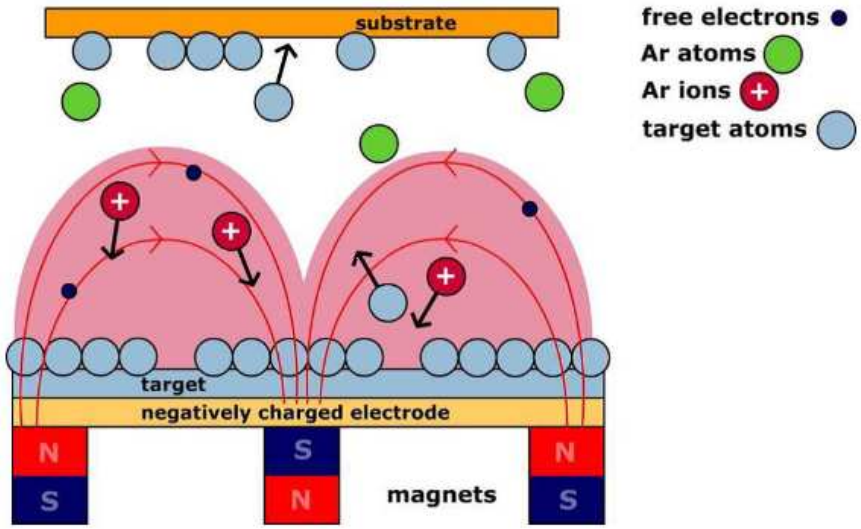

Figure 4.5: Illustration of the magnetron sputtering technique using an argon plasma [44].

it will shake the adjacent ones and induce a collision cascade. Multiple collisions may result in the physical ejection of the surface particle. The incident angle between the ion trajectory and the target surface is important because higher angles will transfer little momentum making the sputtering process ineffective. The environmental pressure plays a critical role too since the it will directly affect the behavior of sputtered particles: in case of low-pressure their energies will be higher and may cause re-sputtering on the substrate surface, in case of high-pressure they will interact with the environment gas particles which will effectively thermalize them to the temperature of ambient gas. The deposition rate is governed by the mass and energy of ion particles, by the angle of incidence and by the strength of chemical bonds between the source atoms. Typically the sputter deposition technique has lower rates than the vacuum evaporation and higher risk of contamination issues. Despite this, it provides higher uniformity and a more stable final geometry.

All the sputtered targets used in this work were manufactured on a Ta backing at LNL using a source target of $NaNbO_3$. An illustration of the production process is reported in Fig. 4.5. Using various time deposition it was possible to produce different thickness targets. A list of all targets used in the this work is reported in Tab. 4.1. In Fig. 4.6 a selection of six targets (three evaporated and three sputtered) before and after irradiation.


LNL2 (bfr)


LNL2 (aft)

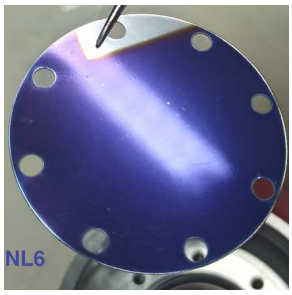

LNL6 (bfr)

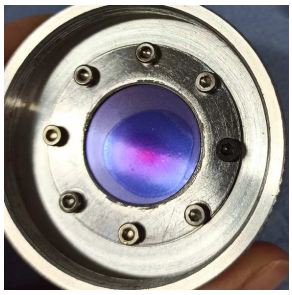
LNL6 (aft)


LNL9 (bfr)


LNL9 (aft)


ATOMKI1 (bfr)


ATOMKI1 (aft)

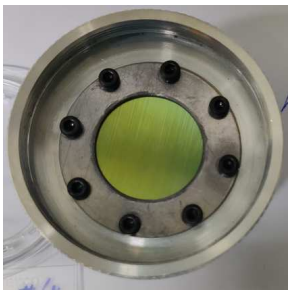
ATOMKI4 (bfr)


ATOMKI4 (aft)


LNL105 (bfr)


LNL105 (aft)

Figure 4.6: Pictures of six targets mounted on their target holders. I report three evaporated targets (LNL2, ATOMKI1 and ATOMKI4) and three sputtered targets (LNL6, LNL9 and LNL105). Each target is shown before (bfr) and after (aft) irradiation. The beamspot is well visible over the target.

5 Characterization procedure

In nuclear physics experiments, targets play a critical role. Understanding the target properties in detail, such as its profile in energies, thickness, uniformity across the surface, chemical composition and eventually the presence of contaminants, is absolutely essential for accurately interpreting the data [45]. In the present work, the Nuclear Resonance Reaction Analysis (NRRA) [46] technique was used to analyze the stoichiometric composition and depth distribution of the targets.

The NRRA exploits the presence of a sharp and isolated resonance in a nuclear reaction that involve either the isotope or one of the isotope in the compound of interest. As reported in Section 2, the resonant cross-section can be described by the Breit-Wigner formula (2.15). Projectiles with energy $E_p < E_r$ will not populate the resonant state in any layer of the target. As they are emitted at $E_p \approx E_r$ the resonance will be populated on the surface of the target. At higher energies $E_p > E_r$ the beam penetrating the target will slow down and will eventually match the condition $E_p \approx E_r$ inside the target. In this way, impinging particles with energy higher than the resonance E_r give place to the reaction on a deeper layer of the target. Since the target is not infinitely thick, beyond an energy threshold the impinging particles will be simply too energetic to be slowed down enough to populate the resonance of interest. By increasing energy in step and acquiring data for each step it is possible to obtain the yield curve. This curve represents the target profile from which one could get information like the target thickness and composition. Its main features are the plateau (which height is associated the target stoichiometry) and a FWHM (related to target thickness). Whenever one of these two quantities vary, because of the target degradation by the beam, it will be directly displayed in the yield curve. The $^{23}\mathrm{Na}(p,\gamma)^{24}\mathrm{Mg}$ reaction has been chosen since it involves ^{23}Na nuclei and have a well known resonance at $E_r^{lab} = 309\,\mathrm{keV}$ [26].

The following section will focus firstly on some basic properties of the $^{23}\mathrm{Na}(p,\gamma)^{24}\mathrm{Mg}$ resonance at $E_r^{lab} = 309\,\mathrm{keV}$. A short summary of the laboratory procedure applied during the measurement follows. Then I will describe the analysis steps: from the energy calibration to the yield computation.

5.1 The $^{23}\mathrm{Na}(p,\gamma)^{24}\mathrm{Mg}$ reaction

The $^{23}\mathrm{Na}(p,\gamma)^{24}\mathrm{Mg}$ reaction is a proton capture that generates an excited ^{24}Mg nucleus that will subsequently decay by γ-emission. It represents the entrance channel for elements that will be processed by the MgAl cycle. This reaction Q-value is set at $(11\,692.696 \pm 0.013)\,\mathrm{keV}$ [14]. We used the $E_r^{lab} = 309\,\mathrm{keV}$ [40, 47] resonance, therefore with the NRRA technique we aimed at populating the excited level $E_x = 11\,988\,\mathrm{keV}$ and investigated each target with a proton beam at energies spanning roughly from $E_p = 308\,\mathrm{keV}$ to $380\,\mathrm{keV}$.

From the reported excited level, a ^{24}Mg nucleus can emit up to 12 different γ rays with energy ranging from $1257.4\,\mathrm{keV}$ to $11\,988.5\,\mathrm{keV}$. I retrieved the associated 45 decay

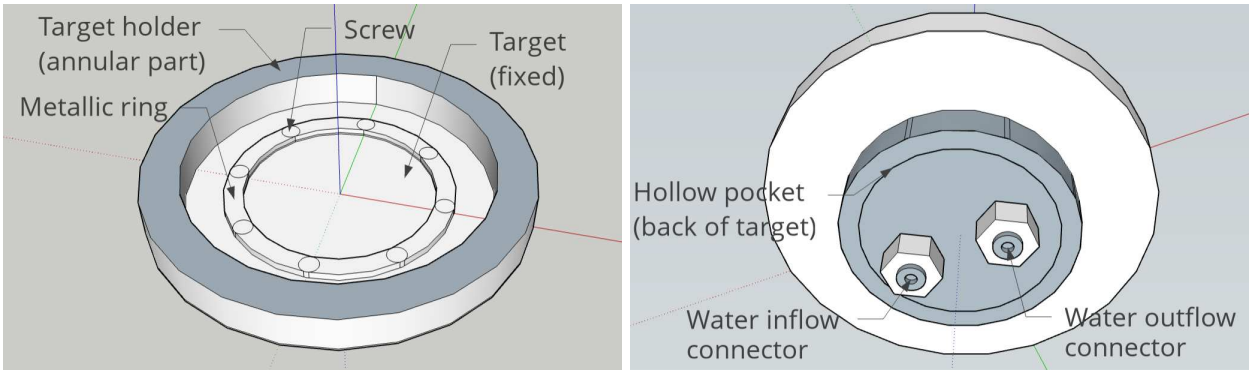

Figure 5.1: Illustrative pictures of the target holder used to mount the target on the beamline, on left the top-view while on right the bottom-view. The blue vertical line represents the beam axis.

cascades from the $E_x = 11\,988\,\text{keV}$ excited level, they are reported in Table A.2 with the related emission probabilities, branching ratios. In the same table, the most probable decay cascades for each initial γ ray are highlighted in gray. The associated resonance strength $\omega\gamma$ of the 309 keV resonance is known with an uncertainty lower than 20% and is set at $(0.105 \pm 0.019)\,\text{eV}$ [13].

5.2 Data acquisition

As first step of the characterization procedure a scan was performed on fresh target, then scans alternated with long runs (generally at higher currents) were completed to monitor the target profile with accumulate charge. Each scan is composed of several runs at different beam energies. We started with a run falling right before the resonance energy E_r and then we increased the beam energies in steps. To check the presence of possible contaminants, runs of some hours have been launched at resonances of the $^{19}\text{F}(\text{p},\alpha\gamma)^{16}\text{O}$ and the $^{11}\text{B}(p,\gamma)^{12}\text{C}$ reactions, which are the most common contaminants. The target was exchanged whenever its plateau was not evident any more or its profile presented abnormal characteristics. The targets were fixed on the beamline with custom target holders, see Fig. 5.1. Four target holders have been used in order to speed up the target change operation and neglect any operator-induced variable when mounting the target.

The charge of each run was obtained with a digital integrator which output is in µC. The spectra obtained by the detector, were processed and showed with a CAEN software (CoMPASS) which allows to perform an online analysis and to get a preliminary target profile during the scan, for a given region of interest (ROI). For each run, a `root` file with the spectrum was saved for later analysis. For each run the charge, current, energy beam and counts in the ROI were inserted in an `xlsx` file. Moreover, an E-Log was compiled to show the target profile, describe potential issues with it and explain the final decision to continue the analysis or change the target. Every time the accelerator was set up for a long run, a technical E-Log to keep track of machine set parameters was prepared.

5.3 Data analysis

5.3.1 Energy calibration

Once the data acquisition at LUNA 400kV was completed, the spectra are ready to be analyzed. However, before starting the targets analysis, one should firstly calibrate the spectra in energies. They are provided in the root format, each detector channel (one for the HPGe and six for the BGO) is composed by 16385 channels. The calibration allows to associate to each channel an energy value.

I selected some suitable lines relevant to the ^{23}Na$(p,\gamma)^{24}$Mg reaction. These lines are associated to an appropriate E_γ value from those reported in Table A.2. Due to the different resolution characteristics of HPGe and BGO, I could selected 8 and 4 lines, respectively covering the γ energy range of interest. The energy values of these lines are reported in Tab. 5.1.

To get the channel to be associated with the expected E_γ, for the HPGe I selected for each peak region of interest the channel with the highest counts. In the case of the BGO spectra, due to its poor resolution, I fitted the peak with a Gaussian and a linear background. An exemplification of this Gaussian fit is reported in Fig. 5.3 for the BGO crystal 3 of run 211 with LNL101 target. Once the channels for each line has been identified, all are plotted against the selected energies E_γ and, since the calibration was pretty stable for each target, I obtained the calibration function only from long runs (thus with high statistics). For the HPGe calibration, I used a linear fit and calibrated each target separately using its long runs. The calibration results for long run 96 (LNL6) is shown in Fig. 5.2. A different strategy was used with the BGO, its linearity is granted only up to $E_\gamma = 8\,\text{MeV}$, therefore I adopted a function linear until 8 MeV and quadratic beyond this value:

$$\begin{cases} y = mx + q & x < 8\,\text{MeV} \\ y = a(x-k)^2 + m(x-k) + mk + q & x \geq 8\,\text{MeV} \end{cases} \tag{5.1}$$

where x is the energy in MeV, y is the channel, $k = 8\,\text{MeV}$ is the shift coefficient while m, q and a are free parameters. The LUNA BGO detector gives in output six spectra (one for each crystals), therefore I calibrated each of them separately and only after the calibration I summed everything in a single spectrum. This allowed to increase the statistics. Moreover, since the BGO campaigns required two separate shifts and were affected by some minor inconveniences, I opted to calibrate each scan separately using a run placed on the yield plateau. The calibration results for run 211 (LNL101) in each crystal is shown in Figure and 5.4. The exact values of fit parameters for both HPGe and BGO are reported in Table A.1.

Table 5.1: Energy values of the γ used to calibrate spectra in HPGe and BGO campaigns.

Detector	E_γ [keV]	Detector	E_γ [keV]	Detector	E_γ [keV]
HPGe	1368.6	HPGe	7748.8	BGO	1368.6
	3122.8		8436.8		4240.4
	6378.1		10617.3		7748.8
	6752.3		11985.3		10617.3

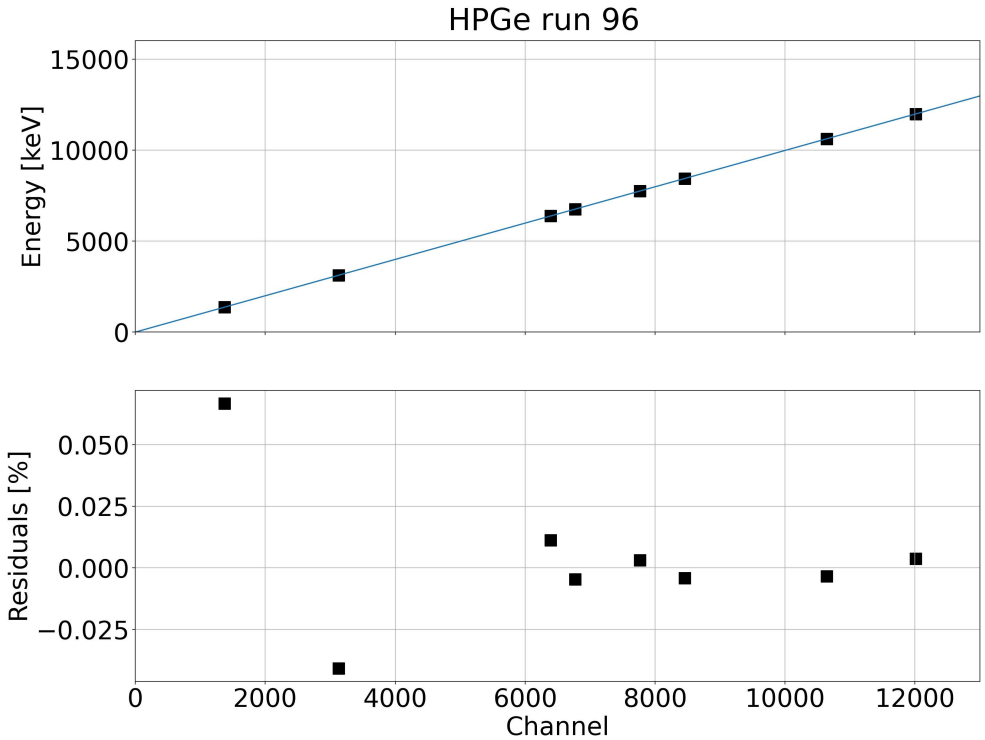

Figure 5.2: Top plot: HPGe calibration for the run 96 (LNL6). Bottom plot: relative residuals defined as $(E - E_{\text{fit}})/E$.

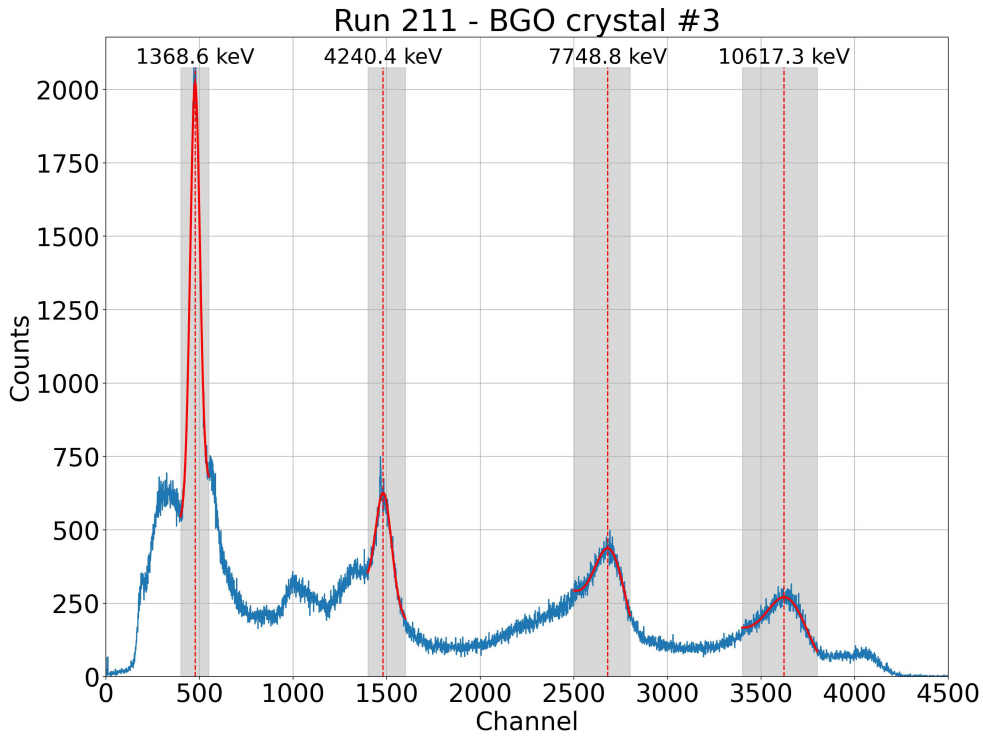

Figure 5.3: Channel determination for the four BGO lines of crystal 3 of run 211 (LNL101). A Gaussian fit with a linear background was used to determine the peak channels. In blue is represented the crystal 3 spectrum, the red solid line is the fit while the red dotted line highlights the channel used for the calibration. The gray shaded areas refers to the channel ranges used in the fit.

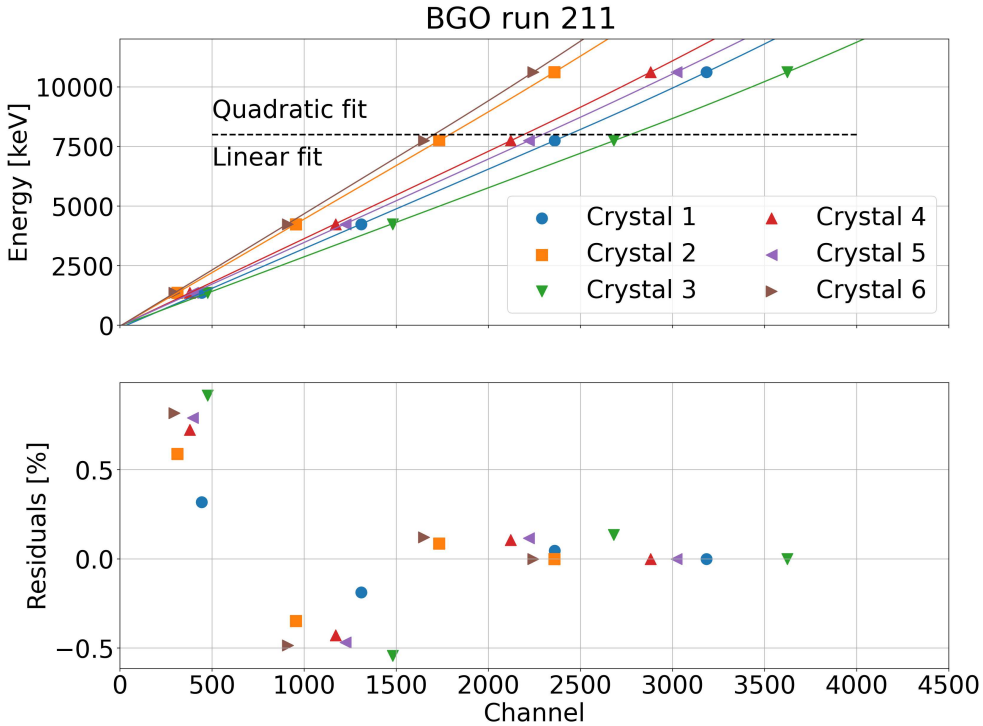

Figure 5.4: Top plot: BGO calibration for all 6 crystals of run 211 (LNL101). The black dotted line separates the linear from the quadratic part of the fit Eq. (5.1). Bottom plot: relative residuals defined as $(E - E_{\text{fit}})/E$.

5.3.2 Peak areas determination

To get the area of the peaks from the $^{23}\mathrm{Na}(p,\gamma)^{24}\mathrm{Mg}$ resonance at 309 keV I applied the Covell method [48]. It is a simple technique, used in nuclear physics to analyze γ-ray spectra, which approximates the background underneath a peak as linear. Using C_i to refer at the counts associated to the i-th bin, the net peak area identified with the region of interest between L and U channels, can be computed as:

$$A = \sum_{i=L}^{U} C_i - \left(\sum_{L-m_L}^{L-1} C_i + \sum_{U+1}^{U+m_U} C_i \right) \frac{n}{m_L + m_U} \tag{5.2}$$

where n is the width related to the peak region, m_U and m_L are the widths associated respectively to the upper and lower background regions. The error on net peak area A measure retrieved via Covell method is given by the following expression:

$$\sigma_A = \sqrt{A + B\frac{1+n}{m_L + m_U}} \tag{5.3}$$

where B is the second term of Eq. (5.2). An application of this procedure is reported in Fig. 5.5.

5.3.3 Yield and stopping power

The experimental yield could be defined as the ratio between the net counts N_γ for a specific γ-ray of interest and the accumulated charge Q:

$$Y = \frac{N_\gamma}{Q} \quad [\mu\mathrm{C}^{-1}] \tag{5.4}$$

this expression has been used in the present work to derive informations about the target thickness, the degradation over successive scans and compare different types of targets. A yield profile is reported in Fig. 5.6.

The yield can also be used to retrieve informations about the targets stoichiometry. In this case, the correct expression to be used is the following:

$$Y = \frac{\mathcal{N}}{N_p \cdot W_\gamma(\theta)} \tag{5.5}$$

where $\mathcal{N}$ is the number of reactions, $W_\gamma(\theta)$ is the angular distribution of the observed γ emission and N_p is the number of impinging particles, estimated from the charge using $N_p = Q/e$ with $e = 1.602\,18 \times 10^{-13}\,\mu\mathrm{C}$ the elementary charge.

In order to retrieve the number of reactions $\mathcal{N}$ from the analysis of a particular γ-ray, the summing effects should be accounted. They are crucial for high-efficiencies or close detector-source geometries (like the ones we used at LUNA 400kV). In a simple case we

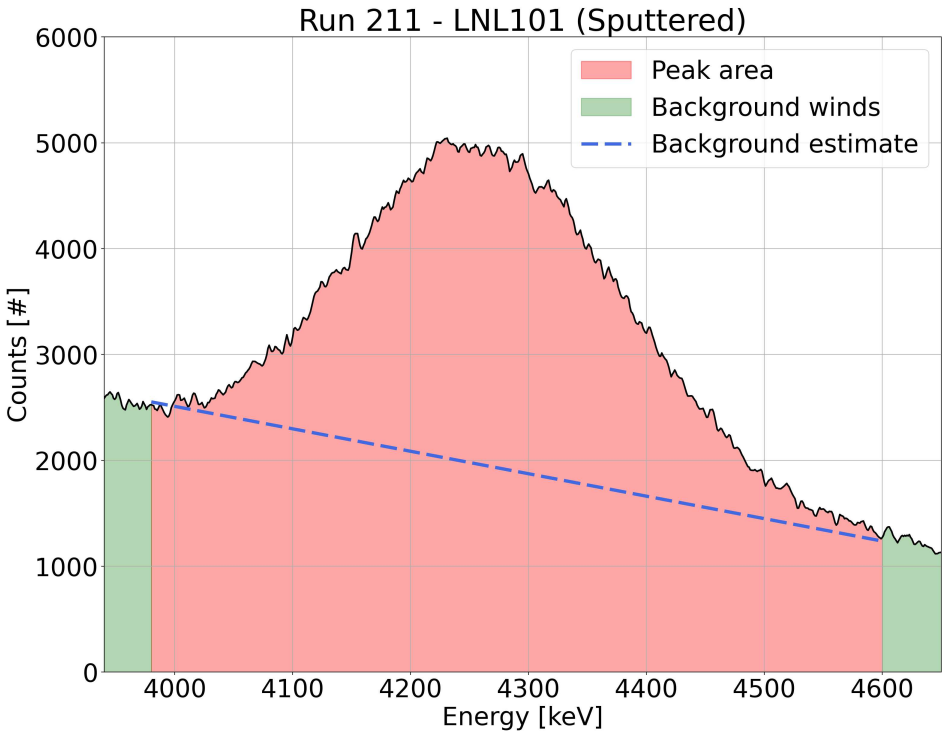

Figure 5.5: Application of the Covell method to the 4240.4 keV line of the run 211 (LNL101). In red I shaded the selected peak region and in green the background wings, the blue dashed line it is indicated the background estimation using the Covell method.

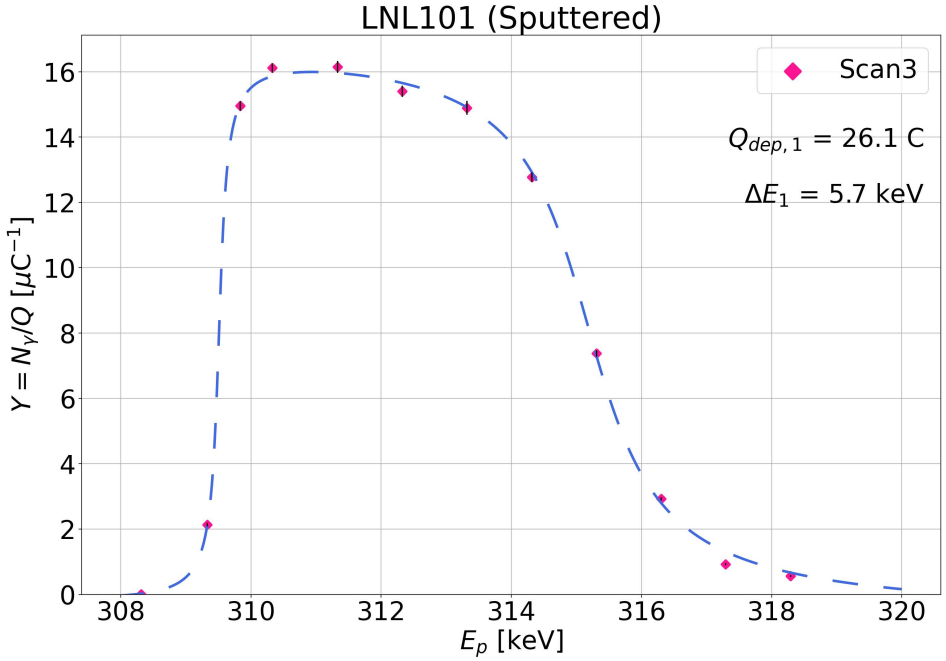

Figure 5.6: Yield profile of the 10 617 keV line for the 3rd scan of LNL101 target. The diamonds represent the computed yields, the vertical black lines are their uncertainties. The deposited charge at the start of the scan and the ΔE obtained by fitting the yield with Eq. (5.10) (dashed line) are reported on the right-hand-side.

Table 5.2: Efficiency parameters used in the course of this work, courtesy of [49].

A	a	b [keV^{-1}]	c [keV^{-2}]	$k1$	$k2$ [keV^{-1}]	$k3$ [keV^{-2}]
0.0379	-0.68 ± 0.02	-0.34 ± 0.02	-0.191 ± 0.009	-1.9 ± 0.2	-1.7 ± 0.3	7 ± 1

may consider three levels: 0 (ground), 1 (intermediate level) and 2 (exited level). The nucleus in the excited state 2 can decay towards the ground state either by emitting γ_{21} followed by the emission of γ_{10} or by emitting a single γ_{20}. The intermediate level can only decay to the ground state with a γ_{10} emission. It may happen that the γ_{21} and γ_{10} are detected together within the time resolution window of the HPGe detector (200 ns) which will read them as a unique γ_{20}. This results in a lower counts for γ_{21} and γ_{10} and a higher counts for γ_{20}. In this simple case, indicating with $\mathcal{N}_{ij}$ the number of detected γ_{ij}, it is possible to state [6]:

$$\begin{aligned} \mathcal{N}_{21} &= \mathcal{N} B_{21} \eta_{21}^{\mathrm{P}} - \mathcal{N} B_{21} \eta_{21}^{\mathrm{P}} \eta_{10}^{\mathrm{T}} = \mathcal{N} B_{21} \eta_{21}^{\mathrm{P}} \left(1 - \eta_{10}^{\mathrm{T}}\right) \\ \mathcal{N}_{10} &= \mathcal{N} B_{21} \eta_{10}^{\mathrm{P}} - \mathcal{N} B_{21} \eta_{10}^{\mathrm{P}} \eta_{21}^{\mathrm{T}} = \mathcal{N} B_{21} \eta_{10}^{\mathrm{P}} \left(1 - \eta_{21}^{\mathrm{T}}\right) \\ \mathcal{N}_{20} &= \mathcal{N} B_{20} \eta_{20}^{\mathrm{P}} + \mathcal{N} B_{21} \eta_{21}^{\mathrm{P}} \end{aligned} \qquad \begin{aligned} &\text{Summing out} \\ &\\ &\text{Summing in} \end{aligned} \tag{5.6}$$

where η_{ij}^{P} and η_{ij}^{T} are respectively the photo-peak and total efficiencies of a given γ_{ij}, $\mathcal{N}$ is the total number of decaying photons and B_{ij} is the branching ratio relative to the cascade of interest. By applying Eq. (5.6) to a specific cascade in the 309 keV decay scheme (in Table A.2), that accounts only two γ emissions, one can recover the corrected counts $\mathcal{N}$. The efficiencies to be used in Eq. (5.6) are expressed by the following:

$$\begin{aligned} \eta^{\mathrm{P}}(E_\gamma) &= A \cdot \exp\left(a + b \cdot (\ln E_\gamma) + c \cdot (\ln E_\gamma)^2\right) \\ \ln\left(\frac{\eta^{\mathrm{P}}(E_\gamma)}{\eta^{\mathrm{T}}(E_\gamma)}\right) &= k1 + k2 \cdot (\ln E_\gamma) + k3 \cdot (\ln E_\gamma)^2 \end{aligned} \tag{5.7}$$

this treatment could be performed only for the HPGe since its efficiencies have been retrieved in a previous measurement with the same setup [49]. The efficiency parameters are reported in Tab. 5.2.

The Eq. (5.4) and (5.5) are equivalent, but the latter one can be related to the cross-section σ in case of a narrow resonance via the following relation:

$$Y = \int_{E_p - \Delta E}^{E_p} dE \, \frac{\sigma(E)}{\mathcal{E}_{\mathrm{eff}}(E)} = \int_{E_p - \Delta E}^{E_p} dE \, \frac{1}{\mathcal{E}_{\mathrm{eff}}(E)} \frac{\lambda^2}{4\pi} \omega\gamma \frac{\Gamma}{(E_{\mathrm{r}} - E)^2 + (\Gamma/2)^2} \tag{5.8}$$

moreover, it is not reductive (since we are dealing with a narrow resonance) to suppose that the effective stopping power and the de Broglie wavelength are constants in the resonance width. This allows us to extract them from the integral and evaluate them at the

resonance energy. The remaining integral admits analytical solutions, leading to:

$$Y = \frac{\lambda_r^2}{2\pi}\frac{\omega\gamma}{\mathcal{E}_{\mathrm{eff,r}}}\left[\arctan\left(\frac{E_p - E_r}{\Gamma/2}\right) - \arctan\left(\frac{E_p - E_r - \Delta E}{\Gamma/2}\right)\right] \tag{5.9}$$

where the quantity Γ represents the resonance width. In order to retrieve an optimal estimation of the target thickness, the profile should be fitted with an opportune parametric expression. In the course of this work, I adopted a parametric version of the Eq. (5.9):

$$Y = H + k_0 \cdot \arctan\Big[s_0 \cdot (E_p - x_0)\Big] - k_1 \cdot \arctan\Big[s_1 \cdot (E_p - x_1)\Big] \tag{5.10}$$

where H, k_i, s_i and x_i are free parameters and E_p is the proton energy. By comparing the arguments of the arctan terms, it is evident that x_0 and x_1 are associated respectively to E_r and $E_r + \Delta E$, therefore it is possible to retrieve the target thickness ΔE simply as $x_1 - x_0$. It has been verified that the x_0 parameter was always compatible to 309 keV.

Without losing the scope of this work, Eq. (5.9) can be approximated in the limit of infinitely thick targets and retrieve the maximum value (set $\Delta E \to \infty$ and $E_p \gg E_r$):

$$Y_{\mathrm{max},\Delta E\to\infty} = \frac{\lambda_r^2}{2}\frac{\omega\gamma}{\mathcal{E}_{\mathrm{eff,r}}} \tag{5.11}$$

where the quantity $Y_{\mathrm{max},\Delta E\to\infty}$ represents exactly the yield in the plateau region. The de Broglie wavelength λ_r has been calculated as follows:

$$\frac{\lambda_r^2}{2} = \left(\frac{M_0 + M_1}{M_1}\right)^2 \frac{4.125\times10^{-18}}{M_0 \cdot E_r^{\mathrm{lab}}} \quad [\mathrm{cm}^2] \tag{5.12}$$

with M_0 and M_1 the mass of projectile and target nuclei in [u] and E_r^{lab} in [eV]. From Eq. (5.11), knowing the yield on the plateau, it is possible the laboratory effective stopping power $\mathcal{E}_{\mathrm{eff}}^{\mathrm{LAB}}$. The stopping power $\mathcal{E}$ is defined as the energy loss per unit of areal density ($[\mathcal{E}] = \mathrm{eV}/10^{15}\mathrm{atoms/cm}^2$) and it depends on both beam and target particles. Therefore it encodes the information about the stoichiometry. For a compound A_xB_y where A is the active nucleus that participates in the reaction and B all the remaining nuclei, the effective stopping power $\mathcal{E}_{\mathrm{eff}}$ reads:

$$\mathcal{E}_{\mathrm{eff}} = \mathcal{E}_A + \sum_B \frac{n_B}{n_A}\mathcal{E}_B \tag{5.13}$$

where the $\mathcal{E}_i$ and n_i terms are the stopping power and the number per square centimeter of each atomic species in the compound. Inserting in Eq. (5.13) the proper values from [50], I calculated the nominal effective stopping powers $\mathcal{E}_{\mathrm{eff}}^{\mathrm{NOM}}$ of the two compounds used in this work, they are reported in Tab. 5.3.

Table 5.3: Stopping power $\mathcal{E}$ and effective stopping power $\mathcal{E}_{\text{eff}}^{\text{NOM}}$ of the nuclei relevant in this work. All values are in eV/10^{15}atoms/cm^2 and have been retrieved from [50].

$\mathcal{E}$(Na)	$\mathcal{E}$(W)	$\mathcal{E}$(Nb)	$\mathcal{E}$(O)	$\mathcal{E}_{\text{eff}}^{\text{NOM}}(NaNbO_3)$	$\mathcal{E}_{\text{eff}}^{\text{NOM}}(Na_2WO_4)$
0.4	31.3	30.0	10.8	62.7 ± 2.0	37.5 ± 1.4

6 Results

This section is dedicated at showing the results of NRRA technique applied to the 12 considered targets. Firstly I will discuss the results of the HPGe campaign, with a special attention to LNL6 and LNL9 target characterization. Then I will report the results for the BGO campaign, mainly focused on target degradation and contaminant investigation.

6.1 The HPGe campaign

For the following analysis I focused on two γ-rays, respectively those at 7748.8 keV and 10617.3 keV. They were chosen either because they represents the two main emissions from the $E_x = 11\,988.5$ keV excited state and they are associated to simple cascades:

$$11988.5 \xrightarrow[46.08\%]{7748.8} \begin{cases} 4238.4 \xrightarrow[21.75\%]{2869.5} 1368.7 \xrightarrow[100.0\%]{1368.6} \mathrm{GS} \\ 4238.4 \xrightarrow[78.25\%]{4238.0} \mathrm{GS} \end{cases} \qquad (6.1)$$
$$11988.5 \xrightarrow[28.11\%]{10617.3} 1368.7 \xrightarrow[100.0\%]{1368.6} \mathrm{GS}$$

where I indicated with GS the ground state. The numbers above and underneath each arrow represent respectively the γ-ray energy and its probability.

The yields, computed as N_γ/Q, of these two γ-rays for all the targets studied during the HPGe campaign are shown in Fig. 6.1 and 6.2. I report also the deposited charge at the beginning of each scan. The ranges used in the Covell method to get the peak areas are reported in Table A.3.

The three evaporated targets, namely LNL1, LNL2 and LNL4, produced at LNL show an irregular profile, such as the plateau structure in LNL1 and LNL2 and the long tail towards high energies in all of them (probably due to sodium diffusion into the backing), and an unstable profile with accumulated charge, see the case of LNL4.

The LNL6 and LNL9 targets were produced through the sputtering technique. Unfortunately, because of time constrain, it was not possible to test the endurance of LNL9. However, LNL6 shows the expected profile which was proven to be stable up to about 15 C of accumulated charge.

For LNL1 and LNL2, due to the structures in their profiles, it was not possible to determine the target thicknesses. In Tab. 6.1 it is reported the target thickness for the remaining three targets retrieved by fitting each scan, when possible, with (5.10).

6.1.1 Effective stopping power

For the LNL6 and LNL9 targets, which present a flat plateau, I could estimate the observed effective stopping power $\mathcal{E}_{\mathrm{eff}}^{\mathrm{LAB}}$, to be compared with the nominal one $\mathcal{E}_{\mathrm{eff}}^{\mathrm{NOM}}$. The results of the calculations are reported in Tab. 5.3. Before using Eq. (5.11) to retrieve the $\mathcal{E}_{\mathrm{eff}}^{\mathrm{LAB}}$, I had

Table 6.1: Target thickness ΔE (in keV) for the HPGe analyzed lines. To retrieve these values, the Eq. (5.10) was used in the fit. Whenever a scans profile had peculiar characteristics that prevented estimating its ΔE, – is reported.

Line	Target	Scan 1	Scan 2	Scan 3
7748.8 keV	LNL4	37.6 ± 2.1	–	–
	LNL6	6.2 ± 0.1	5.9 ± 0.2	5.7 ± 0.2
	LNL9	4.1 ± 0.1		
10 617.3 keV	LNL4	35.8 ± 2.8	–	–
	LNL6	6.4 ± 0.1	5.8 ± 0.2	5.7 ± 0.2
	LNL9	4.1 ± 0.1		

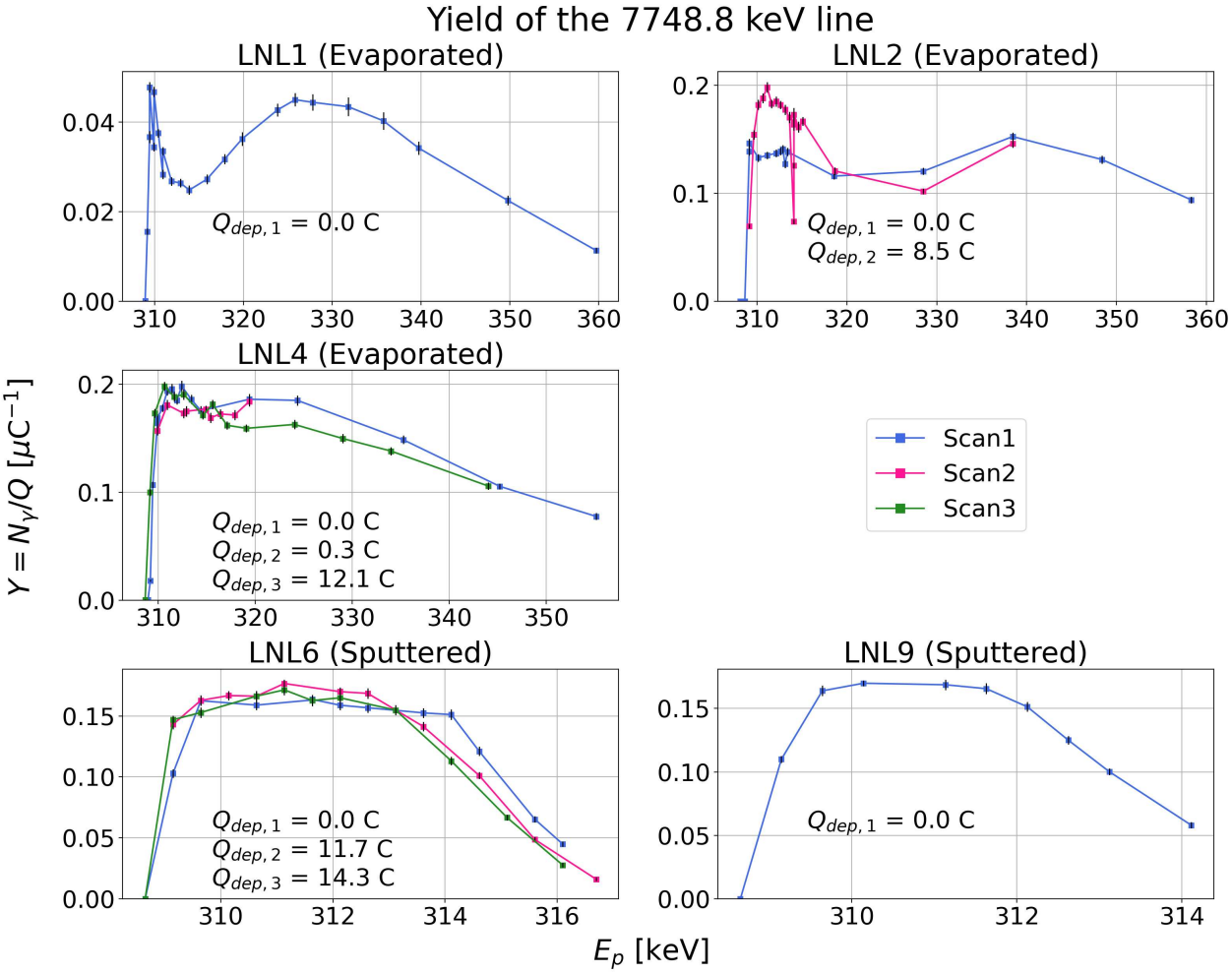

Figure 6.1: Yield profiles for 7748.8 keV line. Each scan is associated to a different color and its deposited charge is reported. The uncertainties are shown as vertical black lines.

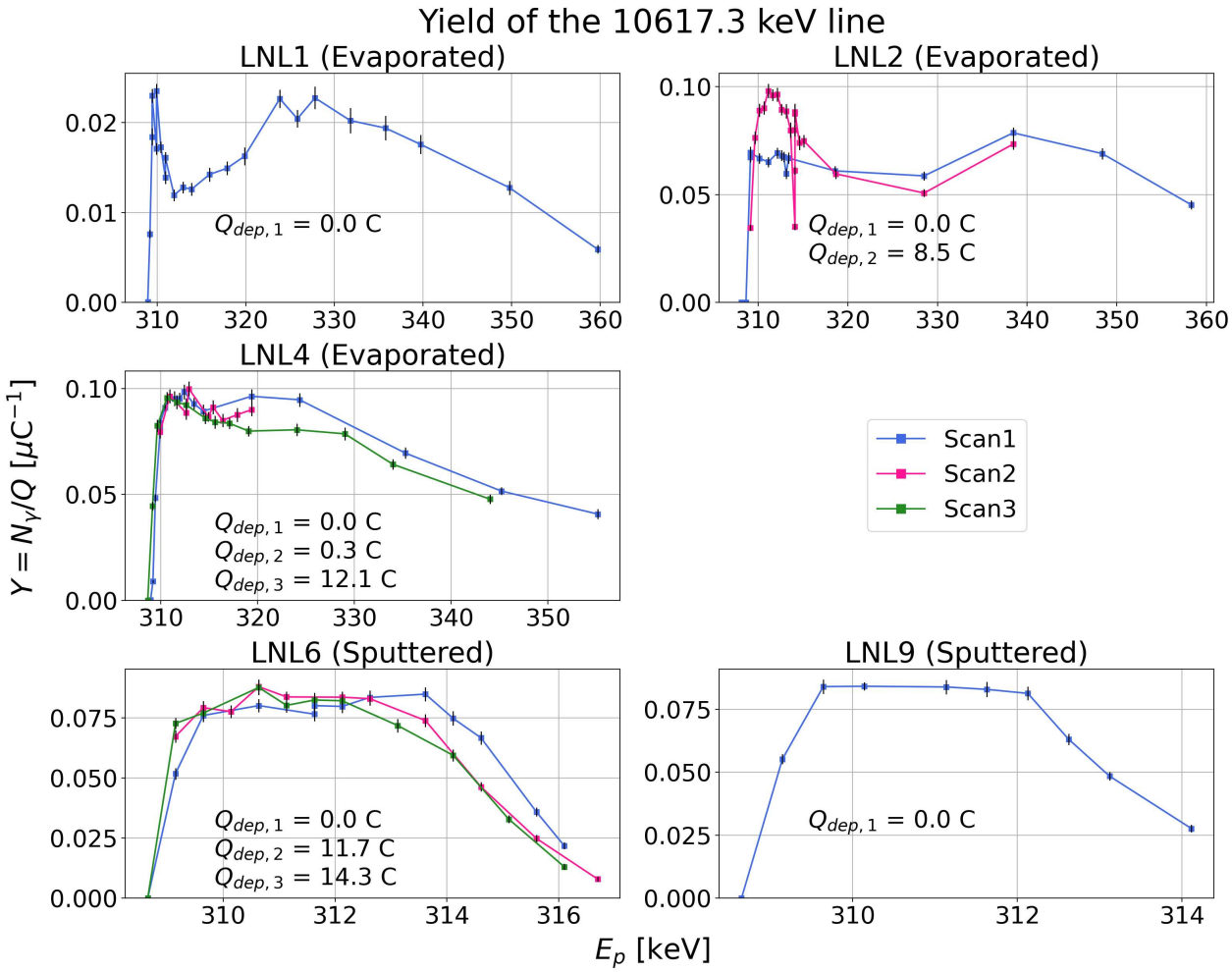

Figure 6.2: Yield profiles for 10 617.3 keV line. Each scan is associated to a different color and its deposited charge is reported. The uncertainties are shown as vertical black lines.

Table 6.2: Angular coefficients and value of the terms involved in the summing correction for the two considered lines in the HPGe study.

Line	a_2	a_4	$W(55°)$	η^{P}_{21}	η^{T}_{10}	B_{21}	B_{10}
7748.8 keV	−0.157	−0.005	1.0164	4.30×10^{-3}	2.81×10^{-7}	46.08%	78.25%
10617.3 keV	−0.183	0.000	1.0012	2.61×10^{-3}	9.70×10^{-2}	28.11%	–

to calculate the number counts corrected by summing effects $\mathcal{N}$. The correction formula depends on the decay cascade: for the one that involves the 10617.3 keV emission I used the first of Eq. (5.6) while for the other that consider the 7748.8 keV emission I applied a similar expression corrected for the branching of the dominating secondary γ-rays:

$$\mathcal{N}_{21} = \mathcal{N} B_{21} B_{10} \eta^{\mathrm{P}}_{21} \left(1 - \eta^{\mathrm{T}}_{10}\right) \tag{6.2}$$

that accounts for the fact that, after the first 7748.8 keV emission, a second 4238.0 keV γ-ray is emitted with $B_{10} = 78.25\%$ (see Eq. (6.1)). In principle Eq. (6.2) should also contains another corrective term for the cascade $4238.4 \rightarrow 1368.7 \rightarrow \mathrm{GS}$, however the detection of these three γ (emitted in succession) within the detector time resolution window is unlikely and its relevance was neglected for simplicity.

With the corrected number of counts I could retrieve the new yield by using Eq. (5.5). In this expression, the angular distribution $W(\theta)$ should be known. In general it can be expressed as:

$$W(\theta) = 1 + a_2 P_2(\cos\theta) + a_4 P_4(\cos\theta) \tag{6.3}$$

where $P_i(\cos\theta)$ are the Legendre polynomials and a_i angular coefficients. The value of a_2 and a_4 are reported in Tab. 6.2 and are taken from [38]. The angular distribution correction was calculated at $\theta = 55°$, the position of the HPGe detector. Finally, the resonance strength to be inserted in Eq. (5.11) is $\omega\gamma_{309} = (105 \pm 19)\,\mu\mathrm{eV}$ [13]. The new yield profiles are shown in Fig. **??**.

I used only the first scan, corresponding to the fresh target, of LNL6 and LNL9 targets to calculate the effective stopping power $\mathcal{E}^{\mathrm{LAB}}_{\mathrm{eff}}$. For each target I identified the yield data on the plateau, see Fig. 6.3 and 6.4, and calculated the $Y_{\mathrm{max},\Delta E\to\infty}$ in Eq. (5.11) as the average of these data. The analysis was performed using both scans obtained via analysis of the $E_\gamma = 10617.3\,\mathrm{keV}$ and 7748.8 keV. In table 6.3 the averages are reported and compared with the nominal value for $NaNbO_3$ compound. The measured effective stopping power is higher than the nominal. This testimonies that the compound must retain a different chemical composition. Among the nuclei involved in the $NaNbO_3$ compound, only the O may be higher because present in the atmosphere of the sputtering chamber. Under the assumption of a higher O abundance, to obtain similar $\mathcal{E}^{\mathrm{LAB}}_{\mathrm{eff}}$ the chemical formula of the compound must range from $NaNbO_{5.17}$ to $NaNbO_{5.98}$.

Table 6.3: Laboratory effective stopping power $\mathcal{E}_{\text{eff}}^{\text{LAB}}$ retrieved from the considered lines for LNL6 and LNL9 targets. The nominal $\mathcal{E}_{\text{eff}}^{\text{NOM}}$ is reported too.

Target	$\mathcal{E}_{\text{eff}}^{\text{LAB}}$		$\mathcal{E}_{\text{eff}}^{\text{NOM}}$
	7748.8 keV	10 617.3 keV	
LNL6	94.7 ± 17.3	90.2 ± 16.6	62.7 ± 2.0
LNL9	89.8 ± 16.4	86.1 ± 15.8	

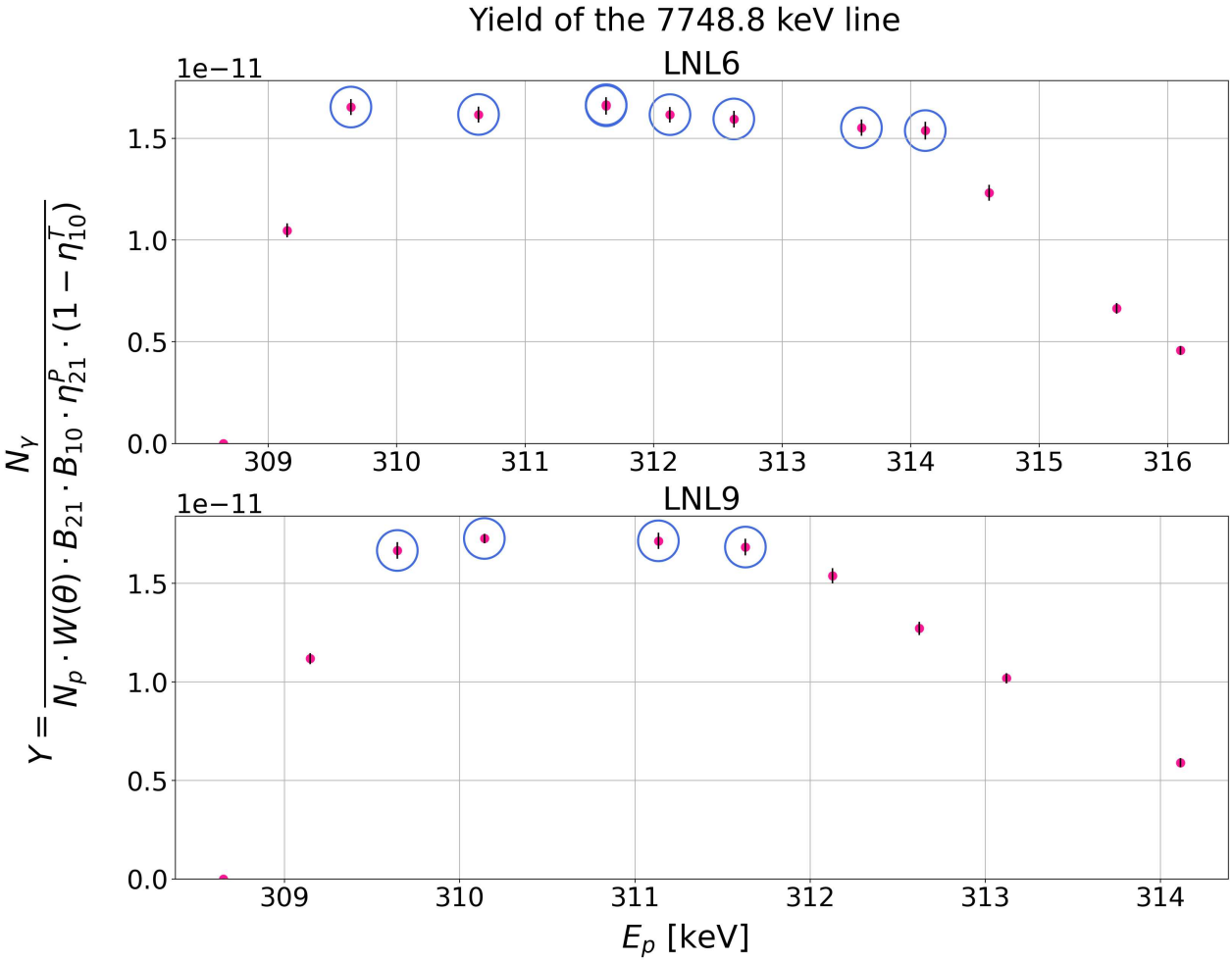

Figure 6.3: Yield profiles of LNL6 and LNL9 targets for the 7748.8 keV line (pink dots), their uncertainties are shown as vertical black lines. The blue-circled data points are those I used to estimate the effective stopping power $\mathcal{E}_{\text{eff}}$.

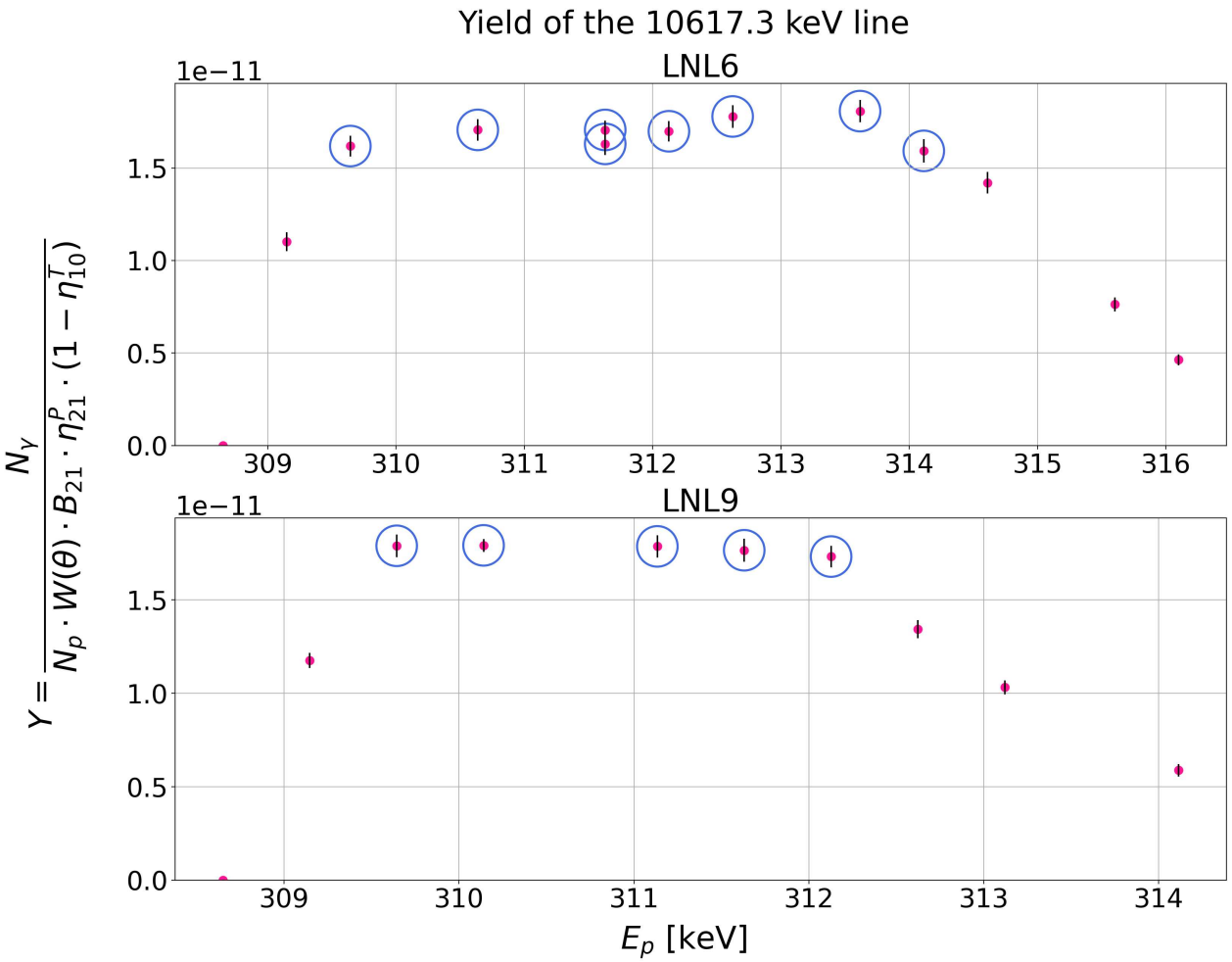

Figure 6.4: Yield profiles of LNL6 and LNL9 targets for the 10 617.3 keV line (pink dots), their uncertainties are shown as vertical black lines. The blue-circled data points are those I used to estimate the effective stopping power $\mathcal{E}_{\text{eff}}$.

6.2 The BGO campaigns

Throughout the BGO campaigns, seven targets have been investigated: four evaporated produced at Atomki (Hungary) and three sputtered manufactured at Legnaro. The sputtered targets had different thicknesses that those characterized during the HPGe campaign. Since they were analyzed with a BGO detector and its efficiency is not known up to date, I could not investigate their stoichiometry. For these targets characterization, I considered the four most prominent lines of the BGO spectra: 1368.6 keV, 4240.4 keV, 7748.8 keV and 10617.3 keV. The energy ranges used with these four lines are reported in Table A.3. The yield profiles as $Y = N_\gamma/Q$ for all targets, except LNL103, are shown in Fig. 6.5, 6.6, 6.7 and 6.8. In Tab. 6.4 is reported the target thickness obtained with the usual fit procedure.

The first couple of evaporated targets, ATOMKI1 and ATOMKI2, presented initially a fair plateau but, as more and more charge was deposited, the yield increased significantly right after the rising edge. Moreover, the tail profile became softer enough such that the yield profile resembled a triangle.

ATOMKI3 presents since the very first scan a smaller plateau in the energy region between 309 – 317 keV. A second scan was attempted after 10.27 C, but the feature became even more pronounced so we decided to dismount it.

ATOMKI4 shows a depression in the range 313 – 323 keV (in a similar fashion as LNL1 and LNL2) which disappeared after the first scan. For this reason, it was not possible to associate to it a target thickness.

LNL101 and LNL105 present good profiles. They are associated to two different sputtering times equal to 7’30” and 15’00” minutes which corresponds to two diverse thicknesses, see Fig. 6.5, 6.6, 6.7 and 6.8. The main difference between these targets is that LNL101 plateau height significantly lower after 26 C which represents a stoichiometry change in the target composition.

LNL103 was characterized two months later than LNL101 and LNL105. For this target, many scans were available, up to roughly 56 C of accumulated charge. This data availability allowed to investigate its degradation. For each line, the target thickness ΔE was obtained by fitting the scans with Eq. (5.10). In Fig. 6.9, 6.10, 6.11 and 6.12 it is shown the yields of the nine scans for our four lines, the fitting curve is also represented for each scan. The target thicknesses ΔE are listed in Tab. 6.5, overall I obtained that LNL103 degraded from 9.104 keV to 7.515 keV. These results are consistent for all the considered γ-rays. In Fig. 6.13 I plotted the deposited charge versus the average of target thickness and fitted the data points with a linear function which well described the data. The plateau height of LNL103 remains unchanged up to 20 C of deposited charge, then it decreases progressively.

Table 6.4: Target thickness ΔE (in keV) for the BGO analyzed lines. To retrieve these values, the Eq. (5.10) was used. Whenever a scans profile had peculiar characteristics that prevented estimating its ΔE, – is reported. ATOMKI4 do not have ΔE estimates.

Line	Target	Scan 1	Scan 2	Scan 3
1368.6 keV	ATOMKI1	50.0 ± 0.8	43.6 ± 0.5	–
	ATOMKI2	30.9 ± 1.3	–	–
	ATOMKI3	54.2 ± 0.8	–	
	LNL101	6.9 ± 0.3	6.4 ± 0.2	5.6 ± 0.1
	LNL105	16.8 ± 0.1	16.4 ± 0.1	15.7 ± 0.8
4240.0 keV	ATOMKI1	49.9 ± 0.8	43.7 ± 0.6	–
	ATOMKI2	30.7 ± 1.3	–	–
	ATOMKI3	54.4 ± 0.8	–	
	LNL101	6.9 ± 0.3	6.4 ± 0.2	5.5 ± 0.1
	LNL105	16.8 ± 0.1	16.4 ± 0.1	15.8 ± 0.7
7748.8 keV	ATOMKI1	49.9 ± 0.9	44.3 ± 0.5	–
	ATOMKI2	30.9 ± 1.4	–	–
	ATOMKI3	54.2 ± 0.8	–	
	LNL101	6.8 ± 0.3	6.4 ± 0.2	5.5 ± 0.1
	LNL105	16.8 ± 0.2	16.4 ± 0.1	15.7 ± 0.8
10 617.3 keV	ATOMKI1	50.0 ± 1.0	42.5 ± 0.6	–
	ATOMKI2	31.1 ± 1.1	–	–
	ATOMKI3	54.0 ± 1.0	–	
	LNL101	6.8 ± 0.2	6.4 ± 0.2	5.7 ± 0.1
	LNL105	16.8 ± 0.2	16.3 ± 0.2	15.8 ± 0.4

Table 6.5: Target thickness ΔE of LNL103 for the considered lines. Values obtained by fitting the yield profiles with Eq. (5.10), the error $\bar{\delta}$ associated to the average value has been calculated as the average absolute error $\sum \delta_i / N$ with $N = 4$.

Scan	ΔE [keV]				
	1368.6 keV	4240.0 keV	7748.8 keV	10 617.3 keV	Average
Scan 1	8.9 ± 0.1	8.9 ± 0.1	8.9 ± 0.1	9.1 ± 0.3	9.0 ± 0.2
Scan 2	8.8 ± 0.2	8.8 ± 0.2	8.8 ± 0.2	8.8 ± 0.2	8.8 ± 0.2
Scan 3	8.2 ± 0.2	8.2 ± 0.2	8.1 ± 0.2	8.1 ± 0.2	8.2 ± 0.2
Scan 4	8.5 ± 0.2	8.5 ± 0.2	8.5 ± 0.2	8.4 ± 0.3	8.5 ± 0.2
Scan 5	8.2 ± 0.2	8.2 ± 0.2	8.2 ± 0.2	8.2 ± 0.2	8.2 ± 0.2
Scan 6	7.9 ± 0.2	7.9 ± 0.2	7.9 ± 0.2	8.1 ± 0.2	7.9 ± 0.2
Scan 7	7.8 ± 0.2	7.8 ± 0.2	7.7 ± 0.2	7.9 ± 0.1	7.8 ± 0.2
Scan 8	7.7 ± 0.1	7.7 ± 0.2	7.8 ± 0.2	7.8 ± 0.4	7.7 ± 0.2
Scan 9	7.5 ± 0.3	7.5 ± 0.3	7.5 ± 0.3	7.6 ± 0.3	7.5 ± 0.3

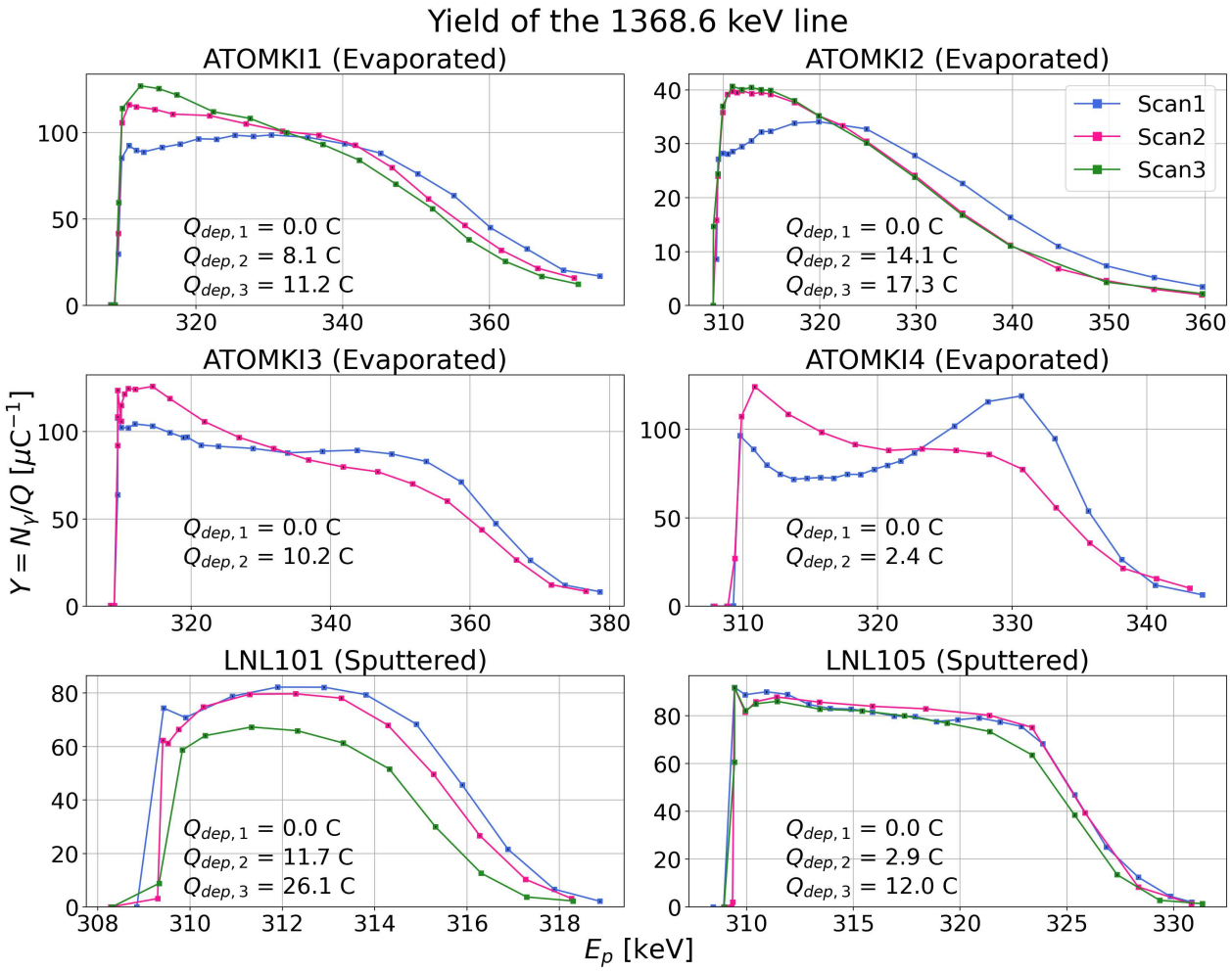

Figure 6.5: Yield profiles of six targets analyzed in the BGO campaign for the 1368.6 keV line, uncertainties are represented as vertical black lines. The deposited charge is reported in each plot.

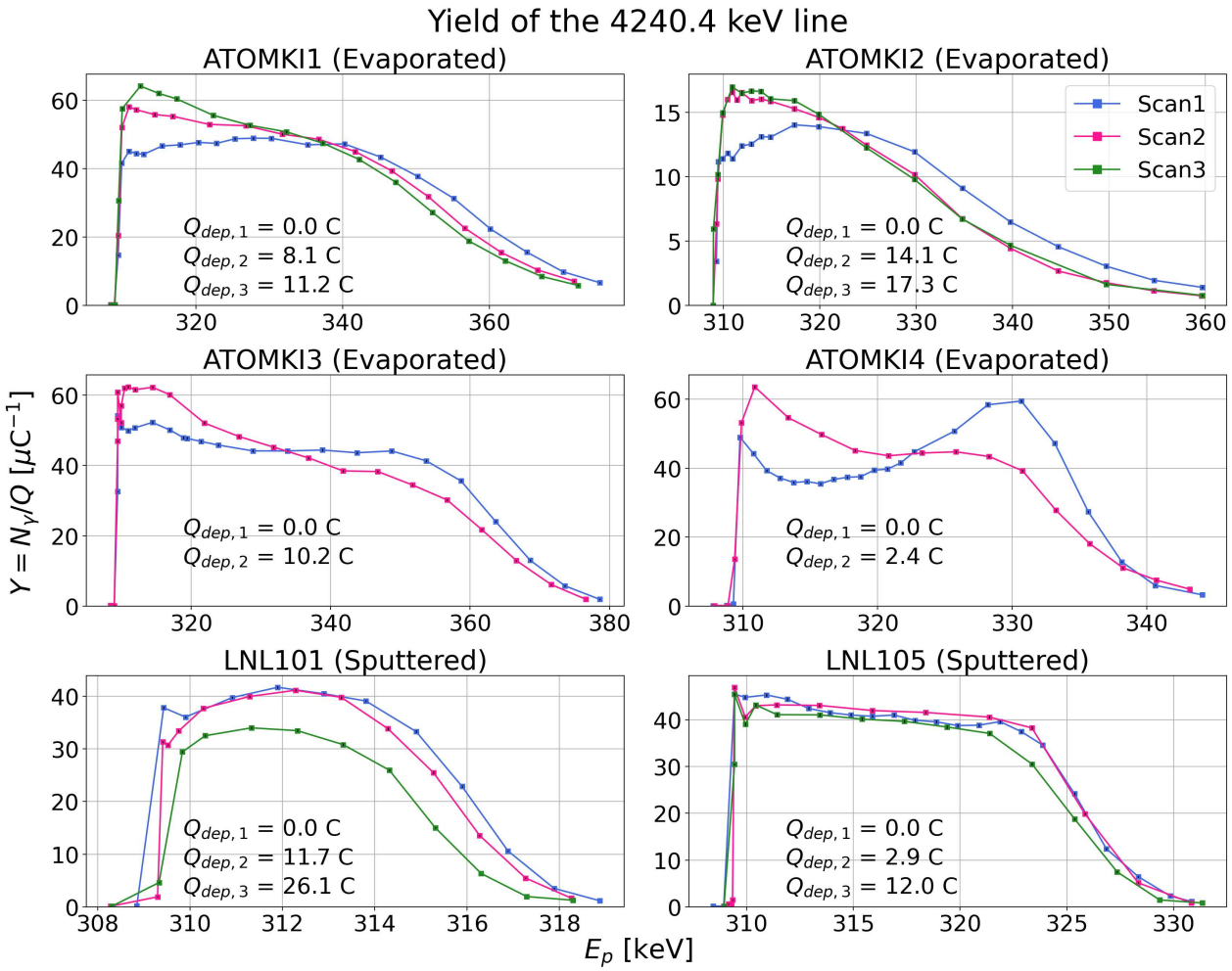

Figure 6.6: Yield profiles of six targets analyzed in the BGO campaign for the 1368.6 keV line, uncertainties are represented as vertical black lines. The deposited charge is reported in each plot.

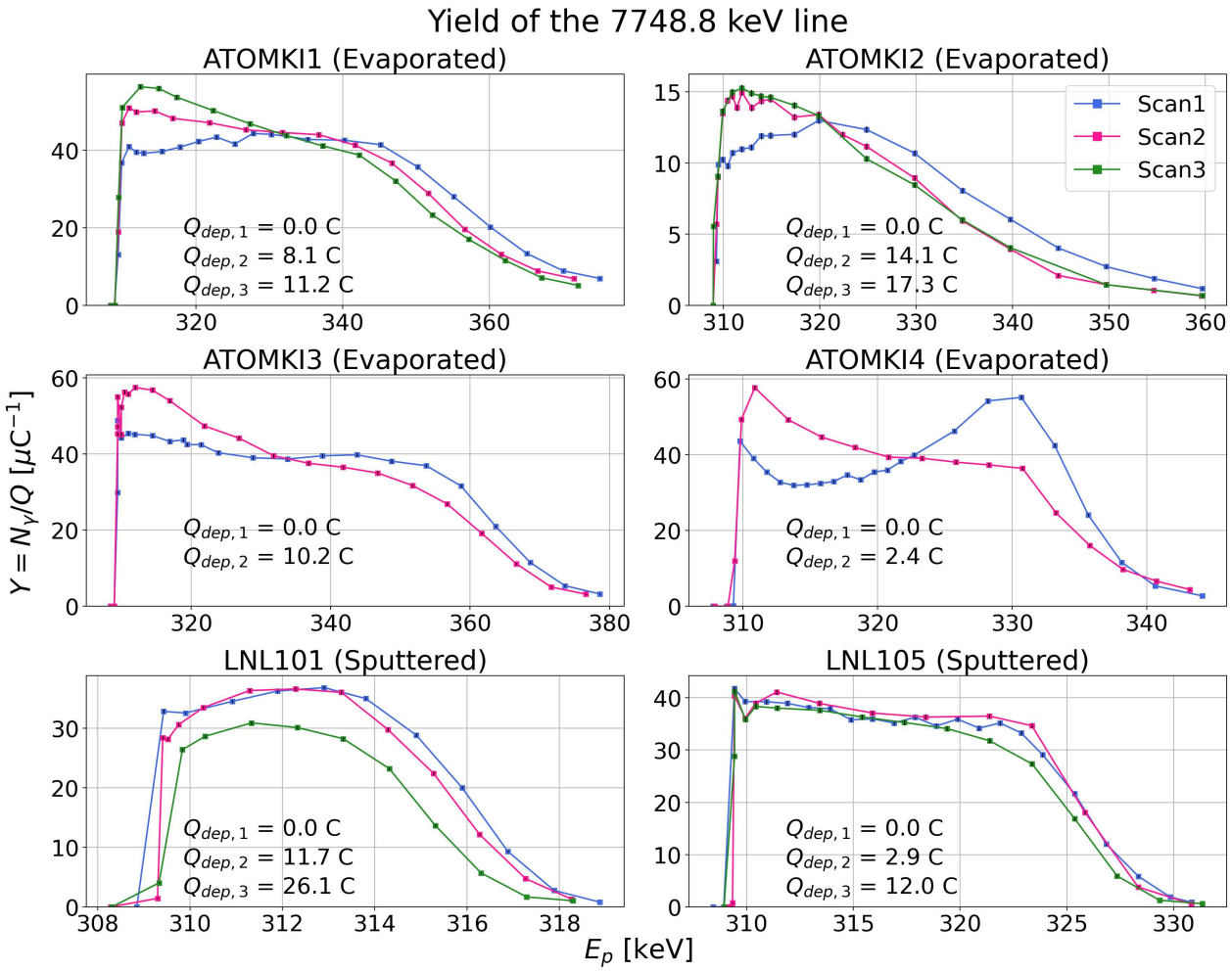

Figure 6.7: Yield profiles of six targets analyzed in the BGO campaign for the 7748.8 keV line, uncertainties are represented as vertical black lines. The deposited charge is reported in each plot.

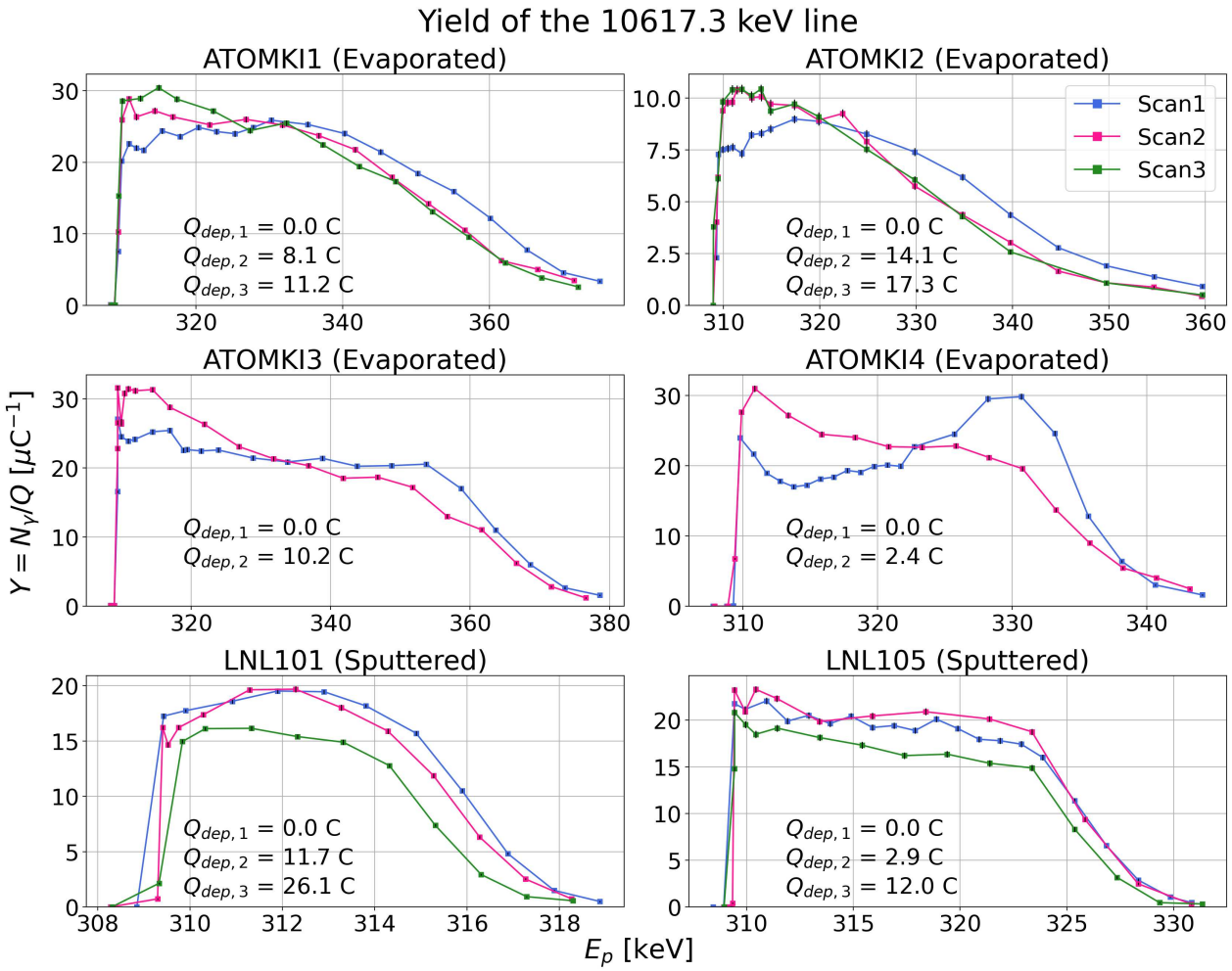

Figure 6.8: Yield profiles of six targets analyzed in the BGO campaign for the 10 617.3 keV line, uncertainties are represented as vertical black lines. The deposited charge is reported in each plot.

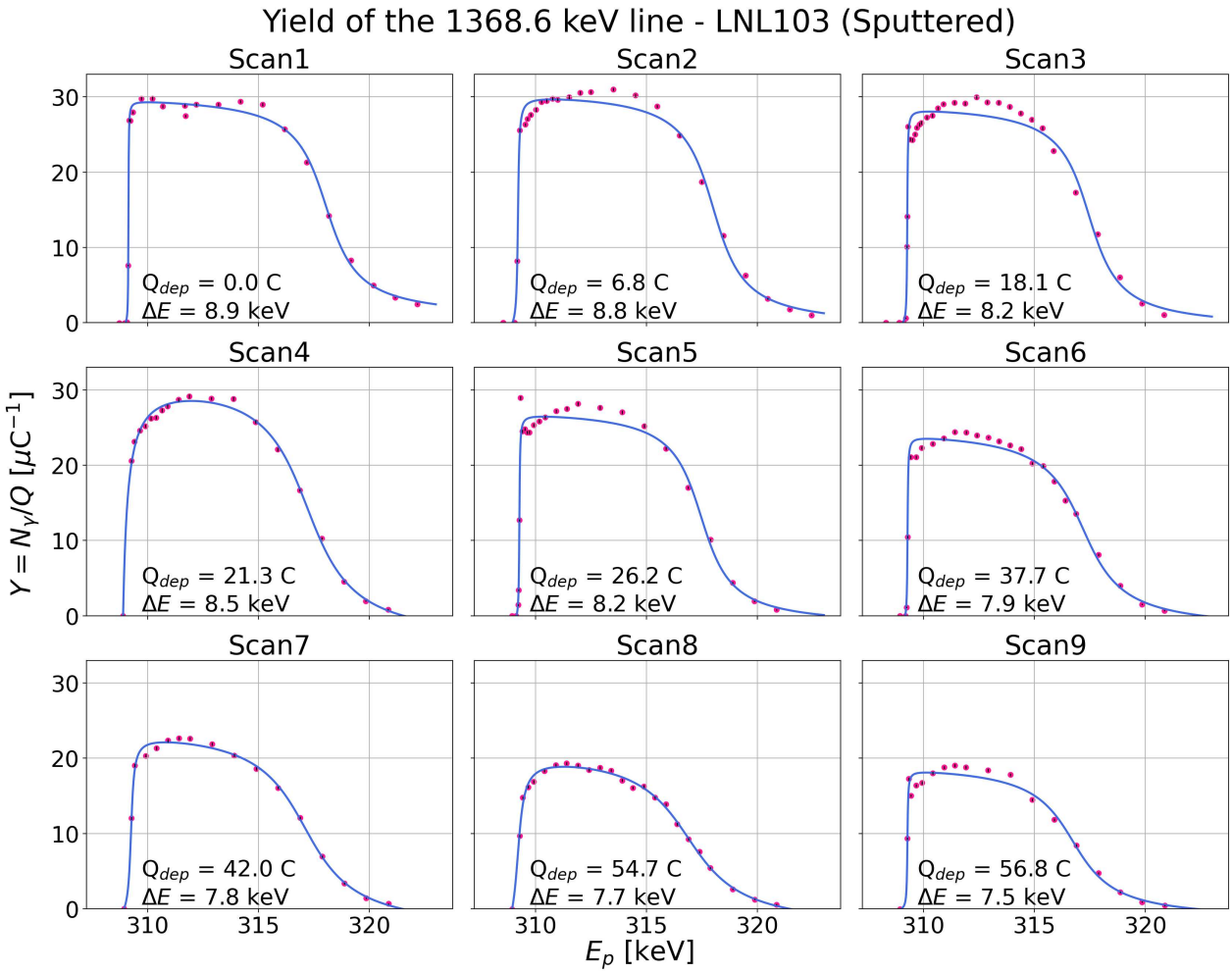

Figure 6.9: Yields profile of the 1368.6 keV line for LNL103 target over the numerous scans performed. The pink dots represents the yield while their uncertainties are reported as vertical black lines. The blue dotted lines represent the fit with Eq. (5.10).

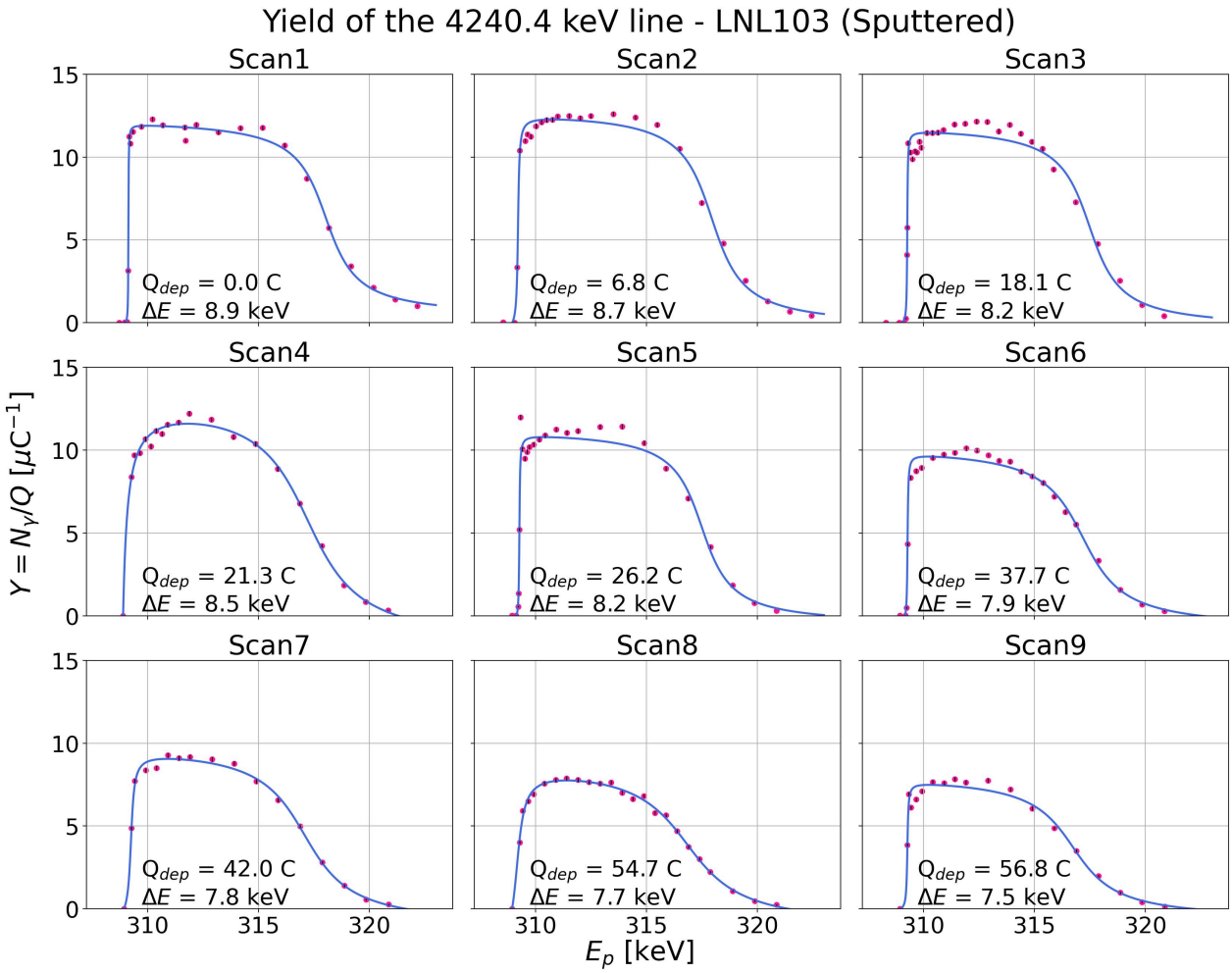

Figure 6.10: Yields profile of the 4240.0 keV line for LNL103 target over the numerous scans performed. The pink dots represents the yield while their uncertainties are reported as vertical black lines. The blue dotted lines represent the fit with Eq. (5.10).

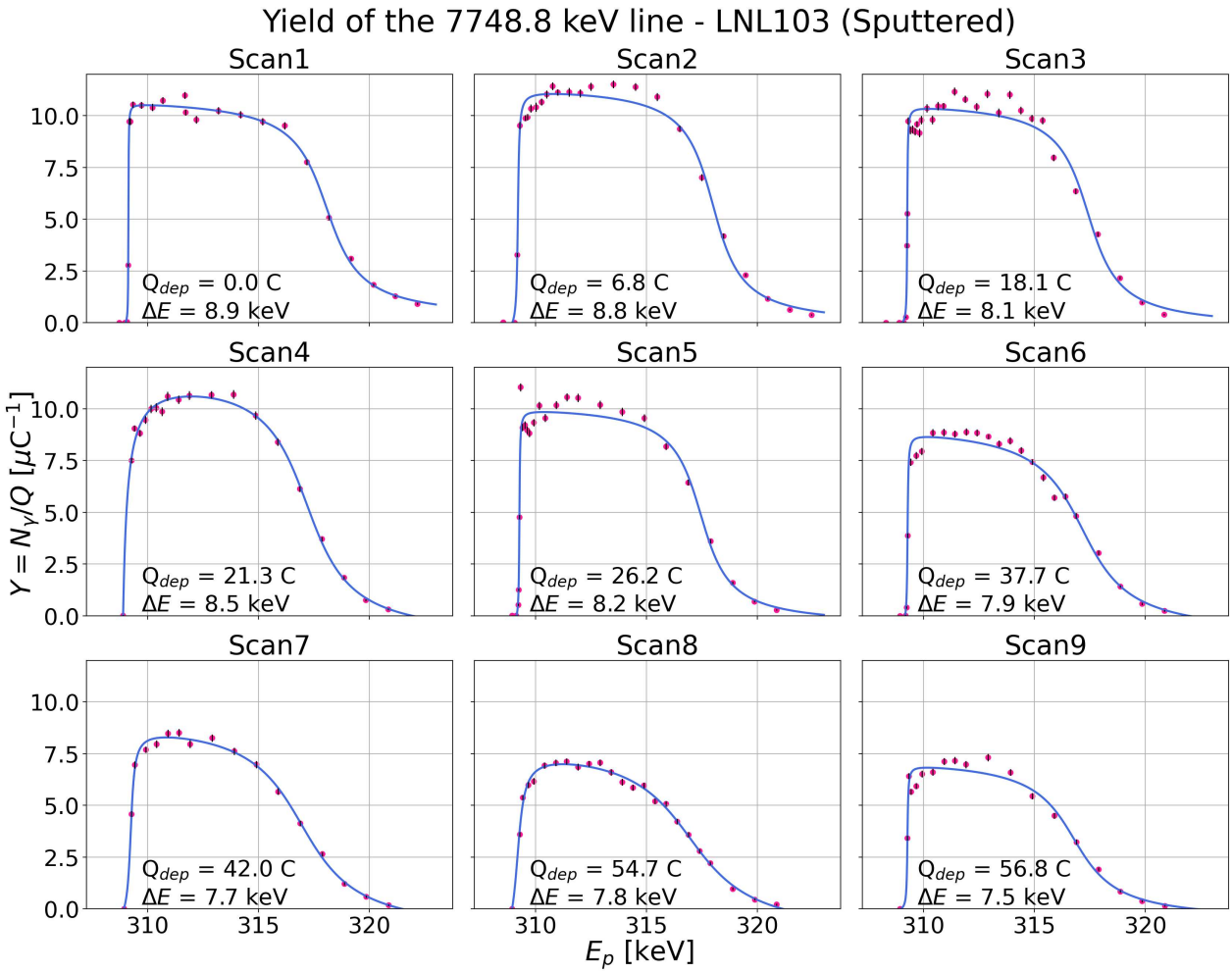

Figure 6.11: Yields profile of the 7748.8 keV line for LNL103 target over the numerous scans performed. The pink dots represents the yield while their uncertainties are reported as vertical black lines. The blue dotted lines represent the fit with Eq. (5.10).

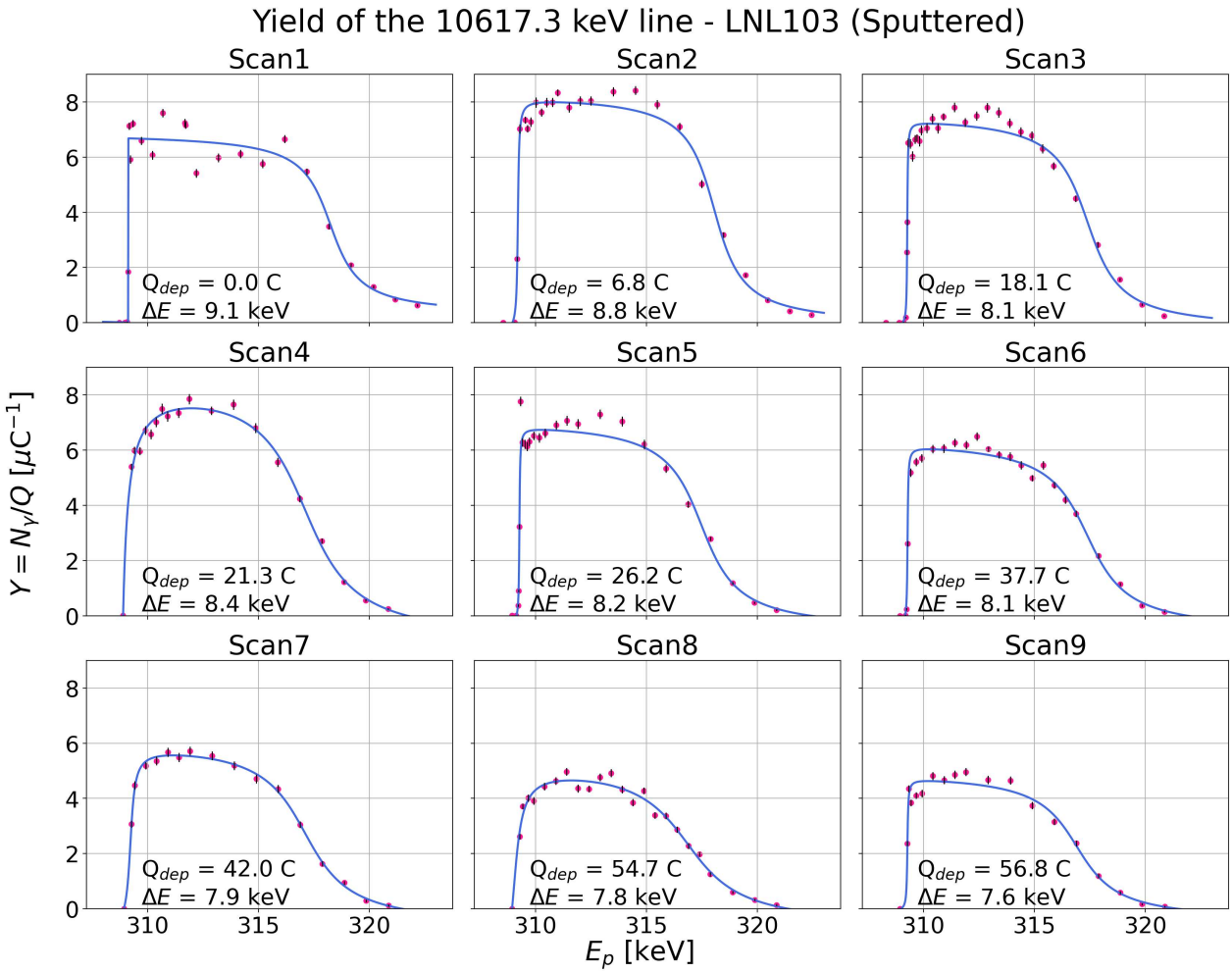

Figure 6.12: Yields profile of the 10617.3 keV line for LNL103 target over the numerous scans performed. The pink dots represents the yield while their uncertainties are reported as vertical black lines. The blue dotted lines represent the fit with Eq. (5.10).

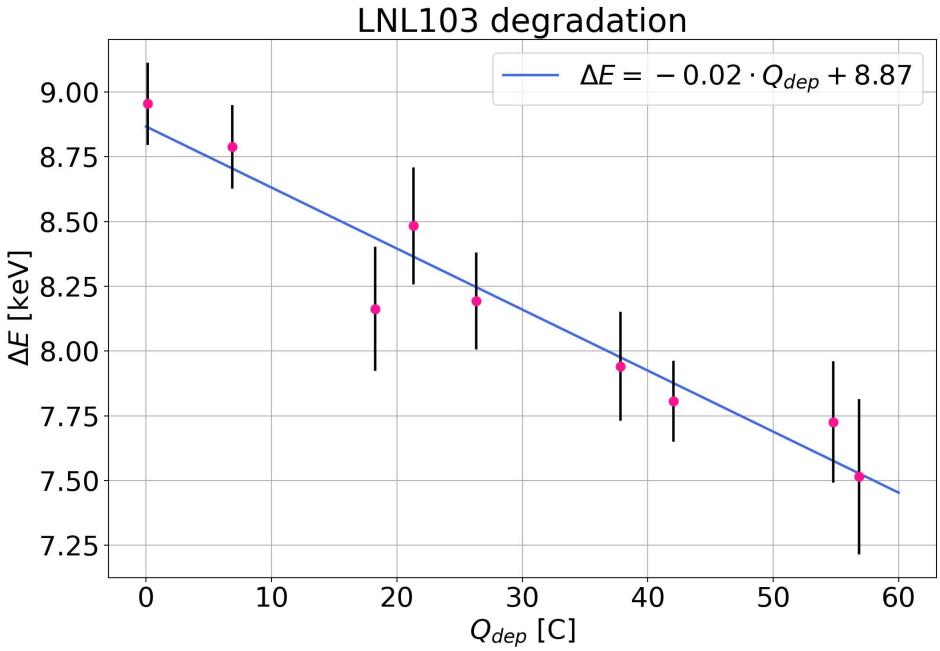

Figure 6.13: Target thickness ΔE versus deposited charge Q_{dep} of LNL103 target. The uncertainties are reported as vertical black lines, the blue line is a linear fit.

6.2.1 Contaminants analysis

During the BGO campaigns, we performed several runs to investigate the presence of contaminants. Two candidates had been considered, ^{11}B and ^{19}F, because they have been commonly observed on solid targets and generates α particle that ultimately would affect the study of $^{23}\text{Na}(p,\alpha)^{20}\text{Ne}$. These two nuclei may interact with the beam protons respectively via the $^{11}\text{B}(p,\gamma)^{12}\text{C}$ and $^{19}\text{F}(p,\alpha\gamma)^{16}\text{O}$ reactions. Their associated Q-values are respectively 15 956.7 keV [51] and 12 843.5 keV [52], but the ^{19}F reaction proceed by steps creating ^{20}Ne that decays emitting an α particle and ^{16}O which de-excite emitting a γ. By populating the two excited levels $E_x = 16\,106.0$ keV of ^{12}C and $E_x = 6129.9$ keV of ^{16}O, it is possible to selected a couple of γ emissions to investigate the contamination of ^{11}B and ^{19}F. I chose the emission at 11 660.1 keV for the ^{11}B and at 6128.6 keV for the ^{19}F. The energetic ranges used for these lines are reported in Table A.3. The retrieved yields $Y = N_\gamma/Q$ for the runs available for the contaminants analysis are plotted in Fig. 6.14 and 6.15. I did not take into consideration ATOMKI2 and LNL103 since they only account for one data point in both plot. The ^{11}B contamination seems to be significantly lower in the sputtered targets. For the ^{19}F we have the opposite situation, with the evaporated targets having the lowest amount of ^{19}F.

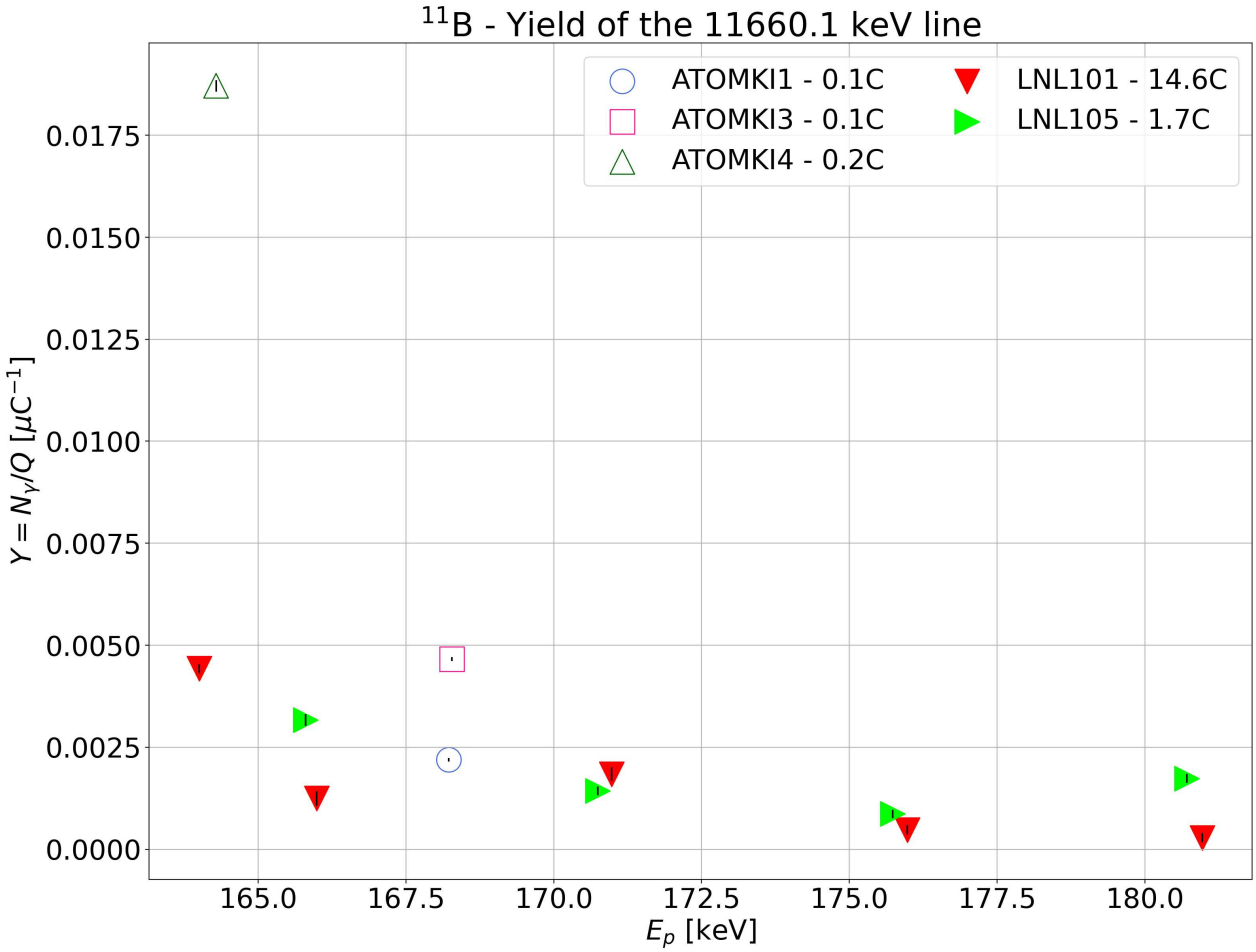

Figure 6.14: Yield representation of the 11 660.1 keV line referring to ^{11}B nucleus. Empty points refer to evaporated targets, solid ones to sputtered targets. Uncertainties are reported as vertical black lines.

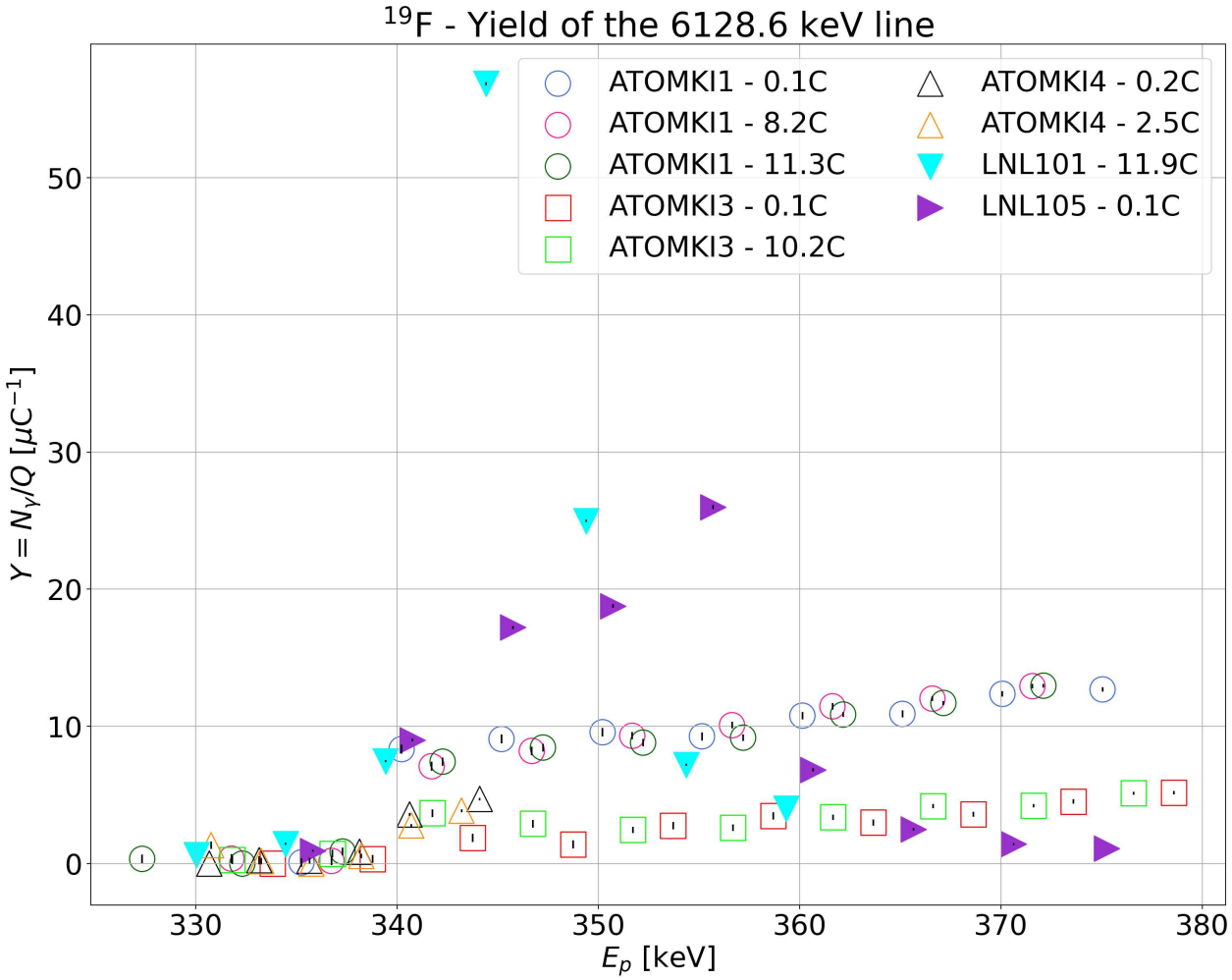

Figure 6.15: Yield representation of the 6128.6 keV line referring to ^{19}F nucleus. Empty points refer to evaporated targets, solid ones to sputtered targets. Uncertainties are reported as vertical black lines.

7 Conclusions

I used the NRRA technique, exploiting the $E_r^{lab} = 309\,keV$ resonance of the $^{23}Na(p,\gamma)^{24}Mg$ reaction, to characterize 12 targets produced following two different techniques: vacuum evaporation (7 targets) and magnetron sputtering (5 targets). These targets have been characterized using the proton beam delivered by LUNA 400kV accelerator in two campaigns using two different detectors (an HPGe and a BGO). The efficiency of HPGe was known, so it was possible to investigate the effective stopping power of the sputtered targets. Thanks to the BGO efficiency, it was possible to considered a larger number of targets, characterize them faster and investigate the presence of two contaminants. In particular, the LNL103 target degradation was analyzed up to high accumulated charge. For both campaigns, the target thickness was calculated when possible.

The greatest differences between the evaporated Na_2WO_4 and sputtered $NaNbO_3$ targets are that the former are associated to a much larger target thickness ΔE (ranging between $30-54\,keV$ at the first scan) and they tend to vary quite substantially accumulating charge. The greater ΔE can be explained by the production method since it is associated to higher deposition rates than magnetron sputtering and because, in order to produce a more uniform layer, probably more material has been deposited. The dramatic variation in the yield profile, in particular the plateau shape and position, is linked to strong variations in the target stoichiometry. For these reasons, the evaporated targets resulted to be less stable than the sputtered ones.

The sputtered targets are associated to much thinner ΔE ($4-17\,keV$ at the first scan) and proved to be more stable on multiple scans. Moreover, for all of them it was possible to retrieve (even by eye) the plateau. Again, this finds an explanation in the production method. In the magnetron sputtering technique, many of the variables that affect the produced target are directly controlled by the operator. LNL103 demonstrates their stability, after almost 60 C the yield profile is still evident and never presented anomalies. An even stronger proof that the production technique deeply influences the final result, is that the evaporated targets were produced by two independent manufacturers but their overall issues, analyzed with different detectors too, were the same (i.e. the LNL1 and ATOMKI4 yield profiles resemble the same structures).

For the LNL6 and LNL9 targets (sputtered, HPGe), I computed the effective stopping power $\mathcal{E}_{eff}$ using the 7748.8 keV and 10617.3 keV γ-rays, under the approximation of infinitely thick targets. The result is significantly different than the nominal value for $NaNbO_3$ targets, since the $\mathcal{E}_{eff}^{LAB}$ varies from $86-95\,eV/10^{15}atoms/cm^2$ with a 18% uncertainty while $\mathcal{E}_{eff}^{NOM}$ is set at $63\,eV/10^{15}atoms/cm^2$ with 3% error. These differences suggest that the actual chemical composition diverges from the theoretical one ($NaNBO_3$). This is believed to be due to O, present in the atmosphere of the sputtering chamber, which were deposited on the Ta substrate together with $NaNbO_3$ compound. Under the assumption of variation only in the O amount, in order to conciliate the laboratory and nominal $\mathcal{E}_{eff}$ values, an

increase of about 70 – 100% of O is required.

Focusing to LNL103 target (sputtered, BGO), we see that its degradation in thickness can be assumed as linear in good approximation. Despite not having the BGO efficiency, we can state that, since the plateau height varies little up to about 20 C of deposited charge, the target stoichiometry is almost unchanged below this value. Beyond 20 C, the plateau progressively lowers with each scan. These considerations remain valid for all the four considered lines. Finally, observing the fit with Eq. (5.10), we see that along the plateau of some scans (i.e. 2,3,5 and 6) there is a small deviation from the fit. This is supposed to be the effect of a non-uniform Na consumption throughout the target which results in a smoother transition between the rising edge and the plateau region.

For the BGO campaigns we investigated the presence of two contaminants, ^{11}B and ^{19}F. The results are opposite between the target types, the sputtered ones are associated to lower ^{11}B and higher ^{19}F contamination than the evaporated.

Considering these characteristics, the sputtered $NaNbO_3$ targets are those chosen to be used in the cross-section measurements of the ^{23}Na$(p,\alpha)^{20}$Ne reaction. They provides a more stable and consistent profile, even at large deposited charge, and they never developed problematic structures. Despite this, it is better to avoid depositing more than 20 C on it in order to preserve the target stoichiometry. Further studies to define the exact chemical composition of sputtered targets are highly advised as well as the usage of a different source to limit the fluorine contamination.

Appendix

A.1: Calibration fit parameters. The HPGe runs were grouped together while for those referring to BGO I separated them according to the scan.

Detector	Target	Run	m	q [keV]	a
HPGe	LNL1	35	0.9973 ± 0.0001	-1.6661 ± 0.7837	–
	LNL4	64	0.9978 ± 0.0001	-1.0416 ± 0.5309	–
	LNL6	96	0.9979 ± 0.0001	-1.4974 ± 0.6424	–
	LNL2	136	0.9979 ± 0.0001	-1.4974 ± 0.6424	–
	LNL9	167	0.9979 ± 0.0001	-0.9089 ± 0.4424	–
BGO	LNL101	211	3.3304 ± 0.0072	-114.4284 ± 11.3333	0.00023 ± 0.00003
	LNL101	211	4.4877 ± 0.018	-35.1414 ± 20.7666	0.0002 ± 0.0001
	LNL101	211	2.8958 ± 0.0181	-25.2041 ± 32.3629	0.00021 ± 0.00007
	LNL101	211	3.6614 ± 0.018	-28.9782 ± 25.5371	0.00021 ± 0.00009
	LNL101	211	3.497 ± 0.0189	-23.5397 ± 27.9334	0.00014 ± 0.00008
	LNL101	211	4.7135 ± 0.0262	-37.7731 ± 28.9195	0.00027 ± 0.00016
BGO	LNL101	226	3.5565 ± 0.0011	-107.9873 ± 1.6866	0.0002 ± 0.00001
	LNL101	226	4.7803 ± 0.021	-31.3164 ± 22.8207	0.00023 ± 0.00013
	LNL101	226	2.9746 ± 0.032	-30.0697 ± 55.8351	0.00022 ± 0.00013
	LNL101	226	3.7081 ± 0.0158	-19.374 ± 22.0202	0.00018 ± 0.00008
	LNL101	226	3.618 ± 0.0213	-21.6512 ± 30.4351	0.00014 ± 0.0001
	LNL101	226	4.8165 ± 0.0234	-23.5167 ± 25.2193	0.00026 ± 0.00014
BGO	LNL101	252	3.5626 ± 0.0042	-112.2864 ± 6.2533	0.00018 ± 0.00002
	LNL101	252	4.7695 ± 0.0195	-32.3232 ± 21.209	0.00023 ± 0.00012
	LNL101	252	2.9691 ± 0.0338	-31.7256 ± 59.082	0.00024 ± 0.00014
	LNL101	252	3.7082 ± 0.0183	-17.0467 ± 25.4744	0.0002 ± 0.00009
	LNL101	252	3.5995 ± 0.0186	-16.7891 ± 26.7232	0.00014 ± 0.00008
	LNL101	252	4.802 ± 0.0241	-29.2864 ± 26.0643	0.00029 ± 0.00015
BGO	ATOMKI4	264	3.5434 ± 0.0144	-92.3463 ± 21.2687	0.00021 ± 0.00007
	ATOMKI4	264	4.759 ± 0.0221	-35.1003 ± 24.0671	0.00022 ± 0.00013
	ATOMKI4	264	2.9607 ± 0.0293	-30.8495 ± 51.4218	0.00021 ± 0.00012
	ATOMKI4	264	3.6996 ± 0.0187	-21.5067 ± 26.1242	0.00021 ± 0.00009
	ATOMKI4	264	3.5933 ± 0.0154	-19.8294 ± 22.1584	0.00015 ± 0.00007
	ATOMKI4	264	4.8022 ± 0.0283	-35.8706 ± 30.5915	0.00025 ± 0.00017
BGO	ATOMKI4	291	3.545 ± 0.0086	-114.5813 ± 12.7803	0.00018 ± 0.00004
	ATOMKI4	291	4.7448 ± 0.0227	-36.0224 ± 24.8862	0.0003 ± 0.00014
	ATOMKI4	291	2.9524 ± 0.0281	-32.1165 ± 49.3526	0.00024 ± 0.00012
	ATOMKI4	291	3.6911 ± 0.0191	-22.255 ± 26.7554	0.00024 ± 0.00009

Detector	Target	Run	m	q [keV]	a
	ATOMKI4	291	3.5812 ± 0.016	-19.1345 ± 23.0826	0.00015 ± 0.00007
	ATOMKI4	291	4.7878 ± 0.029	-32.0091 ± 31.3746	0.00029 ± 0.00018
BGO	ATOMKI1	309	3.5274 ± 0.0084	-93.0241 ± 12.5014	0.00024 ± 0.00004
	ATOMKI1	309	4.7414 ± 0.0249	-31.2067 ± 27.2882	0.00031 ± 0.00015
	ATOMKI1	309	2.954 ± 0.0335	-33.5108 ± 58.9335	0.0002 ± 0.00014
	ATOMKI1	309	3.691 ± 0.0166	-17.1908 ± 23.2859	0.00022 ± 0.00008
	ATOMKI1	309	3.5852 ± 0.0158	-20.5607 ± 22.7798	0.00013 ± 0.00007
	ATOMKI1	309	4.795 ± 0.0286	-33.9369 ± 30.9838	0.00024 ± 0.00017
BGO	ATOMKI1	332	3.5293 ± 0.0072	-96.6303 ± 10.6796	0.00021 ± 0.00003
	ATOMKI1	332	4.7306 ± 0.0194	-35.1759 ± 21.2621	0.00026 ± 0.00012
	ATOMKI1	332	2.9402 ± 0.0293	-30.2651 ± 51.7449	0.00021 ± 0.00012
	ATOMKI1	332	3.6846 ± 0.0157	-21.6781 ± 22.0567	0.00023 ± 0.00008
	ATOMKI1	332	3.5652 ± 0.0167	-17.0264 ± 24.3	0.00014 ± 0.00008
	ATOMKI1	332	4.7699 ± 0.0277	-31.1014 ± 30.1338	0.00024 ± 0.00017
BGO	ATOMKI1	352	3.5424 ± 0.0037	-134.7669 ± 5.5655	0.00018 ± 0.00002
	ATOMKI1	352	4.727 ± 0.0175	-42.7949 ± 19.278	0.00026 ± 0.00011
	ATOMKI1	352	2.9373 ± 0.0248	-34.6798 ± 43.7541	0.00023 ± 0.0001
	ATOMKI1	352	3.6847 ± 0.0181	-30.4197 ± 25.5373	0.00022 ± 0.00009
	ATOMKI1	352	3.5673 ± 0.0178	-29.1002 ± 25.8651	0.00017 ± 0.00008
	ATOMKI1	352	4.777 ± 0.0274	-42.5746 ± 29.7896	0.00021 ± 0.00016
BGO	ATOMKI3	370	3.5383 ± 0.0058	-131.8788 ± 8.5873	0.00014 ± 0.00003
	ATOMKI3	370	4.731 ± 0.0275	-48.1573 ± 30.1896	0.00027 ± 0.00017
	ATOMKI3	370	2.9456 ± 0.0276	-40.3972 ± 48.6145	0.00022 ± 0.00011
	ATOMKI3	370	3.689 ± 0.0204	-33.271 ± 28.6886	0.00023 ± 0.0001
	ATOMKI3	370	3.5714 ± 0.0199	-31.8587 ± 28.9157	0.00015 ± 0.00009
	ATOMKI3	370	4.7807 ± 0.0293	-39.6483 ± 31.8146	0.00027 ± 0.00018
BGO	ATOMKI3	396	3.5482 ± 0.0052	-136.392 ± 7.7711	0.00016 ± 0.00002
	ATOMKI3	396	4.7306 ± 0.0194	-35.1759 ± 21.2621	0.00028 ± 0.00012
	ATOMKI3	396	2.9442 ± 0.0268	-30.4309 ± 47.2708	0.0002 ± 0.00011
	ATOMKI3	396	3.6975 ± 0.0175	-23.7797 ± 24.563	0.00019 ± 0.00008
	ATOMKI3	396	3.5733 ± 0.0187	-24.767 ± 27.0603	0.00018 ± 0.00009
	ATOMKI3	396	4.7878 ± 0.029	-36.7969 ± 31.3996	0.00024 ± 0.00018
BGO	LNL105	421	3.5195 ± 0.0066	-88.7368 ± 9.8031	0.00019 ± 0.00003
	LNL105	421	4.72 ± 0.0179	-26.7227 ± 19.6385	0.00024 ± 0.00011
	LNL105	421	2.9429 ± 0.0292	-31.4483 ± 51.5279	0.00021 ± 0.00012
	LNL105	421	3.6909 ± 0.0141	-15.8139 ± 19.8347	0.0002 ± 0.00007
	LNL105	421	3.5753 ± 0.0174	-17.6664 ± 25.2073	0.00013 ± 0.00008

Detector	Target	Run	m	q [keV]	a
	LNL105	421	4.7807 ± 0.0293	-30.0869 ± 31.764	0.00022 ± 0.00018
BGO	LNL105	455	3.4992 ± 0.0265	-46.2587 ± 39.3843	0.00028 ± 0.00013
	LNL105	455	4.7238 ± 0.0237	-35.0329 ± 26.0959	0.00023 ± 0.00014
	LNL105	455	2.943 ± 0.0324	-33.585 ± 57.06	0.0002 ± 0.00013
	LNL105	455	3.6932 ± 0.0177	-22.305 ± 24.8729	0.0002 ± 0.00008
	LNL105	455	3.5691 ± 0.0142	-20.6824 ± 20.6744	0.00013 ± 0.00006
	LNL105	455	4.7734 ± 0.0255	-31.1749 ± 27.6997	0.00032 ± 0.00016
BGO	LNL105	472	3.5368 ± 0.0023	-135.8405 ± 3.365	0.00018 ± 0.00001
	LNL105	472	4.7202 ± 0.0219	-42.6444 ± 24.1171	0.00001 ± 0.00012
	LNL105	472	2.9388 ± 0.027	-39.8232 ± 47.8075	0.00019 ± 0.00011
	LNL105	472	3.6869 ± 0.0193	-31.8449 ± 27.1116	0.00023 ± 0.00009
	LNL105	472	3.5634 ± 0.0203	-32.5574 ± 29.5202	0.00014 ± 0.00009
	LNL105	472	4.7628 ± 0.028	-38.7135 ± 30.5724	0.00024 ± 0.00017
BGO	LNL103	722	1.2476 ± 0.0154	-54.4161 ± 64.2079	0.00017 ± 0.00004
	LNL103	722	1.2665 ± 0.0126	-40.5614 ± 51.5668	0.00009 ± 0.00003
	LNL103	722	1.4092 ± 0.0095	-18.8727 ± 34.8041	0.00005 ± 0.00002
	LNL103	722	1.3417 ± 0.0094	-28.6684 ± 36.1708	0.00006 ± 0.00002
	LNL103	722	1.317 ± 0.0084	-23.0729 ± 32.9369	0.00004 ± 0.00002
	LNL103	722	1.2239 ± 0.0149	-53.3 ± 63.4817	0.0002 ± 0.00004
BGO	LNL103	723	1.201 ± 0.0137	-54.5275 ± 59.4195	0.00015 ± 0.00003
	LNL103	723	1.2133 ± 0.0122	-41.9242 ± 52.2848	0.00009 ± 0.00002
	LNL103	723	1.3495 ± 0.0128	-25.4751 ± 49.173	0.00006 ± 0.00003
	LNL103	723	1.2845 ± 0.0096	-31.1044 ± 38.9416	0.00006 ± 0.00002
	LNL103	723	1.2614 ± 0.0102	-23.7335 ± 41.7794	0.00005 ± 0.00002
	LNL103	723	1.1741 ± 0.0149	-57.2928 ± 65.9378	0.00023 ± 0.00004
BGO	LNL103	746	1.2024 ± 0.015	-56.9727 ± 64.8268	0.00015 ± 0.00004
	LNL103	746	1.2168 ± 0.0119	-42.9717 ± 51.0185	0.00009 ± 0.00002
	LNL103	746	1.3525 ± 0.0105	-23.8842 ± 40.359	0.00006 ± 0.00002
	LNL103	746	1.2861 ± 0.0105	-30.2142 ± 42.234	0.00006 ± 0.00002
	LNL103	746	1.2649 ± 0.0092	-23.3484 ± 37.5187	0.00005 ± 0.00002
	LNL103	746	1.1767 ± 0.0143	-54.6393 ± 63.1796	0.00023 ± 0.00004
BGO	LNL103	779	1.2049 ± 0.0142	-52.584 ± 61.4616	0.00015 ± 0.00004
	LNL103	779	1.2214 ± 0.012	-43.4899 ± 51.2208	0.00009 ± 0.00002
	LNL103	779	1.352 ± 0.0106	-15.2318 ± 40.4096	0.00006 ± 0.00002
	LNL103	779	1.2894 ± 0.0105	-32.5289 ± 42.1819	0.00005 ± 0.00002
	LNL103	779	1.2671 ± 0.0089	-24.1259 ± 36.4662	0.00005 ± 0.00002

Detector	Target	Run	m	q [keV]	a
	LNL103	779	1.1811 ± 0.0149	-60.7575 ± 65.7036	0.00022 ± 0.00004
BGO	LNL103	808	1.2042 ± 0.0128	-49.448 ± 55.343	0.00016 ± 0.00003
	LNL103	808	1.224 ± 0.011	-42.2133 ± 46.6694	0.00009 ± 0.00002
	LNL103	808	1.3562 ± 0.0086	-19.2342 ± 32.6481	0.00006 ± 0.00002
	LNL103	808	1.291 ± 0.0095	-28.7918 ± 38.2207	0.00006 ± 0.00002
	LNL103	808	1.2699 ± 0.0089	-23.3422 ± 36.4834	0.00005 ± 0.00002
	LNL103	808	1.1881 ± 0.0152	-63.5026 ± 66.5768	0.0002 ± 0.00004
BGO	LNL103	835	1.2031 ± 0.0138	-54.5576 ± 59.5783	0.00014 ± 0.00003
	LNL103	835	1.2212 ± 0.0114	-39.6868 ± 48.3731	0.00009 ± 0.00002
	LNL103	835	1.3517 ± 0.0117	-24.8077 ± 44.9534	0.00006 ± 0.00002
	LNL103	835	1.286 ± 0.0096	-28.7972 ± 38.6134	0.00007 ± 0.00002
	LNL103	835	1.2654 ± 0.0088	-19.5917 ± 36.2098	0.00005 ± 0.00002
	LNL103	835	1.1792 ± 0.0171	-51.5482 ± 75.4109	0.00022 ± 0.00005
BGO	LNL103	869	1.2047 ± 0.0144	-53.7596 ± 62.0847	0.00015 ± 0.00004
	LNL103	869	1.2214 ± 0.0104	-39.5927 ± 44.3164	0.00009 ± 0.00002
	LNL103	869	1.3523 ± 0.011	-21.6536 ± 42.2945	0.00006 ± 0.00002
	LNL103	869	1.2889 ± 0.0102	-30.2482 ± 41.0627	0.00006 ± 0.00002
	LNL103	869	1.2666 ± 0.0084	-20.1521 ± 34.1786	0.00005 ± 0.00001
	LNL103	869	1.182 ± 0.0151	-57.4285 ± 66.6059	0.00022 ± 0.00004
BGO	LNL103	888	1.2058 ± 0.0142	-55.9827 ± 61.3165	0.00016 ± 0.00004
	LNL103	888	1.2245 ± 0.0118	-44.0507 ± 50.0337	0.00009 ± 0.00002
	LNL103	888	1.3535 ± 0.0117	-23.7256 ± 44.6236	0.00006 ± 0.00002
	LNL103	888	1.2908 ± 0.0109	-34.5376 ± 43.7508	0.00005 ± 0.00002
	LNL103	888	1.2707 ± 0.0093	-27.3468 ± 38.1349	0.00004 ± 0.00002
	LNL103	888	1.1804 ± 0.0145	-53.4887 ± 64.0896	0.00021 ± 0.00004
BGO	LNL103	916	1.2086 ± 0.0165	-59.2442 ± 71.0432	0.00014 ± 0.00004
	LNL103	916	1.2262 ± 0.0135	-43.786 ± 57.1756	0.00008 ± 0.00003
	LNL103	916	1.3552 ± 0.0126	-21.4161 ± 48.0845	0.00007 ± 0.00003
	LNL103	916	1.2921 ± 0.0122	-32.797 ± 48.9261	0.00006 ± 0.00002
	LNL103	916	1.2673 ± 0.0079	-13.8706 ± 32.2116	0.00004 ± 0.00001
	LNL103	916	1.1815 ± 0.0131	-51.1703 ± 57.7416	0.00021 ± 0.00004
BGO	LNL103	935	1.206 ± 0.0122	-49.3346 ± 52.7082	0.00015 ± 0.00003
	LNL103	935	1.2241 ± 0.0134	-41.3256 ± 56.9949	0.00009 ± 0.00003
	LNL103	935	1.3557 ± 0.0112	-24.0416 ± 42.9281	0.00006 ± 0.00002
	LNL103	935	1.2931 ± 0.0109	-33.2412 ± 43.883	0.00005 ± 0.00002
	LNL103	935	1.2689 ± 0.0084	-20.1236 ± 34.3001	0.00005 ± 0.00002

Detector	Target	Run	m	q [keV]	a
	LNL103	935	1.1818 ± 0.016	-57.4878 ± 70.5405	0.00021 ± 0.00005
BGO	ATOMKI2	958	1.2084 ± 0.0164	-59.9875 ± 70.5267	0.00015 ± 0.00004
	ATOMKI2	958	1.2273 ± 0.0128	-46.3747 ± 54.0873	0.00008 ± 0.00003
	ATOMKI2	958	1.3563 ± 0.0099	-23.9476 ± 37.7462	0.00006 ± 0.00002
	ATOMKI2	958	1.292 ± 0.0098	-30.304 ± 39.2294	0.00006 ± 0.00002
	ATOMKI2	958	1.2709 ± 0.0089	-24.3576 ± 36.2815	0.00004 ± 0.00002
	ATOMKI2	958	1.1839 ± 0.0147	-53.0592 ± 64.4998	0.00022 ± 0.00004
BGO	ATOMKI2	976	1.2088 ± 0.0145	-57.4437 ± 62.4506	0.00015 ± 0.00004
	ATOMKI2	976	1.2247 ± 0.0111	-43.1823 ± 47.1063	0.00008 ± 0.00002
	ATOMKI2	976	1.3541 ± 0.0126	-27.1053 ± 48.3421	0.00007 ± 0.00003
	ATOMKI2	976	1.2889 ± 0.0105	-30.7211 ± 42.2726	0.00007 ± 0.00002
	ATOMKI2	976	1.2674 ± 0.0091	-24.6127 ± 37.0099	0.00005 ± 0.00002
	ATOMKI2	976	1.1813 ± 0.014	-54.786 ± 61.708	0.00022 ± 0.00004
BGO	ATOMKI2	998	1.2093 ± 0.015	-61.2306 ± 64.6763	0.00015 ± 0.00004
	ATOMKI2	998	1.2262 ± 0.014	-47.1258 ± 59.51	0.00009 ± 0.00003
	ATOMKI2	998	1.3559 ± 0.0142	-31.2035 ± 54.4045	0.00006 ± 0.00003
	ATOMKI2	998	1.2881 ± 0.0086	-29.4403 ± 34.5822	0.00006 ± 0.00002
	ATOMKI2	998	1.2676 ± 0.0083	-23.6974 ± 33.9895	0.00004 ± 0.00001
	ATOMKI2	998	1.1808 ± 0.0135	-53.4488 ± 59.5623	0.00022 ± 0.00004

A.2: Collection of all 45 decay cascades of the $E_x = 11\,988.5\,\text{keV}$ excited state of ^{24}Mg. All reported energy values are in keV while the branching ratio for a given γ_i emission is reported as (B_i). Grey shaded rows refers to the most probable cascades for each γ_0.

E_x^0	E_γ^0 (B_0)	E_x^1	E_γ^1 (B_1)	E_x^2	E_γ^2 (B_2)	E_x^3	E_γ^3 (B_3)	E_x^4	E_γ^4 (B_4)
11988.5	1257.4 (0.41)	10731.1	5495.2 (7.3)	5235.2	996.8 (2.34)	4238.4	2869.5 (21.75)	1368.7	1368.6 (100.0)
11988.5	1257.4 (0.41)	10731.1	5495.2 (7.3)	5235.2	996.8 (2.34)	4238.4	4238.0 (78.25)		
11988.5	1257.4 (0.41)	10731.1	5495.2 (7.3)	5235.2	3866.2 (88.79)	1368.7	1368.6 (100.0)		
11988.5	1257.4 (0.41)	10731.1	5495.2 (7.3)	5235.2	5235.0 (8.88)				
11988.5	1257.4 (0.41)	10731.1	6491.8 (19.71)	4238.4	2869.5 (21.75)	1368.7	1368.6 (100.0)		
11988.5	1257.4 (0.41)	10731.1	6491.8 (19.71)	4238.4	4238.0 (78.25)				
11988.5	1257.4 (0.41)	10731.1	9360.5 (72.99)	1368.7	1368.6 (100.0)				
11988.5	1929.3 (0.69)	10059.1	5820.0 (13.79)	4238.4	2869.5 (21.75)	1368.7	1368.6 (100.0)		
11988.5	1929.3 (0.69)	10059.1	5820.0 (13.79)	4238.4	4238.0 (78.25)				
11988.5	1929.3 (0.69)	10059.1	8688.6 (86.21)	1368.7	1368.6 (100.0)				
11988.5	2703.9 (0.92)	9284.4	5161.0 (21.26)	4122.9	2754.0 (100.0)	1368.7	1368.6 (100.0)		
11988.5	2703.9 (0.92)	9284.4	7914.3 (78.74)	1368.7	1368.6 (100.0)				
11988.5	2984.8 (0.6)	9003.5	1654.4 (7.45)	7348.6	5979.5 (37.89)	1368.7	1368.6 (100.0)		
11988.5	2984.8 (0.6)	9003.5	1654.4 (7.45)	7348.6	7347.2 (62.11)				
11988.5	2984.8 (0.6)	9003.5	2570.9 (8.7)	6432.2	2194.0 (17.36)	4238.4	2869.5 (21.75)	1368.7	1368.6 (100.0)
11988.5	2984.8 (0.6)	9003.5	2570.9 (8.7)	6432.2	2194.0 (17.36)	4238.4	4238.0 (78.25)		
11988.5	2984.8 (0.6)	9003.5	2570.9 (8.7)	6432.2	5063.2 (82.64)	1368.7	1368.6 (100.0)		
11988.5	2984.8 (0.6)	9003.5	4880.1 (21.74)	4122.9	2754.0 (100.0)	1368.7	1368.6 (100.0)		
11988.5	2984.8 (0.6)	9003.5	9001.7 (62.11)						
11988.5	3122.8 (5.07)	8864.5	3629.0 (1.94)	5235.2	996.8 (2.34)	4238.4	2869.5 (21.75)	1368.7	1368.6 (100.0)
11988.5	3122.8 (5.07)	8864.5	3629.0 (1.94)	5235.2	996.8 (2.34)	4238.4	4238.0 (78.25)		
11988.5	3122.8 (5.07)	8864.5	3629.0 (1.94)	5235.2	3866.2 (88.79)	1368.7	1368.6 (100.0)		

E_x^0	E_γ^0 (B_0)	E_x^1	E_γ^1 (B_1)	E_x^2	E_γ^2 (B_2)	E_x^3	E_γ^3 (B_3)	E_x^4	E_γ^4 (B_4)
11988.5	3122.8 (5.07)	8864.5	3629.0 (1.94)	5235.2	5235.0 (8.88)				
11988.5	3122.8 (5.07)	8864.5	4625.7 (7.94)	4238.4	2869.5 (21.75)	1368.7	1368.6 (100.0)		
11988.5	3122.8 (5.07)	8864.5	4625.7 (7.94)	4238.4	4238.0 (78.25)				
11988.5	3122.8 (5.07)	8864.5	7494.6 (89.21)	1368.7	1368.6 (100.0)				
11988.5	3122.8 (5.07)	8864.5	8862.7 (0.92)						
11988.5	3549.8 (2.9)	8438.4	7068.6 (20.0)	1368.7	1368.6 (100.0)				
11988.5	3549.8 (2.9)	8438.4	8436.8 (80.0)						
11988.5	4240.4 (5.07)	7747.7	3509.1 (8.49)	4238.4	2869.5 (21.75)	1368.7	1368.6 (100.0)		
11988.5	4240.4 (5.07)	7747.7	3509.1 (8.49)	4238.4	4238.0 (78.25)				
11988.5	4240.4 (5.07)	7747.7	6378.1 (65.83)	1368.7	1368.6 (100.0)				
11988.5	4240.4 (5.07)	7747.7	7746.4 (25.67)						
11988.5	4432.8 (1.52)	7555.3	3316.7 (23.0)	4238.4	2869.5 (21.75)	1368.7	1368.6 (100.0)		
11988.5	4432.8 (1.52)	7555.3	3316.7 (23.0)	4238.4	4238.0 (78.25)				
11988.5	4432.8 (1.52)	7555.3	6185.8 (30.05)	1368.7	1368.6 (100.0)				
11988.5	4432.8 (1.52)	7555.3	7554.0 (46.95)						
11988.5	6752.3 (7.83)	5235.2	996.8 (2.34)	4238.4	2869.5 (21.75)	1368.7	1368.6 (100.0)		
11988.5	6752.3 (7.83)	5235.2	996.8 (2.34)	4238.4	4238.0 (78.25)				
11988.5	6752.3 (7.83)	5235.2	3866.2 (88.79)	1368.7	1368.6 (100.0)				
11988.5	6752.3 (7.83)	5235.2	5235.0 (8.88)						
11988.5	7748.8 (46.08)	4238.4	2869.5 (21.75)	1368.7	1368.6 (100.0)				
11988.5	7748.8 (46.08)	4238.4	4238.0 (78.25)						
11988.5	10617.3 (28.11)	1368.7	1368.6 (100.0)						
11988.5	11985.3 (0.78)								

A.3: In order to use the Covell method of Eq. (5.2), I used two reasonable ranges: an outer range to select the overall energy region and an inner range which represent the peak region. Their exact values are reported in Tab. .3. In this table I report the energetic ranges used in the peaks analysis.

Line	Outer range [keV]		Inner range [keV]	
	HPGe	BGO	HPGe	BGO
1368.6 keV	–	1050 – 1650	–	1150 – 1550
4240.0 keV	–	3800 – 4800	–	4000 – 4600
7748.8 keV	7720 – 7780	7300 – 8300	7735 – 7765	7400 – 8200
10617.3 keV	10580 – 10650	10250 – 11300	10600 – 10640	10350 – 11200
6129.9 keV	–	5750 – 6600	–	5850 – 6500
11660.1 keV	–	10000 – 13000	–	10500 – 12500

References

[1] Shuichiro Inutsuka (Oct. 2012). 'Present-day star formation: From molecular cloud cores to protostars and protoplanetary disks'. In: *Progress of Theoretical and Experimental Physics* 2012.1, 01A307. ISSN: 2050-3911. DOI: 10.1093/ptep/pts024.

[2] André Maeder (2009). 'Pre-stellar Phase'. In: pp. 475–495. DOI: 10.1007/978-3-540-76949-1_18.

[3] James Hopwood Jeans and James Jeans (1928). *Astronomy and cosmogony*. Canbridge, The University Press.

[4] E. E. Salpeter (July 1957). 'Nuclear Reactions in Stars. Buildup from Helium'. In: *Phys. Rev.* 107 (2), pp. 516–525. DOI: 10.1103/PhysRev.107.516.

[5] Falk Herwig (2005). 'Evolution of Asymptotic Giant Branch Stars'. In: *Annual Review of Astronomy and Astrophysics* 43.1, pp. 435–479. DOI: 10.1146/annurev.astro.43.072103.150600.

[6] C. Iliadis (2007). *Thermonuclear Reactions*. John Wiley & Sons, Ltd. DOI: https://doi.org/10.1002/9783527618750.

[7] A. Slemer et al. (Nov. 2016). '22Ne and 23Na ejecta from intermediate-mass stars: the impact of the new LUNA rate for 22Ne(p,)23Na'. In: *Monthly Notices of the Royal Astronomical Society* 465.4, pp. 4817–4837. ISSN: 1365-2966. DOI: 10.1093/mnras/stw3029.

[8] E. Carretta et al. (July 2009). 'Na-O anticorrelation and HB: VIII. Proton-capture elements and metallicities in 17 globular clusters from UVES spectra'. In: *Astronomy & Astrophysics* 505.1, pp. 139–155. ISSN: 1432-0746. DOI: 10.1051/0004-6361/200912097.

[9] E. Carretta et al. (Apr. 2006). 'Na-O anticorrelation and HB. The Na-O anticorrelation in NGC 2808'. In: *Astronomy & Astrophysics* 450.2, pp. 523533. ISSN: 1432-0746. DOI: 10.1051/0004-6361:20054369.

[10] Inese I. Ivans et al. (Sept. 2001). 'New Analyses of Star-to-Star Abundance Variations among Bright Giants in the Mildly Metal-poor Globular Cluster M5'. In: *The Astronomical Journal* 122.3, p. 1438. DOI: 10.1086/322108.

[11] E. Carretta (2007). 'The chemical composition of the peculiar bulge globular cluster NGC 6388'. In: *Astronomy & Astrophysics* 464.3, pp. 967–981. DOI: 10.1051/0004-6361:20066065.

[12] R. G. Gratton (2007). 'The Na-O anticorrelation in NGC 6441 from Giraffe spectra'. In: *Astronomy & Astrophysics* 464.3, pp. 953–965. DOI: 10.1051/0004-6361:20066061.

[13] Boeltzig Axel (2016). 'Direct measurements of the ^{23}Na$(p,\gamma)^{24}$Mg cross Section at stellar Energies'. PhD thesis.

[14] Richard B Firestone (2007). 'Adopted Levels Gammas for 24Mg'. In: *Nucl. Data Sheets* 108, p. 2319.

[15] S. A. Wender et al. (Apr. 1978). 'Confirmation of 8^+ assignment to the 11.86 MeV level in ^{24}Mg'. In: *Phys. Rev. C* 17 (4), pp. 1365–1367. DOI: 10.1103/PhysRevC.17.1365.

[16] S. E. Hale et al. (Oct. 2004). 'Investigation of the ^{23}Na$(p,\gamma)^{24}$Mg and ^{23}Na$(p,\alpha)^{20}$Ne reactions via (^{3}He$,d$) spectroscopy'. In: *Phys. Rev. C* 70 (4), p. 045802. DOI: 10.1103/PhysRevC.70.045802.

[17] J. Goerres, M. Wiescher and C. Rolfs (Aug. 1989). 'Hydrogen Burning of ^{23}Na in the NeNa Cycle'. In: *Astrophysical Journal* 343, p. 365. DOI: 10.1086/167710.

[18] C. Rowland et al. (Nov. 2004). 'Does an NeNa Cycle Exist in Explosive Hydrogen Burning?' In: *Astrophysical Journal, Letters* 615.1, pp. L37–L40. DOI: 10.1086/425964.

[19] C. Iliadis and A.E. Champagne (2005). 'Nuclear Astrophysics: Direct measurements with stable beams'. In: *Nuclear Physics A* 758. Nuclei in the Cosmos VIII, pp. 73–79. ISSN: 0375-9474. DOI: https://doi.org/10.1016/j.nuclphysa.2005.05.019.

[20] J. M. Cesaratto et al. (2013). 'Measurement of the $E_r^{\mathrm{cm}} = 138$ keV resonance in the ^{23}Na$(p,\gamma)^{24}$Mg reaction and the abundance of sodium in AGB stars'. In: *Phys. Rev. C* 88 (6), p. 065806. DOI: 10.1103/PhysRevC.88.065806.

[21] C. Marshall et al. (Sept. 2021). 'New energy for the 133keV resonance in the ^{23}Na$(p,\gamma)^{24}$Mg reaction and its impact on nucleosynthesis in globular clusters'. In: *Phys. Rev. C* 104 (3), p. L032801. DOI: 10.1103/PhysRevC.104.L032801.

[22] C. Angulo et al. (1999). 'A compilation of charged-particle induced thermonuclear reaction rates'. In: *Nuclear Physics A* 656.1, pp. 3–183. ISSN: 0375-9474. DOI: https://doi.org/10.1016/S0375-9474(99)00030-5.

[23] C. Iliadis et al. (Oct. 2010). 'Charged-particle thermonuclear reaction rates. Tables and graphs of reaction rates and probability density functions'. In: *Nuclear Physics A* 841.1-4, pp. 31–250. ISSN: 0375-9474. DOI: 10.1016/j.nuclphysa.2010.04.009.

[24] U. Greife et al. (1994). 'Laboratory for Underground Nuclear Astrophysics (LUNA)'. In: *Nuclear Instruments and Methods in Physics Research Section A: Accelerators, Spectrometers, Detectors and Associated Equipment* 350.1, pp. 327–337. ISSN: 0168-9002. DOI: https://doi.org/10.1016/0168-9002(94)91182-7.

[25] A. Formicola et al. (2003). 'The LUNA II 400kV accelerator'. In: *Nuclear Instruments and Methods in Physics Research Section A: Accelerators, Spectrometers, Detectors and Associated Equipment* 507.3, pp. 609–616. ISSN: 0168-9002. DOI: https://doi.org/10.1016/S0168-9002(03)01435-9.

[26] A. Boeltzig et al. (2019). 'Direct measurements of low-energy resonance strengths of the ^{23}Na$(p,\gamma)^{24}$Mg reaction for astrophysics'. In: *Physics Letters B* 795, pp. 122–128. ISSN: 0370-2693. DOI: https://doi.org/10.1016/j.physletb.2019.05.044.

[27] M. Haffke et al. (July 2011). 'Background measurements in the Gran Sasso Underground Laboratory'. In: *Nuclear Instruments and Methods in Physics Research Section A: Accelerators, Spectrometers, Detectors and Associated Equipment* 643.1, pp. 36–41. ISSN: 0168-9002. DOI: 10.1016/j.nima.2011.04.027.

[28] C. G. Bruno et al. (Aug. 2015). 'Resonance strengths in the ^{17,18}O$(p,\alpha)^{14,15}$N reactions and background suppression underground. Commissioning of a new setup for charged-particle detection at LUNA'. In: *European Physical Journal A* 51, 94, p. 94. DOI: 10.1140/epja/i2015-15094-y.

[29] C. G. Bruno et al. (Sept. 2016). 'Improved Direct Measurement of the 64.5 keV Resonance Strength in the ^{17}O$(p,\alpha)^{14}$N Reaction at LUNA'. In: *Phys. Rev. Lett.* 117.14, 142502, p. 142502. DOI: 10.1103/PhysRevLett.117.142502. arXiv: 1610.00483.

[30] Antonio Caciolli and on behalf of the LUNA collaboration (2020). 'Nuclear Astrophysics in underground laboratories: the LUNA experiment'. In: *Journal of Physics: Conference Series* 1610.1, p. 012002. DOI: 10.1088/1742-6596/1610/1/012002.

[31] Axel Boeltzig and for the LUNA Collaboration (2016). 'Cross Section Measurements for the 23Na(p,)24Mg Reaction at LUNA'. In: *Journal of Physics: Conference Series* 689.1, p. 012014. DOI: 10.1088/1742-6596/689/1/012014.

[32] A Boeltzig et al. (Jan. 2018). 'Improved background suppression for radiative capture reactions at LUNA with HPGe and BGO detectors'. In: *Journal of Physics G: Nuclear and Particle Physics* 45.2, p. 025203. DOI: 10.1088/1361-6471/aaa163.

[33] C Casella et al. (2002). 'A new setup for the underground study of capture reactions'. In: *Nuclear Instruments and Methods in Physics Research Section A: Accelerators, Spectrometers, Detectors and Associated Equipment* 489.1, pp. 160–169. ISSN: 0168-9002. DOI: https://doi.org/10.1016/S0168-9002(02)00577-6.

[34] S. Seuthe et al. (1987). 'Production and properties of implanted targets'. In: *Nuclear Instruments and Methods in Physics Research Section A: Accelerators, Spectrometers, Detectors and Associated Equipment* 260.1, pp. 33–42. ISSN: 0168-9002. DOI: https://doi.org/10.1016/0168-9002(87)90385-8.

[35] J. Keinonen et al. (1989). 'Short lifetimes in ^{24}Mg for test of rotational collectivity in shell-model wave functions'. In: *Nuclear Physics A* 493.1, pp. 124–144. ISSN: 0375-9474. DOI: https://doi.org/10.1016/0375-9474(89)90536-8.

[36] T.A.D. Brown et al. (2009). 'Properties of ^{23}Na implanted targets'. In: *Nuclear Instruments and Methods in Physics Research Section B: Beam Interactions with Materials and Atoms* 267.19, pp. 3302–3308. ISSN: 0168-583X. DOI: https://doi.org/10.1016/j.nimb.2009.06.122.

[37] S. Wagner and M. Heitzmann (1960). 'Resonanzenergien für den Protoneneinfang'. In: *Zeitschrift für Naturforschung A* 15.1, pp. 74–78. DOI: doi:10.1515/zna-1960-0111.

[38] P.W.M. Glaudemans and P.M. Endt (1963). 'The ^{23}Na$(p,\gamma)^{24}$Mg reaction'. In: *Nuclear Physics* 42, pp. 367–382. ISSN: 0029-5582. DOI: https://doi.org/10.1016/0029-5582(63)90742-9.

[39] SG Boydell and DG Sargood (1975). 'Accurate Branching Ratio Measurements in ^{23}Na$(p,\gamma)^{24}$Mg'. In: *Australian Journal of Physics* 28.4, pp. 369–382.

[40] M.A. Meyer, J.P.L. Reinecke and D. Reitmann (1972). 'A study of the ^{23}Na$(p,\gamma)^{24}$Mg reaction and the excited states of ^{24}Mg'. In: *Nuclear Physics A* 185.2, pp. 625–643. ISSN: 0375-9474. DOI: https://doi.org/10.1016/0375-9474(72)90037-1.

[41] F. W. Prosser et al. (Jan. 1962). 'Gamma Radiation from Proton Capture in ^{23}Na'. In: *Phys. Rev.* 125 (2), pp. 594–599. DOI: 10.1103/PhysRev.125.594.

[42] B.M. Paine and D.G. Sargood (1979). '(p,γ) Resonance strengths in the s-d shell'. In: *Nuclear Physics A* 331.2, pp. 389–400. ISSN: 0375-9474. DOI: https://doi.org/10.1016/0375-9474(79)90349-X.

[43] Donald M. Mattox (2000). 'Physical vapor deposition processes'. In: *Metal Finishing* 98.1, pp. 410–423. ISSN: 0026-0576. DOI: https://doi.org/10.1016/S0026-0576(00)80350-5.

[44] *Principles of magnetron sputtering* (n.d.). Accessed: 2024-01-30. URL: https://nabis.fisi.polimi.it/equipments/aja-atc-orion-8-sputtering-system.

[45] Stodel, Christelle (2020). 'Methods of targets characterization'. In: *EPJ Web Conf.* 229. DOI: 10.1051/epjconf/202022902001.

[46] G. F. Ciani et al. (Mar. 2020). 'A new approach to monitor ^{13}C-targets degradation in situ for $^{13}(\alpha, n)^{16}$O cross-section measurements at LUNA'. In: *European Physical Journal A* 56.3, 75, p. 75. DOI: 10.1140/epja/s10050-020-00077-0.

[47] A. Boeltzig et al. (Oct. 2022). 'Investigation of direct capture in the ^{23}Na$(p, \gamma)^{24}$Mg reaction'. In: *Phys. Rev. C* 106 (4), p. 045801. DOI: 10.1103/PhysRevC.106.045801.

[48] Gordon Gilmore (Apr. 2008). *Practical Gamma-Ray Spectrometry*. DOI: 10.1002/9780470861981.

[49] Vigolo Anna (2022). 'Study of the ^{14}N$(p, \gamma)^{15}$O reaction in a wide energy range in underground with LUNA'. PhD thesis.

[50] Ziegler F. James (2013). *Stopping and Range of Ions in Matter*. URL: http://www.srim.org/.

[51] F. Ajzenberg-Selove (1990). 'Energy levels of light nuclei A = 11-12'. In: *Nuclear Physics A* 506.1, pp. 1–158. ISSN: 0375-9474. DOI: https://doi.org/10.1016/0375-9474(90)90271-M.

[52] D.R. Tilley, H.R. Weller and C.M. Cheves (1993). 'Energy levels of light nuclei A = 16-17'. In: *Nuclear Physics A* 564.1, pp. 1–183. ISSN: 0375-9474. DOI: https://doi.org/10.1016/0375-9474(93)90073-7.